Modelling and reconstruction of events in SNO+ related to future searches for lepton and baryon number violation

Ian T. Coulter

Balliol College, Oxford

Thesis submitted in partial fulfilment of the requirements for the degree of Doctor of Philosophy at the University of Oxford

Trinity Term, 2013

Modelling and reconstruction of events in SNO+ related to future searches for lepton and baryon number violation

Ian T. Coulter
Balliol College, Oxford

Thesis submitted in partial fulfilment of the requirements for the degree of Doctor of Philosophy at the University of Oxford

Trinity Term, 2013

Abstract

SNO+ is a liquid scintillator experiment whose physics goals include measurements of solar neutrinos, reactor anti-neutrinos, geo neutrinos and double beta decay. During an initial water phase, it will also search for invisible modes of nucleon decay.

This thesis investigates methods of improving the detector's sensitivity to the baryon and lepton violating processes of neutrinoless double beta decay and invisible nucleon decay. It does this through an improved scintillator model, allowing the sensitivity of the detector with different loading techniques to be evaluated, through a new background rejection technique, capable of increasing the active volume of the detector, and with the development of improved position fitters, achieving resolutions of approximately 10 cm in scintillator and 25 cm in water.

The sensitivity of SNO+ to invisible modes of nucleon decay is explored, predicting, after one month of data, a limit of $\tau > 1.38 \times 10^{30}$ years on the decay of neutrons and of $\tau > 1.57 \times 10^{30}$ years on the decay of protons.

Acknowledgements

Firstly, I would like to thank my supervisor Steve Biller from whom I've learnt a lot in the last four years. Without his enthusiasm and his ability to find me such a variety of interesting tasks to do, my work on this PhD would have been a lot less interesting. His advice and remarkably accurate 'back of the envelope' calculations have proved invaluable, particularly during the thesis-writing stage.

I also would like to thank Armin Reichold for attempting to teach me the correct way to work in a lab as well as for his ability to provide an expert opinion on any topic which has provided some interesting conversations over group meetings and lunchtimes. I also need to thank Ken Clark who, during his time at Oxford, provided me with a practical example of how to work in a lab (as well as just how much can be achieved using blu-tac and paperclips) as well as managing to recognise and correct my Arrested Development and Simpsons quotes. Many thanks must also go to Phil Jones who, as a senior grad student, took the time to give me advice on coding and introduced me to the various problems of RAT and Root and, on whose work and advice, the reconstruction chapters of this thesis are built upon.

The other Oxford students Krish, Chris and Rehan have each helped me out during their time here and have put up with me during the final months of writing this thesis. In addition, Nick Jelley and Mark Chen have also provided interesting discussions and advice during my time in Oxford.

Outside Oxford, I would like to thank those at SNOLAB, particularly Christine, Peter and Noel, for showing me just how much work goes into building and maintaining a particle physics detector. Similarly, thanks to those on the ELLIE installation crew (Simon, James, Gwen, Jose, Sofia and Luiz) who were willing to let me tag along and who made Sudbury an interesting place to stay during those

couple of months. Particular thanks must go to James Sinclair for his willingness to chaffeur me through Canada and North America and to Matt Mottram for managing to find a pub serving real ale in Sudbury. Thanks also to many others on the SNO+ experiment, all of whom have been friendly and full of advice and who have made the last couple of years such an enjoyable experience.

Thanks must also go to the support staff in Oxford, particularly technicians such as Bryan Finnegan, Rik Elliot and John Saunders, who have dealt well with the ever-changing demands of the SMELLIE system, the IT staff, who have have always managed to fix the various ways I have managed to break my computer, and to the physics secretaries, Kim Proudfoot and Sue Geddes, who have always been willing to help out with last minute trips to Canada.

I'd also like to thank the Osney raiders (Rich, Simon, Alex and Jamie) as well as Ed, Tim, Andy, James, Ellie and Vitek for making Oxford an entertaining place to live for the last four years. Without the trips to the pub, football, darts and other distractions, I wouldn't have enjoyed my time in Oxford nearly as much.

Finally, and most importantly, I'd like to thank my family. Without the love and support of my parents as well as my brother and sister, Philip and Hazel, I wouldn't be where I am today.

Contents

List of Figures

List of Tables

Chapter 1

The physics of SNO+

SNO+ is a large liquid scintillator detector based in SNOLAB, Canada. Among its physics goals are the measurement of low energy solar neutrinos, measurements of anti-neutrinos from nearby reactors, geo neutrinos from the Earth and of neutrinoless double beta decay. During an initial water phase, used to calibrate the detector, SNO+ will also be able to search for invisible modes of nucleon decay. Of these, neutrinoless double beta decay and nucleon decay are both non-Standard Model processes which violate lepton and baryon number, respectively. The detector itself is described in more detail in Chapter 2.

Lepton number is equal to the number of leptons minus the number of anti-leptons and is a conserved quantity in all Standard Model interactions. Similarly, baryon number is equal to the number of baryons minus the number of anti-baryons and is also conserved throughout the Standard Model. Although these conservation laws have not been observed to be violated, many Grand Unified Theories predict that they will via processes such as neutrinoless double beta decay or nucleon decay. Further motivation to investigate this lies in the Sakharov conditions necessary for a matter dominated universe, one of which is the violation of baryon number, alongside CP violation and for the universe not to be in thermal equilibrium when the asymmetry is generated[1]. Some cosmological models use

leptogenesis, requiring violation of lepton number, as a mechanism to create the matter-antimatter asymmetry which is then converted to an excess of baryons[2].

This thesis describes scintillator modelling and reconstruction algorithms developed with an aim to improve the sensitivity of the SNO+ experiment to neutrinoless double beta decay and nucleon decay. This includes an improved scintillator model, discussed in Chapter 3 and 4, which allows evaluation of different loading techniques in attempt to increase the amount of double beta decay isotope that can be added into the scintillator. Also investigated are position reconstruction algorithms for scintillator, in Chapter 5, and water, in Chapter 7. A good position fit is required to prevent the reconstruction of external backgrounds into the fiducial volume of the detector and to provide the necessary energy resolution to distinguish between the neutrinoless double beta decay signal from the two neutrino background. In the water phase, the direction fit will also be used to identify and cut solar neutrino backgrounds during the nucleon decay analysis. In Chapter 6, a new background rejection technique is discussed which uses a likelihood based technique to identify external backgrounds originating outside the scintillator volume. These will provide a limit on the fiducial volume of the detector. This method aims to tag the background events and so to increase the active volume of the detector that will be used in a double beta decay analysis. Finally in Chapter 8, the sensitivity of the SNO+ detector to invisible modes of nucleon decay is explored and a prediction is made on the limit that can be set after a month of running in the water phase of the experiment.

This chapter describes the motivation behind looking for the processes of neutrinoless double beta decay and of nucleon decay and details the current status of measurements.

1.1 The neutrino

Neutrinos are a fundamental Standard Model particle with neutral charge and spin one half. They exist as neutral counterparts to the charged leptons, interacting via the weak interaction, with three flavours: electron, muon and tau. The neutrino is the lightest known particle in the Standard Model with a very low, but non-zero, mass.

Neutrinos were first predicted by W.Pauli, in his letter beginning 'Dear radioactive ladies and gentleman...', in 1930 to explain the missing portion of the measured energy of the electrons produced in beta decays. Since the emission of beta-rays from a particular transition should have a fixed energy, a single energy peak would have been expected. Instead, a continuous energy spectrum was observed. This appeared to violate the conservation of energy, unless another particle was carrying away some of this energy unobserved. This was the neutrino, as hypothesised by Pauli, which would have to be a low mass electrically neutral particle whose energy, added to that of the beta, would give the fixed energy required for energy conservation. This was then developed further into a working theory of beta decay by E.Fermi in 1934[3].

The neutrino was first detected experimentally, in 1956, when F.Reines and C.Cowan detected electron anti-neutrinos from a nuclear reactor at Savannah River in South Carolina[4]. The experiment used the interaction of the anti-neutrinos with protons in a tank of water. This produces a positron, which annihilates quickly with an electron to produce two gamma rays, and a neutron which is captured by cadmium nuclei, dissolved in the water, producing another set of gammas after a delay of 5 μs. This allowed the use of the delayed coincidence to distinguish these events from backgrounds.

This was followed by the detection of ν_μ at Brookhaven in 1962[5] and ν_τ by the DONuT experiment in 2000[6]. The total number of neutrinos flavours, coupling

to the weak force and with mass below half that of the Z boson, was measured experimentally from the width of the Z^0 mass at LEP and found to be consistent with three[7].

Helicity is defined as the projection of a particle's spin along its momentum. The neutrino helicity was measured in 1957, by Goldhaber et al[8], using the inverse beta decays of samarium atoms via electron capture to measure the helicity of the neutrino produced. This found that neutrinos have negative helicity. The weak interaction only couples to left handed neutrinos and right handed anti-neutrinos so only left handed neutrinos have been observed in nature. In the limit of a massless neutrino, left-handed neutrinos are equivalent to negative helicity neutrinos. If the neutrino has mass, this will allow the neutrino to be in a reference frame moving faster than its momentum and so in which its helicity is flipped. This helicity flip will be suppressed by the high energy required, due to the low mass of the neutrino, and, for a massless neutrino, this is forbidden entirely.

1.2 Neutrino oscillations

In hadronic physics, it has long been known that particles can oscillate between states, e.g. kaon oscillations where the kaons are created as the K^0 or $\overline{K}^0$, states of definite mass, but propagate as states of definite lifetime, K_{Short} and K_{Long} which exist as a superposition of the mass eigenstates. Similarly, oscillations have also been observed in the neutrino sector as the weak flavour eigenstates are not the same as the mass eigenstates. A beam of single flavour neutrinos will oscillate over time and distance to contain neutrinos of the other flavours as well, with the composition depending on the distance from the source, the energy of the neutrinos and the difference in the mass squared of the states:

$$P_{\nu_\alpha \to \nu_\beta}(L, E) = \sum_{i,j} U_{\alpha i} U^*_{\alpha j} U^*_{\beta i} U_{\beta j} \exp \frac{-i \Delta m^2_{ij} L}{2E} \tag{1.1}$$

where $P_{\nu_\alpha \to \nu_\beta}$ is the probability of a neutrino created of flavour α and energy E having a flavour β after travelling a distance L. Δm^2_{ij} is the difference in the mass squared of the mass states i and j while U is the PMNS (Pontecorvo Maki Nakagawa Sakata) matrix which gives the mixing between the mass states. This matrix can be parameterised in terms of three mixing angles θ_{12}, θ_{23} and θ_{13} and a phase δ[9].

Oscillations were found useful in explaining observations of atmospheric neutrinos. High energy cosmic rays interact in the upper atmosphere, producing mainly pions which decay to produce both muon and electron neutrinos:

$\pi^\pm \to \mu^\pm + \nu_\mu(\overline{\nu}_\mu)$

$\mu^\pm \to \mathrm{e}^- + \nu_e(\overline{\nu}_e) + \overline{\nu}_\mu(\nu_\mu)$

Measurements were made of the atmospheric neutrino flux by the Super-Kamiokande experiment, which is a large underground water Cherenkov detector based in Japan containing 50,000 tonnes of water surrounded by 13,000 photo-multiplier tubes. It was found that, while the ν_e flux was consistent with what was expected, there was a deficit in the amount of ν_μ detected. By comparing the downward flux, from neutrinos created typically 10 km above the Earth's surface, and the upward flux, after neutrinos have travelled through the Earth itself, the L/E behaviour of this disappearance was able to be investigated and was found to match that expected from neutrino oscillation[10]. While not conclusive proof of neutrino oscillations themselves, the energy dependence of the disappearance suggested that neutrinos had mass. This was investigated further using accelerator neutrinos at suitable baselines, such as the K2K[11] and MINOS[12] experiments, which observed ν_μ disappearance but no ν_e appearance, consistent with ν_μ to ν_τ oscillations.

Oscillations such as these also provided an explanation for the 'solar neutrino problem', where the measurements of the neutrino flux from sun were found to be less than expected from the Standard Solar Model, initially suggested by R.Davis at Homestake[13], South Dakota, but confirmed by other experiments such as Kamiokande[14] and SAGE[15]. It was suggested that this discrepancy could be explained by the electron neutrinos produced in the sun oscillating to other flavours that are undetected. This was resolved, in 2002, by the SNO experiment which, as with other detectors, could measure the charged current and elastic scattering interactions:

$\nu_e + \mathrm{d} \rightarrow \mathrm{e}^- + \mathrm{p} + \mathrm{p}$

$\nu + \mathrm{e}^- \rightarrow \nu + \mathrm{e}^-$

which are sensitive mainly to ν_e, but also neutral current interactions:

$\nu + \mathrm{d} \rightarrow \nu + \mathrm{p} + \mathrm{n}$

which are independent of the neutrino flavour and so gave a measure of the total neutrino flux. SNO found that the total neutrino flux was consistent with the Standard Solar Model while the ν_e flux was only about 30 % of this[16][17], providing proof of neutrino flavour change. By combining the results of SNO and KamLAND, oscillations could be confirmed and the ordering of m_1 and m_2 determined[18].

As recently as 2012, the third mixing angle θ_{13} has been measured to be $\sin(2\theta_{13}) = 0.092 \pm 0.016(stat) \pm 0.005(syst)$ at a significance of 5.2 sigma at Daya Bay[19], in China, and as $\sin(2\theta_{13}) = 0.113 \pm 0.013(stat) \pm 0.019(syst)$ at a significance of 4.9 sigma at RENO[20], in South Korea, finding a non-zero value for θ_{13}, using neutrinos from nearby reactors, after hints from T2K[21] and Double Chooz[22].

1.3 Massive neutrinos

As suggested by neutrino oscillations, it appears that neutrinos have a small but non-zero mass. However, in the Standard Model of particle physics, neutrino masses are set to zero. This means that neutrino masses require non-Standard Model physics to explain them.

Neutrino oscillations don't provide a direct measure of the masses but instead is only sensitive to the difference between the masses squared. The current best values for the neutrino mass differences, from a global fit of available data, taken from the PDG[23] are:

$\Delta m^2_{23} = 2.35 \times 10^{-3} eV^2$

$\Delta m^2_{12} = 7.58 \times 10^{-5} eV^2$

Due to the uncertainties on the mass differences, it isn't possible to determine the ordering of the neutrino masses. It can be seen that m_1 and m_2 are similar in mass while m_3 is further away. However it is unclear whether m_3 is of higher mass than 1 and 2, the normal mass hierarchy, or lower mass, the inverted hierarchy, as shown on Figure 1.1. Figure 1.2 shows the allowed values of the neutrino masses taking into account the orderings of the normal and inverted hierarchies and the constraints laid by the oscillation measurements as well as cosmological and neutrinoless double beta decay limits.

The most direct way to search for the neutrino mass is to use measurements of the endpoint of beta decays. Near the endpoint, the shape of the spectrum is very dependent on the neutrino mass. These experiments require a good energy resolution and a low endpoint energy. Tritium is a popular isotope for this, with a low endpoint of 18.6 keV and a simple structure, reducing the uncertainty due to nuclear effects. The current best limit for the mass of ν_e comes from the Mainz[26] and Troitsk[27] experiments and is less than 2 eV. Currently under construction is the KATRIN experiment, based in Karlsruhe, Germany, which uses a large

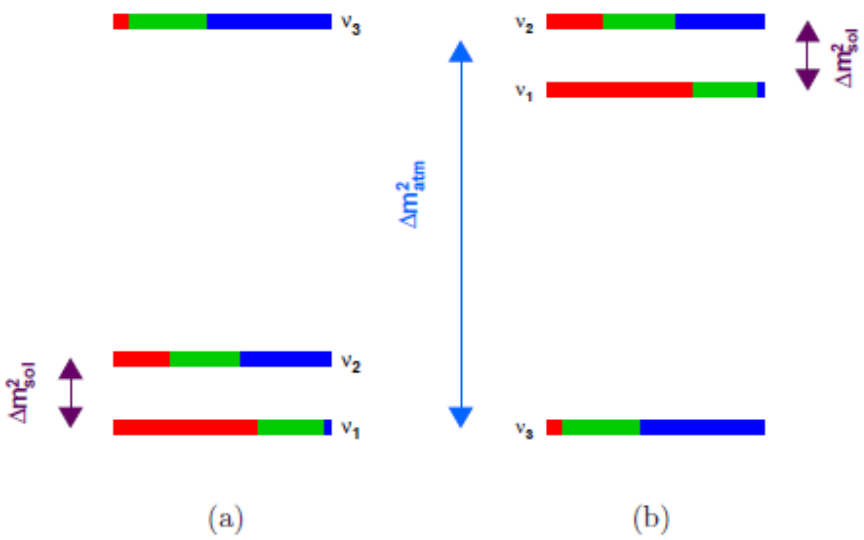

Figure 1.1: Possible neutrino mass orderings for a) the normal hierarchy and b) the inverted hierarchy. The electron, muon and tau fraction of each mass state is shown in the colours red, blue and green. This figure is taken from[24].

spectrometer with expected sensitivity to neutrino masses down to 0.2 eV[28].

Direct measurements of the muon and tau neutrino masses have been made using the kinematics of pion and tau decays respectively. However the limits achieved are much higher, 190 keV for the ν_μ [29] and 18.2 MeV for the ν_τ [30].

Planck and WMAP were able to set a cosmological limit of $\sum m_\nu$ <0.66 eV on the mass of the active neutrinos by investigating the structure of the CMB and gravitational lensing[31].

1.3.1 Neutrinoless double beta decay

One of the questions still unanswered about neutrinos is whether the neutrino and anti-neutrino are distinct particles. In 1937, E.Majorana suggested that the neutrino may be the same as its anti-particle[32], a Majorana particle, as opposed to being separate Dirac particles, as is the case for most Standard Model particles. This is possible because, unlike other fundamental Standard Model fermions, the neutrino has a neutral charge. Applying the Dirac theory to neutrinos produces

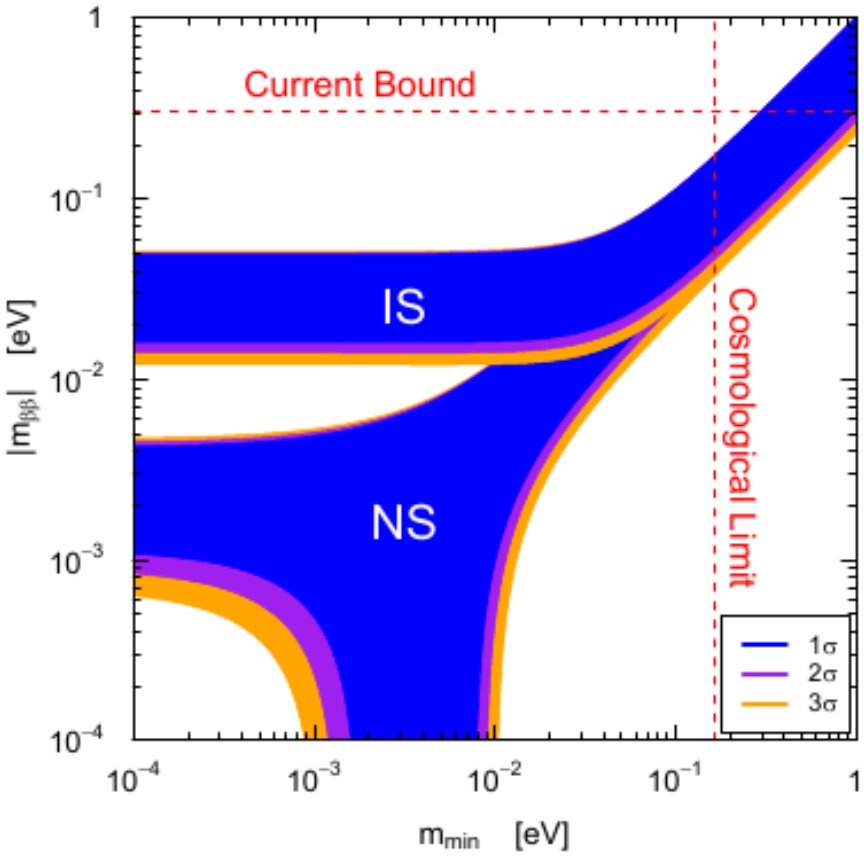

Figure 1.2: Effective Majorana mass as a function of the lightest neutrino mass for the normal and inverted mass hierarchys. Effective Majorana mass is defined as a sum of the three neutrino masses, $m_{\beta\beta} = |\sum_{i=1}^{3} m_i U_{ei}^2|$. This figure is taken from[25].

four states, particle and anti-particle, each with a left handed and right handed state. Majorana's theory results in two states that are either left handed or right handed. So in this case, what is observed as the anti-neutrino would be the right handed state of the neutrino.

Majorana neutrinos are preferred in many beyond Standard Models theories. They allow some processes such as neutrinoless double beta decay (discussed further below) which don't conserve lepton number and so provide a mechanism for leptogenesis. They can also provide an explanation for why neutrino masses are significantly lower than those of the quarks and even the charged leptons. In certain theories, the 'seesaw mechanism' suppresses the neutrino mass with respect

to that of a heavy Majorana neutrino[2].

If the neutrino was massless, there would be no way to distinguish these theories. However, a massive Majorana neutrino permits certain nuclei to undergo the process of 'neutrinoless double beta decay'.

Double beta decay is a process, first proposed by Goeppert-Mayer in 1935[33], by which a nucleus can change its charge by two, as two neutrons simultaneously undergo beta decay to produce two sets of a proton, an electron and an antineutrino, as shown on Figure 1.3 a). This can occur in nature if the single beta decay is forbidden, either by reasons of energy, as the daughter nucleus would require higher energy than the parent state, or strongly suppressed by angular momentum considerations. In this case, it can be energetically favourable for the nucleus to change its atomic number by two units instead, undergoing double beta decay. Due to the binding energy of the nucleons, this is most common in 'even-even' nuclei such as those shown in Table 1.1.

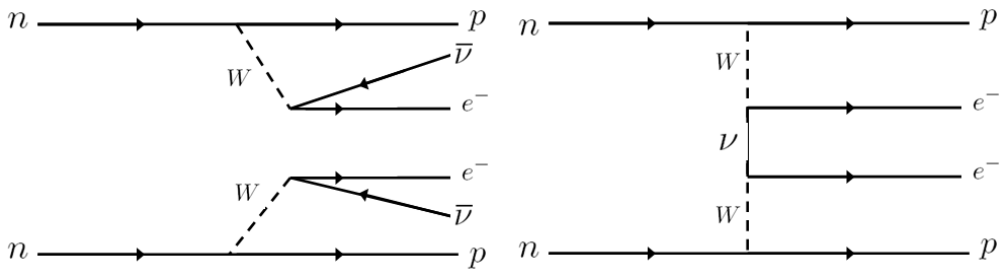

(a) Two neutrino double beta decay (b) Neutrinoless double beta decay

Figure 1.3: Feynmann diagrams for a) two neutrino and b) neutrinoless double beta decay.

Shortly after Majorana's proposal, W.Furry in 1939 suggested that, for Majorana neutrinos, these nuclei would also be able to undergo neutrinoless double beta decay[34], $0\nu\beta\beta$, as shown on the Feynmann diagram on Figure 1.3 b). In this case, the first neutron undergoes beta decay, emitting a right-handed anti-neutrino with a positive helicity (alongside a negative helicity electron). If the neutrino is massive, the anti-neutrino can flip its helicity and so have a negative

Transition	Q-value (keV)	Natural (%) Abundance	Experiment
48Ca	4274.4	0.187	CANDLES
76Ge	2039.0	7.8	Heidelberg-Moscow, GERDA MAJORANA
82Se	2995.5	9.2	SUPERNEMO, LUCIFER
96Zr	3347.7	2.8	
100Mo	3034.4	9.6	NEMO3, MOON
116Cd	2809	7.5	COBRA
130Te	2527.0	34.5	COBRA, CUORE, SNO+
136Xe	2457.8	8.9	EXO, KamLAND, XMASS
150Nd	3367.7	5.6	DCBA

Table 1.1: Table of some known double beta decay isotopes alongside their Q-value, the natural abundance of that isotope and some of the experiments using it for a neutrinoless double beta decay search.

helicity. If the neutrino is a Majorana particle, the right-handed anti-neutrino can act as a left-handed neutrino which can then produce a W boson and a negative helicity electron, inducing the second beta decay. This process, thus, has two requirements, that neutrinos and anti-neutrinos are identical aside from helicity, i.e. Majorana particles, and that the neutrinos have mass. It is due to energy required for the helicity flip and the neutrino's low mass that this process is heavily suppressed relative to the two neutrino process.

The process is especially interesting since, as well as providing confirmation of the Majorana-Dirac nature of neutrinos, the rate is proportional to the effective Majorana mass of the neutrinos. Hence, a discovery of $0\nu\beta\beta$ would provide a measurement of the neutrino mass. The rate can be found as[24]:

$$\frac{1}{T^{0\nu\beta\beta}_{\frac{1}{2}}} = G^{0\nu}(Q,Z)|M^{0\nu}|^2 m^2_{\beta\beta} \tag{1.2}$$

where $G^{0\nu}(Q,Z)$ is a phase space factor dependent of the Q-value of the transition, Z is the nuclear charge, $M^{0\nu}$ is the nuclear matrix element and $m_{\beta\beta}$ is the effective Majorana mass of the neutrinos, defined as a sum over the neutrino masses:

$$m_{\beta\beta} = |\sum_{i=1}^{3} m_i U_{ei}^2| \tag{1.3}$$

The matrix element gives the transition rate of the interaction within the nucleus and must be calculated analytically. Its value can depend strongly on the model and assumptions used to calculate it. This means that a global search for double beta decay must use a variety of isotopes, as measurements of multiple isotopes are required in order to factor out the uncertainty on the model to find $m_{\beta\beta}$. It is also the case that no one isotope can be strongly preferred over the others due to the uncertainty in $M^{0\nu}$.

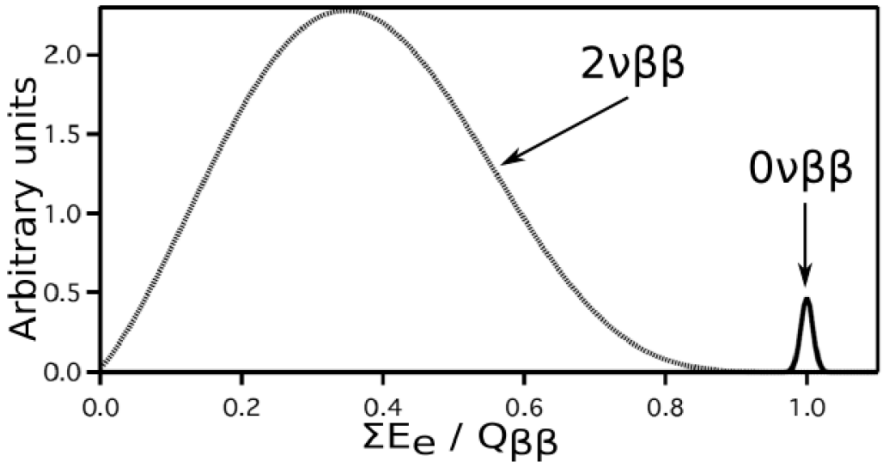

Figure 1.4: Generic energy spectrum showing the energy spectrum for $2\nu\beta\beta$ as well as the $0\nu\beta\beta$ peak[35].

As shown on Figure 1.4, the experimental signal for neutrinoless double beta decay is a peak or shoulder, depending on the energy resolution of the experiment, at the endpoint of the two neutrino double beta decay spectrum. Since the $0\nu\beta\beta$ is heavily suppressed relative to that of the $2\nu\beta\beta$ spectrum, this is expected to be small and so a good energy resolution is required to distinguish the 0ν peak. Also preferred is a high end point, to raise signal above natural radioactive backgrounds, and a large mass of the isotope, either through a high natural abundance or through enrichment.

Due to the difficulty in measuring $0\nu\beta\beta$, there are currently no undisputed measurements and instead upper limits on the effective Majorana mass have been set. Some members of the Heidelberg-Moscow experiment have claimed a measurement of $0\nu\beta\beta$ with a mass of 0.32 ± 0.03 eV[36]. This claim is widely disputed and will be checked by the current generation of experiments, particularly GERDA[37] which uses the same germanium crystals, removing any uncertainty in the matrix element, and is expected to produce results soon.

Current limits on $0\nu\beta\beta$ have been set by the NEMO3 experiment, using the isotopes ^{100}Mo and ^{82}Se to achieve limits of the neutrinoless double beta decay half-life $T_{\frac{1}{2}}^{0\nu\beta\beta} > 2.7 \times 10^{22}$ yr and 1.5×10^{22} yr respectively[38]. The NEMO3 detector uses thin foils made of enriched isotopes placed in a tracking detector. This will be upgraded to a new experiment, SUPERNEMO, which will investigate ^{82}Se using several modules, the first demonstrator model of which is to begin running in 2014[39], aiming towards an eventual lifetime measurment of 10^{26} years and a mass sensitivity of 50 meV.

A limit has been set on $0\nu\beta\beta$ with ^{130}Te by CUORICINO, which consists of TeO_2 bolometers, shielded from radioactive backgrounds, which measure the energy deposition by rises in temperature. It found $T_{\frac{1}{2}}^{0\nu\beta\beta} > 2.8 \times 10^{24}$ yr at 90% C.L which corresponds to mass of 300-710 meV[40]. This will be upgraded to CUORE, which is expected to have a sensitivity of down to 40-100 meV[41].

The KamLand-Zen and EXO experiments both use xenon as a double beta decay isotope. KamLAND-Zen uses xenon loaded into liquid scintillator while EXO uses liquid xenon, enriched to over 80 % ^{136}Xe, in a time projection chamber. These have both recently released limits of $T_{\frac{1}{2}}^{0\nu\beta\beta} > 2.0 \times 10^{25}$ yr at 90% C.L for KamLand-Zen[42] and $T_{\frac{1}{2}}^{0\nu\beta\beta} > 1.6 \times 10^{25}$ yr at 90% C.L for EXO[43] respectively. The KamLAND-Zen paper combines these to give a lifetime limit of 3.4×10^{25} year with an upper limit of the neutrino mass of $m_{\beta\beta}$ of 120-250 meV at 90% CL, depending on the matrix element used.

As part of its physics goals, SNO+ will undertake a search for $0\nu\beta\beta$, using ^{130}Te with an initial loading of 0.3%, expecting to achieve a sensitivity approaching 50 meV. The second phase of the experiment will aim to increase the loading to percentage level loadings of tellurium, pushing the sensitivity further through the inverted hierarchy. The design of the SNO+ detector will be discussed in more details in the oncoming chapters.

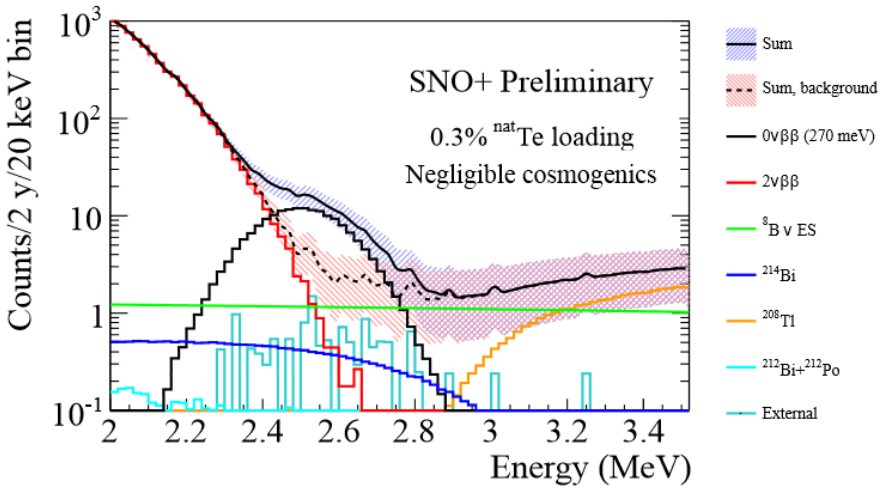

Figure 1.5: Expected signal and backgrounds for $0\nu\beta\beta$ in SNO+ assuming 0.3% loading of tellurium, after two years of data taking[44]. Error bands represent statistical errors (Poisson) at 68% CL.

Shown on Figure 1.5 is the expected reconstructed energy spectrum of signal and backgrounds in SNO+ at 0.3% loading of tellurium. This plot assumes a majorana neutrino with $m_{\beta\beta}$ of 270 meV. It also assumes that cosmogenics can be purified to such levels that they can be neglected. It uses the results of alpha and coincidence tagging to reduce the ^{212}Bi-^{212}Po and ^{214}Bi-^{214}Po by a factor of greater than 99% and ^{208}Tl by a factor of 97%. It assumes a fiducial radius of 3.5 m and an external background tag, described in Chapter 6 of this thesis, is applied, reducing external backgrounds by a factor of two[45].

As can be seen, the main background in the region of interest is the $2\nu\beta\beta$ spectrum, with the $0\nu\beta\beta$ peak appearing as a shoulder on the end. It is this that leads to the requirements for a good energy resolution. Also seen are the

solar ^{8}B neutrinos in green, which are an irreducible background, and the external backgrounds in light blue. The external backgrounds reconstructing in the region of interest will depend on the fiducial volume chosen so the use of a technique to identify and tag these backgrounds, as described in Chapter 6, would allow a larger active volume of the detector to be used.

1.4 Invisible nucleon decay

Another non-standard interaction required in many beyond Standard Model theorys is that of nucleon decay. Many Grand Unified Theories (GUTs) result in a symmetry between baryons and leptons and so can use the violation of baryon or lepton number as a way of explaining the matter-antimatter asymmetry of the universe. This would imply that the proton, and the neutron when bound in the nucleus, would be able to decay, albeit with a heavily suppressed rate. Nucleon decay has not yet been observed but several experiments have set limits on the lifetime which helps to constrain the theoretical models.

In the simplest extensions to the Standard Model, the minimal SU(5) GUTs, the nucleons are expected to predominantly decay to pions, e.g. $p \rightarrow e^+ + \pi^0$. Depending on the theory, this typically had a lifetime of 10^{29} to 10^{31} years. Due to the long lifetime, large water Cherenkov detectors such as IMB and Super-Kamiokande were built. These provided a large sample size of protons in the water as well as allowing the use of Cherenkov signal to distinguish different particle types. IMB, which ran from 1983 to 1990, was able to place a limit of 5.5×10^{32} years at 90 % C.L. on this decay mode[46] while, as of 2012, Super-Kamiokande has set a limit of 1.29×10^{34} years[47].

The addition of supersymmetry to GUTs can suppress the lifetime further to 10^{33} years. In these cases, the main decay mode can be to a final state containing kaons, e.g. $p \rightarrow K^+ + \nu$ or $p \rightarrow K^0 + \mu^+$. The Super-Kamiokande experiment

has led searches for these modes, setting limits of 6.7×10^{32}[48] and 1.6×10^{33} years[49] respectively.

More generic nucleon disappearance events, known as 'invisible nucleon decay', have also been investigated. In these modes, the decay products of the nucleon are not detected, for example, if the nucleon decays to 3ν[50]. Instead, the experiment searches for the decay products of the unstable nucleus left by the disappearance of a nucleon.

The SNO experiment looked for invisible nucleon decay for the decay of a nucleon in ^{16}O in the heavy water, which would produce a gamma of energy 6-7 MeV as the nucleus relaxes to its ground state. A limit of $\tau_{inv} > 2 \times 10^{29}$ years was measured[51]. In 2006, the KamLAND experiment improved this by looking for decays in ^{12}C in its scintillator, setting a limit of 5.8×10^{29} years on the decay of a single nucleon to invisible modes, $n \rightarrow inv$, and of 1.4×10^{30} years on two nucleon decay, $nn \rightarrow inv$[52].

Chapter 2

The SNO+ experiment

Situated in SNOLAB, Canada, the SNO+ experiment is a new multi-purpose liquid scintillator detector. It is based upon the SNO detector and infrastructure with some upgrades necessary for the use of scintillator rather than heavy water. The use of scintillator dramatically increases the light produced by events in the detector compared to the use of heavy water. This light is predominantly produced from scintillation rather than the Cherenkov process so the directional information of the event is lost but the greater statistics available mean the energy threshold of SNO+ will be lower, allowing it to probe different physics such as low energy solar neutrinos. In addition, by loading in an appropriate isotope into the scintillator, the detector will be able to search for neutrinoless double beta decay.

The SNO detector consists of 6 m radius acrylic vessel, the AV, contained within a cavern in SNOLAB as shown in Figure 2.1. During the running of the experiment, this will be filled with liquid scintillator, the nature of which is discussed in more detail in Chapter 3. During SNO, the AV was supported from the deck on top of the cavity by 10 rope loops. With the addition of the scintillator, which will be less dense than the surrounding water shielding, it will also require hold-down ropes to prevent the AV from floating upwards.

The AV is surrounded by approximately 9500 photomultiplier tubes (PMTs)

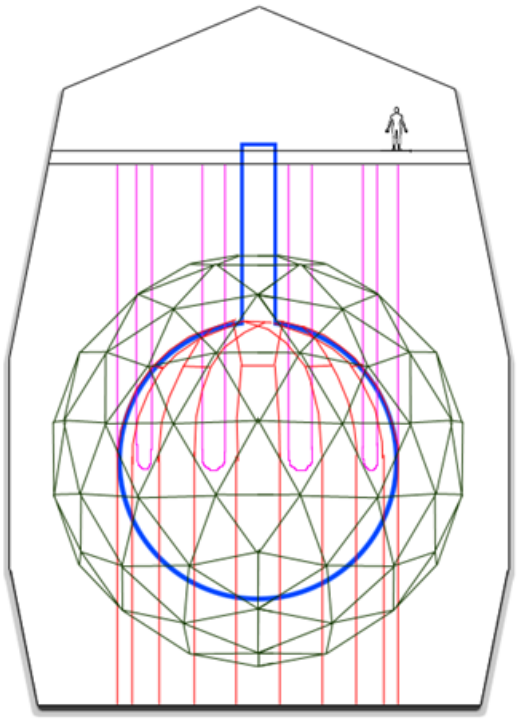

Figure 2.1: Diagram showing a drawing of the SNO+ detector in position in the cavity. The acrylic vessel is shown in blue, suspended from the deck by the hold-up ropes in pink and held in position by the hold-down rope net in red. The PMT support structure (PSUP) is shown in dark green.

held on a stainless steel PMT support structure (PSUP). This is itself supported by 15 stainless steel cables from the deck. The volume between the PSUP and AV will be filled with water to act as shielding, preventing external backgrounds from the PSUP and PMTs from reaching the detector. The SNO+ cavern around the PSUP will also be filled with water to shield against backgrounds from the rock. The cavity walls and floor are lined with concrete and urylon liner to prevent radioactivity from the rock leaching into the cavity water shielding. SNOLAB is located 2km underground, which acts as an overburden of 6000 mwe (metres of water equivalent), reducing the amount of cosmic muons to around 70 per day passing through the detector[53].

2.1 Detector upgrades

Among the upgrades to the detector for use in SNO+ is the addition of hold-down ropes, required as the scintillator is less dense than the surrounding water shielding and so the AV will tend to float upwards. To solve this, a hold-down rope net of 20 interwoven $1\frac{1}{2}$" tensylon ropes has been laid over the top of the AV and fixed to the cavity floor[54]. In addition, the vectran hold-up ropes from SNO were replaced with $\frac{3}{4}$" tensylon ropes.

A new cover gas system has been developed for SNO+ to prevent radon entering the detector from the mine air[55]. The system used on SNO would be unable to meet the background requirements for SNO+ so a new system was developed which uses a series of low-radon nitrogen filled bags. As the pressure of the air on deck changes, clean air will flow between these bags and the detector, compensating for any fluctuations in the air pressure on deck and preventing radon from the mine air contaminating the detector.

The processing and purification system used in SNO has been redesigned and redeveloped for use with scintillator. This takes into account the more stringent radiopurity requirements for the SNO+ scintillator, the different backgrounds that will be present and the new techniques developed to remove them as well as replacing any materials that were found to be incompatible with the scintillator.

During SNO, it was found that there was a split in the urylon liner on the cavity floor and so this has been relined. Work has also been done in cleaning the inner surface of the AV. This aims to remove any radioactive backgrounds from dust and particles that may have settled on the AV surface during its time left unfilled during the intermission between SNO and SNO+.

2.2 SNO+ electronics

The observables in a SNO+ event are the time and charge of each PMT hit. When a pulse is produced by the PMT, it is read out by the PMT interface card (PMTIC) and sent to the front end card (FEC) which determines whether the channel crosses the discriminator threshold. The FEC then calculates the time and charge recorded on the PMT. These appear as a single time value, TAC, and as three different charge values, found by integrating the pulse. The charges are given as QHL and QHS, which both use high gain with long and short integration times, respectively, and QLX, which uses a low gain and long integration time. The QHS can be considered as describing the size of the pulse that caused the PMT to trigger while QHL takes into account the late and scattered light as well.

The analogue master trigger card (MTCA) sums the triggers of all PMT channels within certain windows, e.g. the Nhit100 trigger, which sums all PMTs firing in a 100 ns period. This information is passed to the digital master trigger card (MTCD) which compares to the trigger thresholds and determines if a global trigger (GT) of the detector should be issued. If no global trigger occurs within a set period, approximately 400 ns, the TAC will reset and the PMT hit will not be associated with an event[56]. An overview of the trigger system is shown on the diagram on Figure 2.2.

Since SNO, much of the electronics has been updated to provide added functionality. In addition, some of the PMTs, known from SNO to be faulty, have been repaired and replaced.

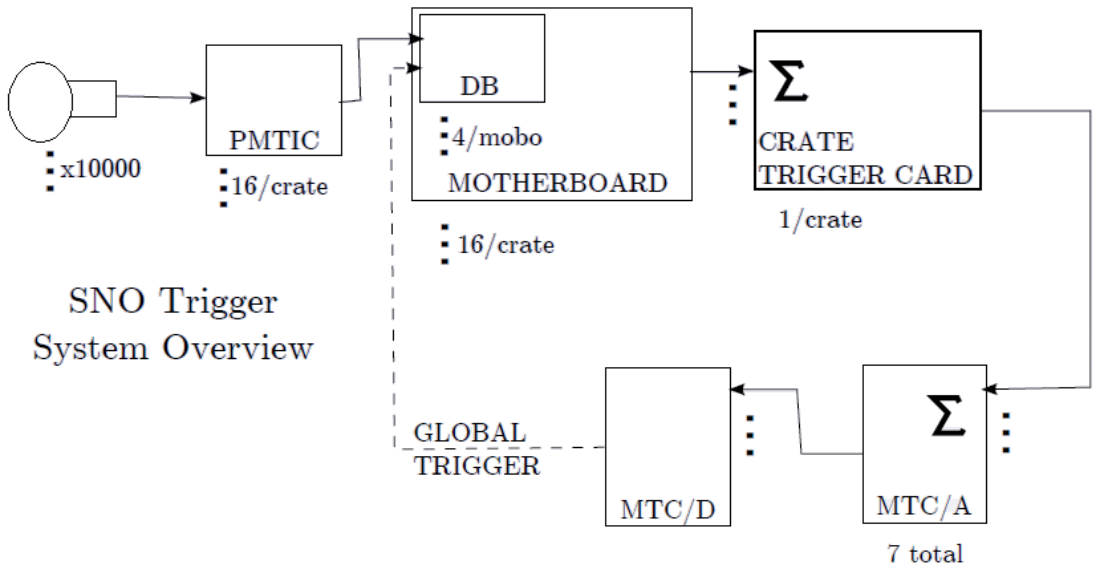

Figure 2.2: Diagram showing the SNO+ trigger system, adapted from[56]. The output of the PMT is read out by the PMT Interface card (PMTIC) and passed to the daughterboard (DB) which caculates timing and charge which is then read out by the front end card (FEC). The crate trigger card (CTC) sums the triggers for a particular crate and passes this to the analogue master trigger (MTCA) which combines this information for all crates. The digital master trigger card (MTCD) compares this to the trigger thresholds to decide whether a global trigger is issued.

2.3 Calibration in SNO+

Amongst the sources that will be used in SNO+, several have been refurbished for use in scintillator and other new sources have been developed to probe the lower energy scale of SNO+. These sources will be required for the calibration of the PMTs and electronics, continuous monitoring of the scintillator optical properties as well as the calibration of the position and energy reconstruction.

Sources that have been developed include several tagged sources, which use either a PMT inside the source or coincident decay to tag the radioactive decays from that source. These include a ^{60}Co source, producing a 2.5 MeV γ, a ^{48}Sc source with a 3.3 MeV γ, a ^{24}Na with a 4.1 MeV γ and, refurbished from SNO, a ^{16}N source producing a tagged 6.1 MeV γ. Other sources under development are an AmBe neutron source and ^{90}Y and ^{8}Li beta sources.

Another calibration source undergoing refurbishment from SNO is the Laser-

ball system which uses a light diffusing sphere coupled to a nitrogen dye laser to produce an isotropic source of light at a range of possible wavelengths.

These sources will be deployed into the scintillator in the inner volume of the detector. To maintain cleanliness, the sources are contained within a sealed 'glove box' above the AV neck in the Deck Clean Room. When in use, sources will be lowered into the detector, as shown in Figure 2.3, suspended from an umbilical cable and positioned in three dimensions using a combination of the umbilical and a set of calibration side ropes. This system has been updated from that used in SNO due to the necessity for material compatibility with the scintillator. To this end, the side ropes have been made of tensylon and the umbical has been re-designed out of tygothane[57].

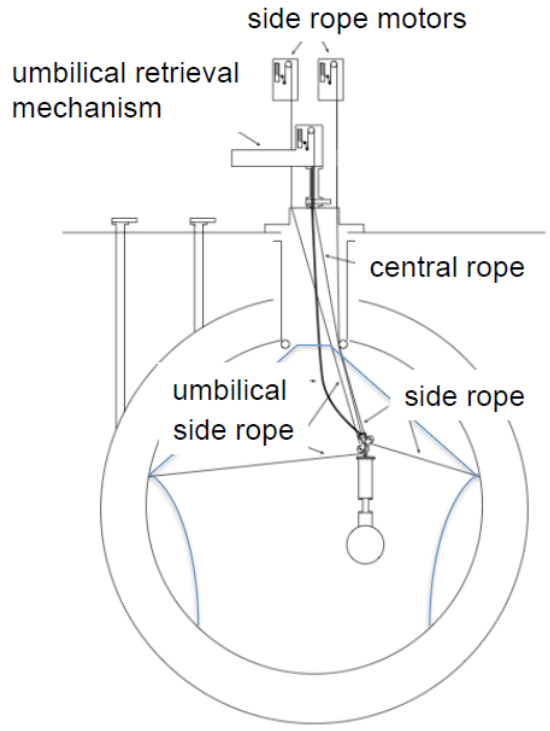

Figure 2.3: Diagram showing an example of a deployed source in SNO+, its position controlled by the calibration ropes and umbilical.

A set of 6 cameras have been installed on the edge of the PSUP, looking inwards, and will be used to determine the position of the deployed sources. This will be possible using an LED placed on the source or umbilical. The cameras

can pick up small amounts of light over a long exposure time and so triangulate the position of the calibration source to within an accuracy of less than 1 cm[58]. The camera system system will also be equiped with its own light source, again mounted on the PSUP, enabling it to take pictures of the detector with no source present, which will be used to monitor the hold-down rope net.

Since the radiopurity requirements of the SNO+ scintillator will be higher than those of the D_2O in SNO, a system of calibration fibres, known as the Embedded LED/Laser Light Injection Entity (ELLIE) system, have been installed on the edge of the PSUP as shown on Figure 2.4. These allow the detector properties to be monitored without having to deploy a calibration source and so reduce the risk of introducing backgrounds into the scintillator. This will consist of three components to measure timing (TELLIE), scattering (SMELLIE) and monitoring the attenuation (AMELLIE)[59][60].

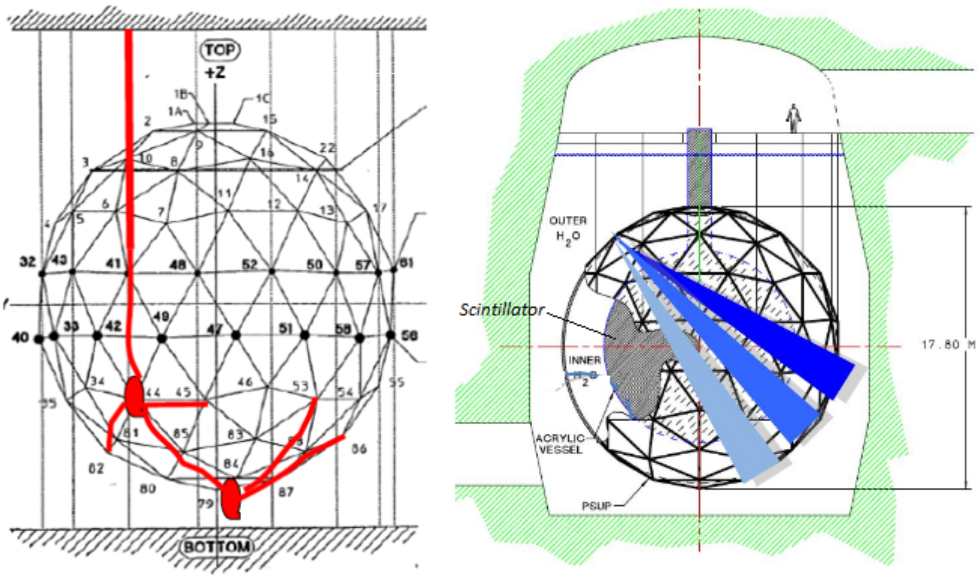

(a) Example of routing of an ELLIE fibre from deck to final position

(b) SMELLIE node with beams in 3 directions across detector

Figure 2.4: Drawings showing a) the routing of a typical ELLIE fibre along the PSUP from deck to its mounting position on the PSUP and b) a SMELLIE node with collimated beams in 3 different directions.

The TELLIE system consists of wide-angled beams shone across the detector

from 92 different positions on the PSUP, giving full coverage of the PMTs, using light from LEDs of a single wavelength. This will be used to calibrate the timing offsets of the PMTs, a job that was done using the Laserball during SNO. It is also possible that, given its full coverage, the TELLIE system could be used to determine the position of deployed sources by using the shadowing effect of the body of the source.

The SMELLIE system consists of 12 fibres, mounted at 4 positions on the PSUP, each position containing collimated beams at three angles, 0°, 10° and 20° relative to the centre of the detector. This will use light, produced by a system of lasers, at 4 different wavelengths between 375 nm and 500 nm. By analysing the position and time of PMT hits relative to the initial direction of the beam, it should be possible to measure the scattering of the scintillator. The multiple positions and directions of the beams will provide a check against systematics.

The AMELLIE system has 4 different injection positions, each with wide-angled beams in two different directions and uses light from LEDs at multiple wavelengths. This produces a beam which covers a sizeable area of the detector and so allows in-situ monitoring of the stability of attenuation of the scintillator.

2.4 Monte-Carlo simulation

SNO+ uses a Monte-Carlo simulation known as RAT, Reactor Analysis Tools. This was originally developed for use in the Braidwood collaboration, based on software which simulated a generic liquid scintillator experiment with a KamLAND-like geometry, and was adapted for use in a number of experiments including SNO+ and the dark matter experiments DEAP and CLEAN, each now with their own distinct branch of the code. This is written primarily in C++, with some python, with the use of Geant4 libraries to simulate physical processes and ROOT libraries to store data.

Chapter 3

Scintillator Monte-Carlo

During the course of its running, SNO+ is planned to run using both unloaded scintillator, for initial calibration and commissioning of the detector as well as for measurements of solar neutrinos, and scintillator loaded with a double beta decay isotope. It is important that the scintillator is modelled accurately in the Monte-Carlo simulations. Ideally, the scintillator should be described by input parameters which can be measured both in the lab and by in-situ monitoring as the experiment progresses, and give outputs that match the behaviour observed in the detector.

To this end, the processes simulating the creation and tracking of optical photons through the scintillator were modified and verified. The underlying physics of the code was correct, but this was modified to a multi-component model which matches the measured data and should be easier to maintain.

Changes were made to how the data is stored in the database and read into the simulation as well as modifications to the processes of scattering, absorption and re-emission. This was done after extensive discussion with others in the Scintillator Monte-Carlo working group[61].

3.1 Composition of the scintillator

The SNO+ scintillator will consist of several components that will vary in composition depending on the phase of the experiment and the physics being investigated.

In the 'solar phase' of the experiment, it will consist of a bulk scintillator linear alkylbenzene, 'LAB', along with a wavelength shifter 2,5-diphenyloxazole, 'PPO'. Charged particles will excite the LAB, producing scintillation photons in the 300 nm wavelength region but, left by itself, the LAB will quickly re-absorb them. However PPO absorbs strongly in the 300-350 nm range and emits in the 350-450 nm region. This has the action of lifting the photons out of the low wavelength region in which LAB and PPO are strong absorbers and up to higher wavelengths which coincide with the maximum sensitivity of the PMTs and where the chance of absorption is lower. The scintillation process and the action of the wavelength shifter is discussed further below.

During this phase, the detector will run initially in order to take measurements of backgrounds, run calibrations as well as perform checks on both the detector hardware and simulations. There will also be physics measurements in the form of low-energy solar neutrinos, reactor neutrinos and geo-neutrinos. After the double beta phase is complete, the detector will return to this setup to take longer measurements of the solar neutrinos.

In the 'double beta decay phase', an isotope will be added to the scintillator in order to search for double beta decay. The isotope may bring additional optical properties such as absorption or scattering. Depending on the nature of these optical properties, it may be necessary to run with a secondary wavelength shifter in order to avoid the additional low wavelength attenuation of photons. This idea is discussed in more detail in Chapter 4.

To this end, any modelling of the scintillator should be as generic as possible to allow the simulation to be easily modified for use in the various phases.

3.2 Physics processes within the scintillator

In order to model the properties of the scintillator, the physics processes which can affect optical photons need to be considered. The wavelength range of sensitivity for the SNO+ photomultiplier (PMT) tubes is approximately 200 to 600 nm as shown on Figure 3.1. In this range, photons may be created by either scintillation or the Cherenkov process.

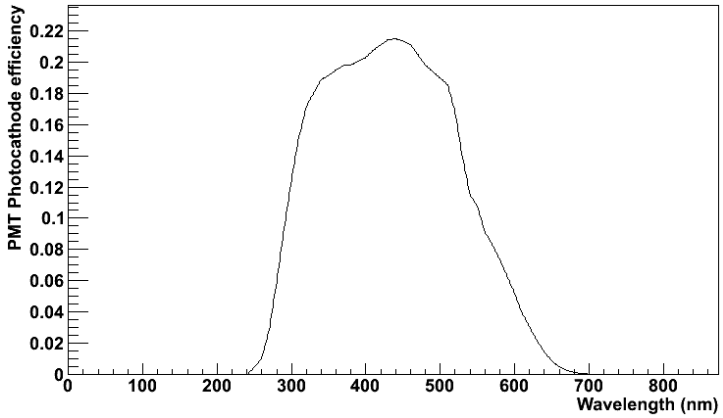

Figure 3.1: Wavelength dependence of the photocathode efficiency of a SNO+ PMT.

As an electron travels through the scintillator, it will deposit its energy as it excites and ionises the surrounding matter. As the scintillator molecules de-excite back to the ground state, some of this energy will produce photons via fluorescence. In the case of the SNO+ scintillator, it is the LAB which will be excited.

The photons are produced with a time delay given by an exponential form $\exp(-\frac{t}{\tau})$, where τ is the fluorescence decay time. The fluorescence will have the same decay time, emission spectrum and quantum efficiency regardless of its initial excited state, due to internal conversion within the molecule[62].

Slower emission of photons may also occur via phosphorescence or delayed fluorescence, which occurs as the excited singlet decays first to a meta-stable triplet state via a radiationless transition and then to the ground state, emitting a photon[62].

The amount of light produced along a particle track can be found using:

$$\frac{dL}{dr} = \frac{L_0 \times \frac{dE}{dr}}{1 + kB \times \frac{dE}{dr}} \tag{3.1}$$

where L_0 is the light yield of the scintillator, $\frac{dE}{dr}$ is the energy the particle deposits per unit length and kB is Birks' constant.

Other charged particles, such as α particles, will also deposit their energy via molecular excitation and ionisation. γ radiation will deposit energy as it Compton scatters off electrons or undergoes pair production, producing secondary electrons which will then excite the scintillator. Meanwhile, neutrons will lose their energy by scattering or absorption with nuclei in the scintillator, producing recoil protons or γ rays as the nuclei de-excite. For heavier particles such as protons or α s, the number of photons produced will be lower due to the quenching effect. Quenching occurs as the number of ionised atoms around the charged particle saturates at high values of $\frac{dE}{dr}$, i.e. if the particle deposits a large amount of energy over a short distance, and so it requires more energy to produce further photons. This is quantified by the parameter kB in equation 3.1.

Due to overlap between its absorption and emission spectra, the LAB may self-absorb the light it produces. To reduce this, a wavelength shifter, PPO, is used. It is then the case that the excited energy of the LAB molecule will be transferred to the PPO, either by radiative or non-radiative transfer. It will then be emitted via the PPO emission spectrum, above the absorption of the LAB.

Photons may also be produced as Cherenkov light. As charged particles pass through a medium faster than the phase velocity of light in that medium, they will polarise the molecules of the medium. When the molecules then relax, they emit radiation as a constructively interfering wavefront at an angle characteristic of the speed of the particle [63].

As a photon travels through the scintillator, it may undergo scattering or ab-

sorption. Scattering by individual components of the scintillator is not easily separable, and so an overall bulk scattering for all components is considered. Benchtop measurements of the scintillator scattering at Queen's University, Canada, and BNL are used as inputs to the simulation. These measurements show a $\frac{1}{\lambda^4}$ wavelength dependence and $1+\cos^2\theta$ angular dependence[64], consistent with the Rayleigh Scattering process.

If the photon is absorbed, its behaviour will depend on the component of the scintillator by which it was absorbed. If absorbed by the LAB or a wavelength shifter, it may be re-emitted as a longer wavelength photon. If absorbed by the double beta decay isotope, the photon does not get re-emitted and the energy is lost to the detector. As mentioned previously, excitations of the LAB are usually transferred to the PPO so the emission spectrum of the PPO is used for both LAB and PPO. However, these components will still have different re-emission efficiencies and emission time delays.

3.3 Input parameters to the simulation

The inputs to the simulation should be parameters that can be physically measured. They should also be easy to change and maintain. These are compiled in Table 3.1, showing which of these properties are measured for the scintillator as a whole and which must be considered for each component separately.

Overall	Each Component
Light yield	Absorption Length
Refractive index	Re-emission timing
Birks' constant	Re-emission spectrum
Scintillation timing	Re-emission probability
Scintillation emission spectrum	
Scattering length	

Table 3.1: Table of the measured properties that describe the scintillator. These are divided into two columns showing whether this property is measured for the scintillator as a whole or for each individual component.

A 'scaling factor' was also introduced, which scales the overall size of the scattering or absorption of each component, making it easier to investigate the effect of changes in the scintillator properties on the detector response.

3.3.1 Light yield

The light yield is given as a single value for the scintillator and gives the total number of photons produced per MeV of energy deposited in the scintillator when integrated across the wavelength range of 200 to 800 nm. The relative intensity at which the photons are emitted at different wavelengths is given separately as the scintillation emission spectrum. This value comes from lab measurements at UPenn[65] and is dependent on the composition of the scintillator. When the detector is commissioned, this value will be tuned to match the observed in-situ light yield of the scintillator during calibration.

3.3.2 Refractive index

The refractive index of the scintillator is given as a wavelength dependent array which spans the range 200 to 800 nm in 2nm steps, shown on Figure 3.2. This is based on lab measurements[66] of the scintillator at UW.

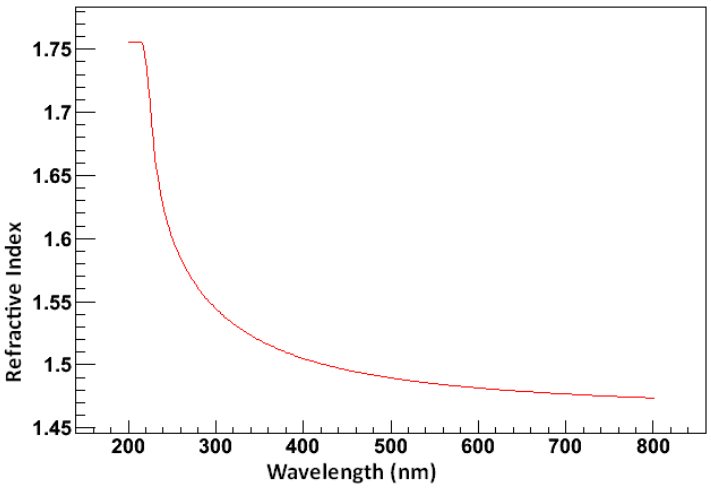

Figure 3.2: Refractive index of the unloaded scintillator.

3.3.3 Birks' constant

Birks' constant is given as a single value of 0.0798 for unloaded scintillator and 0.0719 for Nd-loaded scintillator, coming from measurements in the lab at UW[67]. A measurement of Birks' constant for Te-loaded scintillator is currently underway at Dresden but, within this thesis, it assumed to be equal to that of the neodymium loading.

3.3.4 Scintillation timing

The scintillation timing is given separately for alphas and betas based on measurements of the deoxygenated scintillator at Queens[68]. These are each given in the RAT database as a combination of three exponential components as shown in Table 3.2.

	Alphas	Betas
t_1	-3.2	-4.6
t_2	-18	-18
t_3	-190	-156
R_1	0.44	0.71
R_2	0.16	0.22
R_3	0.41	0.07

Table 3.2: The values for characterising the alpha and beta scintillation timing distributions in RAT. These are given as a sum of three exponentials, where t_i is the time constant of each decay in ns and R_i is the relative contribution of that component.

3.3.5 Re-emission timing

The re-emission timing is given separately for each component as an exponential. The values used are based on measurements of the UV excitation of the scintillator[69] and are shown in Table 3.3.

	LAB	PPO
t_1	-5.8	-1.6
R_1	1	1

Table 3.3: The values for characterising the remission timing distributions in RAT for emission from LAB and PPO. These are given as an exponential, where t_i is the time constant of each decay in ns and R_i is the relative contribution of that component.

3.3.6 Scintillation emission and re-emission spectra

The emission spectrum is given separately for scintillation and re-emitted light. Each component of the scintillator has its own particular re-emission spectrum to allow for multiple wavelength shifters. The emission spectrum from scintillation and the re-emission spectra of PPO and bisMSB, another wavelength shifter which could be used alongside the PPO in certain loadings of double beta decay isotopes, are plotted on Figure 3.3. For the SNO+ scintillator, the same re-emission spectrum is used for both LAB and PPO since light absorbed by the LAB is mostly non-radiatively transferred to the PPO before it is re-emitted. Some of the light may be re-emitted by the LAB but will be almost immediately re-absorbed by the PPO, and so the LAB effectively emits via the PPO. Some of the LAB absorbed light will also not be re-emitted[69].

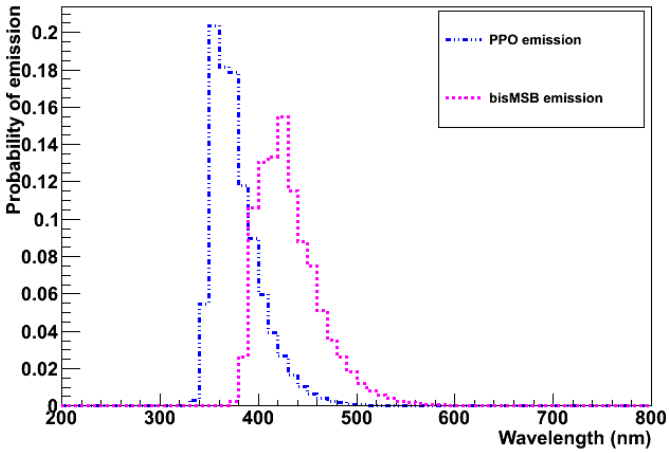

Figure 3.3: Plot of the re-emission spectrum of PPO in blue (same as that of the scintillation from unloaded scintillator) as well as the re-emission spectrum of bisMSB, another wavelength shifter, in purple.

3.3.7 Absorption and scattering lengths

Absorption is given separately for each component as an array of absorption lengths over a wavelength range of from 200 nm to 800 nm. Above 600nm, this was extrapolated out to 800 nm at a constant value due to limitations in the measured data. Since the PMT efficiency is effectively zero at wavelengths this high, as shown on Figure 3.1, this approximation shouldn't make any difference to the results of the simulation. A bin width of 4 nm was chosen in order to catch a peak in the absorption of Nd at 430 nm as shown in Figure 3.4.

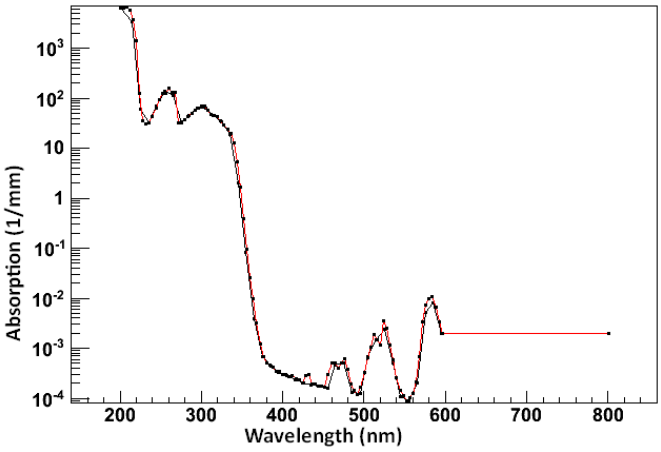

Figure 3.4: Effect of changing the bin size from 10 nm (black) to 4 nm (red) on the total absorption for Nd-loaded scintillator.

The absorbances A are taken from lab measurements of the scintillator mixtures at Queens and BNL. They are then separated into components and converted, from cm and as a power of 10, into the absorption length l_{abs}, in mm, of an exponential by Equation 3.2.

$$A(\mathrm{cm}^{-1}) = \frac{10}{\ln(10) \times l_{abs}(mm)} \tag{3.2}$$

The scattering of the scintillator is based on that of the bulk scintillator, rather than for individual components. It consists of a wavelength dependent array, again taken in 4 nm steps between 200 and 800 nm. This is based on measurements

at Queens of the unloaded scintillator[64], confirmed by further measurements at Brookhaven and Seattle. The absorption spectra, used in RAT, for different loading techniques are described in Chapter 4.

3.3.8 Re-emission probability

The re-emission probability is given as a single value for each component, representing the probability that, given a photon has been absorbed, it will be re-emitted. These values will depend on the concentration of PPO in the scintillator, currently taken to be 2 g/L. LAB has a value of 0.59 based on measurements of energy transfer in the scintillator at Queens by A.Wright[69], while PPO uses 0.8, a value from Borexino[70]. How these values change with the loading of PPO and the effect this has on the performance of the detector is discussed in Chapter 4.

3.4 Coding logic for physics processes

In describing the coding logic used for the scintillator Monte-Carlo, it would be useful to first outline the definitions of some terms and the notation used in the following equations.

The SNO+ Monte-Carlo simulation, RAT, is based on Geant4 and so uses the Geant4 definitions of steps and tracks[71] when discussing the propagation of particles. A step describes the motion of a particle in a straight line until either its properties are changed by a step-ending physical process such as scattering or absorption, or it reaches a geometrical boundary. A track is the combination of these steps from the creation of the particle to the point where the particle is stopped and killed. It should be noted that, in RAT, re-emitted photons exist as separate tracks from that of their parent particle.

In the description of the code below, the following notation is used:

l_{abs_i} - the absorption length of component i

l_{scatt} - the overall scattering length of the scintillator

l_{abs_total} - the overall absorption length of the scintillator

l_{total} - the total attenuation length

f_{scatt} - the fraction of the light that is scattered

f_{abs_i} - the fraction of the absorbed light that is absorbed by component i

3.4.1 Initialisation

Upon run initialisation of a RAT simulation, the input properties are loaded in from the database. Wavelength dependent properties are stored in vectors, ordered in terms of wavelength. In addition, a total attenuation length is calculated as the sum of each component's absorption and the overall scattering length:

$$l_{total} = \frac{1}{\sum_i \frac{1}{l_{abs\_i}} + \frac{1}{l_{scatt}}} \tag{3.3}$$

3.4.2 Track creation

Tracks may be created by either the Cherenkov or scintillation processes. Cherenkov photons are produced using code adapted from the Geant4 Cherenkov process. This runs at the end of each step in a charged particle's track. The number of photons emitted per mm is found using:

$$370Z^2(E_{max} - E_{min} - \frac{1}{\beta^2}\int \frac{dE}{n^2}) \tag{3.4}$$

The code then finds the mean number of photons emitted in the step by multiplying this by the step length, and then draws an integer number from a Poisson distribution with this mean to get the number of photons produced in the step. Each photon is then generated, sampling an appropriate energy, a direction on the Cherenkov light cone and a polarisation. The photon is then created at a random

position and time along the step of the initial particle.

The scintillation process runs at the end of each step, finding the energy deposited in the scintillator in that step, E_{dep}, and dividing by step length to get $\frac{dE}{dx}$. The quenched energy deposited, E_{quench}, is then found as:

$$E_{quench} = \frac{E_{dep}}{1 + kB \times \frac{dE}{dx}} \tag{3.5}$$

The mean number of photons is then found by multiplying the quenched energy by the light yield, given in photons per MeV. The total number of photons produced is the found by drawing from a Poisson distribution with this mean, for low mean numbers of photons, or from a Gaussian for higher means. Each photon is then generated with a wavelength drawn from the scintillation emission spectrum, an isotropic direction and an emission time delay sampled from the overall scintillation timing, specific to the initial particle. The photon is then placed at a random position along the initial particle track.

3.4.3 Track propagation, absorption and scattering

Optical photon tracks are propagated through the scintillator using Geant4. To determine whether or not a photon is attenuated by scattering or absorption, a customised physics process 'OpAttenuation' is used, the length of which corresponds to the total attenuation length, i.e. the distance a photon travels before it is either scattered or absorbed.

The step may end as the photon undergoes scattering, absorption or transportation into a new medium. The distance that a photon will travel before one of these occur is determined using the total attenuation length at that photon's wavelength. A random number is drawn against an exponential distribution of this total length to get the length that this photon travels in the step.

If this distance is longer than the straight line path the photon will travel to

the next material boundary, the track will end at the boundary between the two media. Geant4 will then use the refractive indices of the two media to check for refraction or total internal reflection. It then creates a new step, propagating the track forward with a new direction determined by its refractive index.

If the track does not pass into a new medium, the step ends after travelling the calculated distance. It then determines whether the photon was scattered or absorbed by calculating the fraction of light at this wavelength which will be scattered:

$$f_{scatt} = \frac{l_{total}}{l_{scatt}} \tag{3.6}$$

A random number is then drawn and compared to this scattering fraction. If the random number is less than the scattering fraction, the track has been scattered. Otherwise, the track has been absorbed. If the track has been scattered, it is assigned a new direction drawn from the Rayleigh scattering $1+\cos^2\theta$ angular distribution. It is also assigned a new polarisation and then the track continues with a new step. If absorbed, the track is marked as having been stopped and will be picked up again later for possible re-emission.

3.4.4 Re-emission

After all tracks have been stopped, the code deals with re-emission of the absorbed photons. First, it determines by which component the photon has been absorbed. It does this by calculating the total absorption length:

$$l_{abs\_total} = \frac{1}{\sum \frac{1}{l_{abs\_i}}} \tag{3.7}$$

The fraction of the photons that are absorbed by a particular component i will be given by:

$$f_{abs\_i} = \frac{l_{abs\_total}}{l_{abs\_i}} \tag{3.8}$$

It then calculates for each scintillator component, i=$(1, ...N)$, the probability, P_i, that, for component i, the photon is aborbed by any component with index from 1 to i, i.e. for component 2, $P_2 = f_{abs\_1} + f_{abs\_2}$. This has the property that for i=N, the probability of having been absorbed by any component will be 1; this ensures that the photon must always be absorbed, an important safety check!

$$P_i = \sum_{j<i} f_{abs\_j} \tag{3.9}$$

Next it draws a random number, ρ, and if $P_{i-1} < \rho \leq P_i$, the photon is absorbed by the ith component. It is then assigned as the component's probability of re-emission which the code then draws a random number against. If the random number is less than the re-emission probability, the photon is re-emitted and so will create a secondary track. Otherwise, the photon is absorbed without re-emission and produces no secondary tracks. If the photon is re-emitted, it is then assigned a direction selected at random from an isotropic distribution. The emission time delay is drawn from the same component's re-emission timing. The wavelength of the new photon is drawn from the component's emission spectrum with the condition that it must draw a new wavelength greater than or equal to that of the initial particle. The new track is then propagated forward.

3.5 Limitations

The code assumes that all the scattering in the detector is due to Rayleigh scattering. This is currently consistent with laboratory measurements of the scattering of both loaded and unloaded scintillators within our wavelength range. For larger molecules, Mie scattering could become an issue and so this is a planned software

update for the future.

Another current assumption is that, for every one photon that is absorbed, the scintillator will only re-emit a single photon, thus ignoring the possibility of a single absorbed photon resulting in more than one re-emitted photon. This is a property of the spin and angular momentum of the singlet and ground states between which the photon de-excites. While it could also be possible for two lower energy photons to be absorbed, resulting in a single higher energy photon being emitted, this is a higher order effect that is not considered in the simulation.

The simulation only considers photons with wavelengths 200 to 800 nm. This is a reasonable approximation, as any higher wavelength photons will be outside the sensitivity range of the PMTs while lower wavelength photons will travel very short distances before being absorbed and re-emitted at higher wavelengths. These will therefore be implicitly included in the light yield of the scintillator.

Also neglected from the model is the effect of thermal broadening. Absorbed photons with energies greater than the size of the band gap will excite the molecule and will be able to be re-emitted at any point on the emission spectrum. For energies just below the band gap, the photon is able to use thermal energy to make up the shortfall and still excite the molecule, re-emitting across the whole spectrum, potentially at a shorter wavelength than with which it was absorbed. For wavelengths much longer than the band gap, the photons aren't actually absorbed by the molecule but instead undergo Raman scattering, shifting to a longer wavelength[72].

However, in this case, the amount of thermal broadening is small since thermal energy at 300K is much smaller than the energy of a 300nm photon. In addition, this process only takes place near the width of band gap which is around 300 nm, a region in which photons will travel only very short distances before being shifted to longer wavelengths anyway. Thus, it is likely that little additional accuracy would be gained by taking measurements and separating these processes in a full

simulation.

3.6 Conclusion

A model has been developed for the SNO+ simulation, which successfully models the creation, transportation and physics processes acting on optical photons within the sensitivity range of the experiment. The model uses input data which has been measured experimentally and will be verified and tuned further during the initial calibration. Continual monitoring of scintillator properties will also take place using calibration systems.

The model can be easily adapted to different scintillator mixtures, which is both of use for the multiple phases of running planned for SNO+ and also in the further development and simulation of new scintillator types to improve the detector sensitivity, as discussed in Chapter 4.

Chapter 4

Application to scintillator development

Using the scintillator model described in Chapter 3, new scintillator mixtures have been simulated in order to test the detector response to different loading techniques. A study is shown of the effect of different concentrations of PPO, the main wavelength shifter to be used in the SNO+ scintillator, on the light yield and ability to reconstruct in unloaded scintillator. This chapter also contains studies performed on the use of tellurium, an alternative isotope to neodymium, as a double beta decay candidate. This involved simulations of the effects of two different methods of loading tellurium into the scintillator and of using a range of different secondary wavelength shifters. This was done with the aim of finding the mixture which maximises the number of PMT hits and so allows a greater amount of loading.

As the loading increases, the absorption of optical photons will increase and so number of PMT hits will drop, worsening the energy resolution and increasing the background events reconstructing within the signal region. Appendix A investigates the effect of the energy resolution on the background levels, assuming 0.3 % loading, and determines that over 150 hits per MeV of deposited energy are

required such that the signal region isn't dominated by two neutrino background. Due to its effect on the reconstruction of external backgrounds, a certain standard of fitted position is also required. The requirements on the position fitters are discussed in detail in section 5.1.3 and require a low radial bias and a resolution of less than 26 cm.

The loading methods and results discussed in this chapter are a work in progress as investigations into the loading are ongoing. Due to a decision by the collaboration not to publicly discuss the method of the tellurium loading at the current time, no details will be given on the nature of the loading technique.

4.1 Optimisation of PPO concentration

Based on initial measurements at Queens, it was determined that the optimal level of PPO loading would be 2 g/L. In order to confirm this, simulations were run using different levels of PPO loading and the effect on the number of hits and on reconstruction was investigated.

In order to run these tests, several assumptions where made. The absorption spectrum of PPO had been measured at a concentration of 1.5 g/L. It was assumed the absorption would scale proportional to the concentration, i.e. doubling the concentration of PPO would double the amount of absorption.

The light yields used at different PPO concentrations were based on measurements at Queens of the light yield of the scintillator with different concentrations of PPO, shown on Figure 4.1[73]. This plot was used to find how the light yield scales with fluor concentration and this was used to convert more recent measurement of the light yield at 2 g/L[65], to different levels of PPO.

The re-emission timing of LAB, which emits through the PPO, will change with the concentration of PPO, as will the probability of re-emission from the LAB. These are shown for various concentrations of PPO in Table 4.1 based on

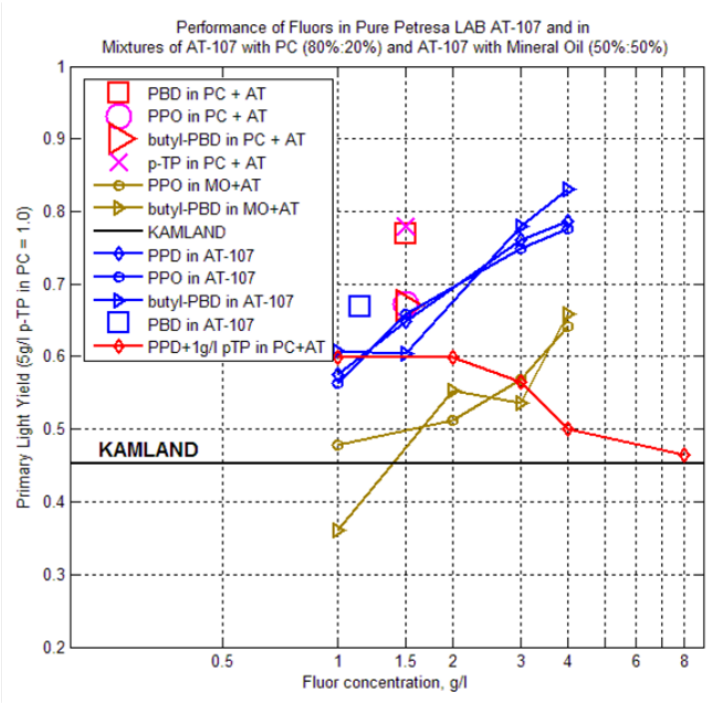

Figure 4.1: Measured light yield of the scintillator with various fluor concentrations based on measurements at Queens[73]. The light yields used in this study were the blue circles which give the change in light yield for LAB (AT-107) with different PPO concentrations.

measurements of the emission timing at Queens. The probability of re-emission from the LAB is found by multiplying the transfer efficiency of LAB to PPO by the probability of re-emission from PPO, measured to be 0.8[69]. With no measured data available, the scintillation timing delay was assumed to be unchanged.

The number of hits (Nhits) per MeV was investigated by simulating 3 MeV electron evenly throughout the detector for each of the different PPO concentrations. Since the re-emission timing becomes slower at lower concentrations, it is also useful to check that the fitters are still able to reconstruct with this new PPO mixture. To test this, the same 3 MeV events were fit using the likelihood fitter described in Chapter 5, re-coodinated to take into account of the change in optics, and the resolution calculated. The results are shown in Table 4.2.

In conclusion, while some additional sensitivity through the increased statistics could be gained by increasing the amount of PPO used, it is likely that the gain

PPO concentration (g/L)	τ_{0x} (ns)	LAB → PPO Transfer Efficiency (%)
32	1.66	92.7 ± 0.1
4	3.2	86.0 ± 0.8
2	5.0	78.2 ± 1.5
1	7.3	67.7 ± 2.3
0.5	9.2	59.3 ± 3.2
0.25	11.6	48.7 ± 5.0
0.1	24.1	-0.06 ± 27.8
0.025	41.5	-82.8 ± 116.5

Table 4.1: Re-emission times and transfer efficiency of LAB, via the PPO, for different concentrations of PPO, based on measurements at Queens[69].

PPO concentration (g/L)	Nhits per MeV	Position resolution (mm)
0.5	345	124
1	425	106
1.5	475	106
2	495	106
4	534	103

Table 4.2: Nhits per MeV found using simulations of different concentrations of PPO. Also shown is the fitter resolution at 3 MeV for each concentration.

available would not be worth the additional cost of doubling the amount of PPO. On the other hand, dropping the PPO concentration only lowers the number of PMT hits by a few percent so, if costs proved prohibitive, it could be possible to lower the PPO level.

While this is true for the unloaded scintillator, the use of a secondary wavelength shifter with the Te-loaded scintillator could change the optimum loading level, depending on the absorption and emission spectrum of the secondary shifter.

4.2 Te-loaded scintillator

Recent work at Oxford, Queens and BNL has suggested that the sensitivity of the SNO+ experiment to neutrinoless double beta decay could be improved by the use of ^{150}Te as a candidate isotope. This is based upon the higher natural abundance of the isotope ^{130}Te, 34%, compared to 5.6% for ^{150}Nd, meaning that enrichment

wouldn't be necessary. Unlike neodymium, the optical properties don't appear to contain any intrinsic absorption peaks, in the region of interest of 300 to 600 nm, meaning that the isotope can be potentially loaded to higher levels of loading and it has a relatively lower two-neutrino double beta decay rate, which acts as one of the major backgrounds at higher loading. Purification and background tagging techniques have been developed to remove or identify many of the other significant backgrounds.

Use of tellurium in the SNO+ detector would involve plans for an initial 0.3 % loading, as an initial proof of concept and to allow analysis of background levels, followed by a larger loading at the level of 3 %.

4.2.1 Different loading techniques

In order to develop this idea further, different loading techniques were developed at BNL and measurements made of their optical properties, including absorption, scattering and re-emission. These were then placed into the SNO+ RAT simulation and their effect within the SNO+ detector was investigated.

In this chapter, two types of Te loading will be considered. The first method (from this point, known as Type A) contained absorption in the 400-450 nm region but also significant additional scattering, shown in Figure 4.2 a). The figure only shows the absorption of the tellurium across a range of wavelengths from 370-440 nm, this is because, outside this wavelength range, the tellurium appeared to have an unphysical value for the absorption length after subtraction of the LAB and PPO contributions. In these regions, the absorption length of the tellurium was assumed to be very long. In order to avoid this absorption and to shift photons to the higher wavelengths where the effects of scattering would be lower, a secondary wavelength shifter, bisMSB, which absorbs in the 400-420 nm region but emits photons at 420-450 nm was used. bisMSB, whose emission spectrum is shown on

Figure 4.3, has a re-emission probability of 0.96 and delay time of 1.4 ns compared to those of 0.8 and 1.6 ns for PPO.

The results in terms of number of PMT hits per MeV are shown in Table 4.3 and the position resolution in Table 4.4, alongside those of neodymium loading. For the Type A form of tellurium loading, it can be seen that it meets the requirements in terms of the number of PMT hits but the scattering noticeably affects the position resolution of the fitter, particularly at higher loadings. A poor position resolution could potentially cause problems with external backgrounds, discussed further in Chapter 6, and so imposes a limit on the maximum loading that could be achieved. However these optics are an artefact of how the tellurium was loaded and come from the surfactant rather than being intrinsic to the tellurium itself and so a different loading technique could improve the situation.

Thus a new loading method (Type B) was developed, which used a different form of surfactant. This had more absorption than the previous model but no additional scattering as shown in Figure 4.2 b). The Nhits per MeV and position resolution are also included in the Tables 4.3 and 4.4.

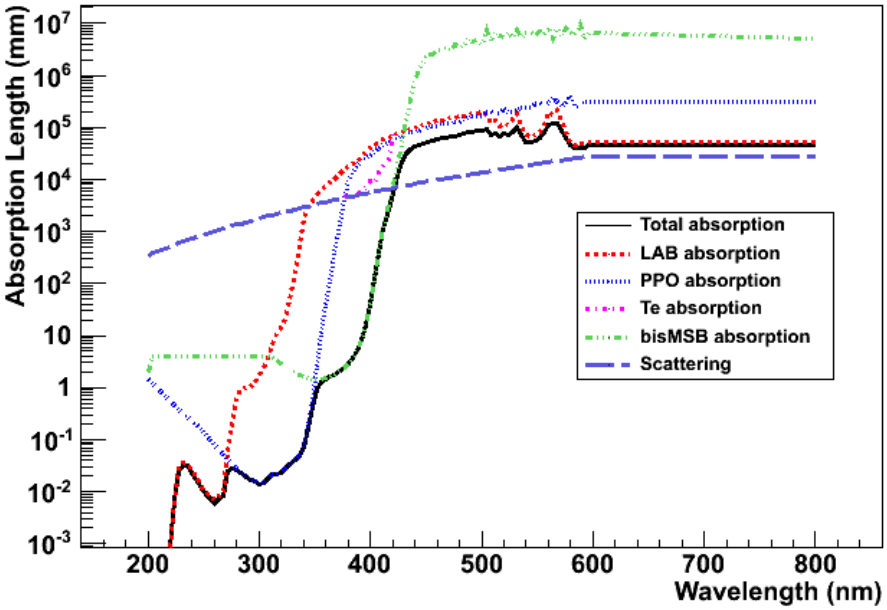

(a) Total absorption for Type A Te-loaded scintillator (at 0.1% loading) with bisMSB as a secondary WLS)

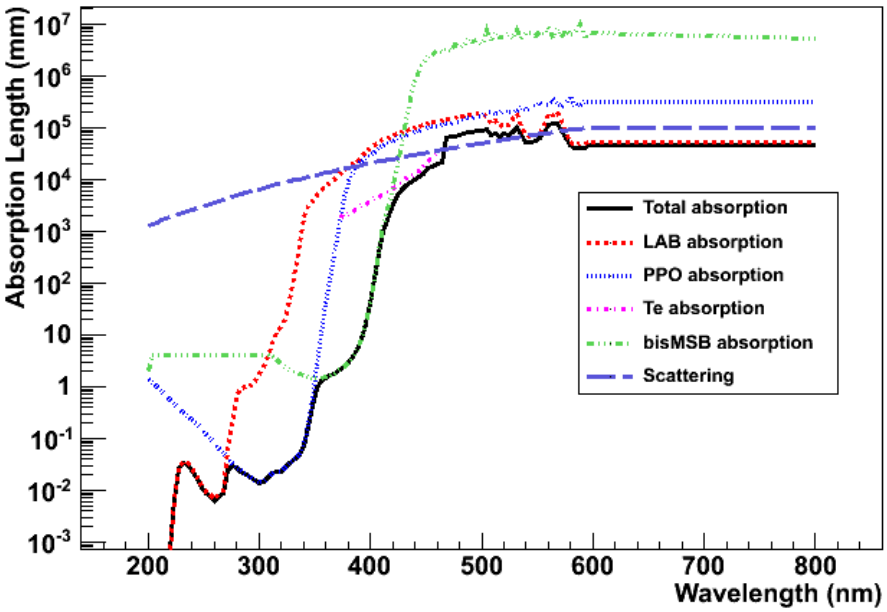

(b) Total absorption for Type B Te-loaded scintillator (at 0.1% loading) with bisMSB as a secondary WLS)

Figure 4.2: Absorption spectra for Types A and B Te-loaded scintillator with bisMSB as a secondary wavelength shifter. The absorption from the LAB is shown in red, PPO in blue, the tellurium in purple and the bisMSB in light blue. The total absorption is shown in black and the total scattering in pale blue.

Loading (%)	Nhits per MeV		
	Nd	Te+bisMSB (A)	Te+bisMSB (B)
0.1	393	468	358
0.3	274	378	234
0.5	215	302	178
1	146	179	119

Table 4.3: Nhits per MeV for different isotope concentrations using different loading techniques of tellurium, with and without bisMSB as a secondary wavelength shifter, and of neodymium.

Loading (%)	Position Resolution (mm)		
	Nd	Te+bisMSB (A)	Te+bisMSB (B)
0.1	100	101	99
0.3	111	128	124
0.5	127	173	140
1	149	305	175

Table 4.4: Position resolution at 3 MeV for different isotope concentrations using different loading techniques of tellurium, using bisMSB as a secondary wavelength shifter, and of neodymium.

Although the Type B loading has higher absorption and so the number of PMT hits fall off quicker with higher loadings, the lower scattering means that the fitter still sees a good reconstructed position whereas the position resolution of the Type A loading becomes noticeably worse at higher loadings.

4.2.2 Different wavelength shifters

This initial study considered only bisMSB as a secondary wavelength shifter. However other wavelength shifters (shortened to WLS) are available with different absorption and emission spectra. The simulation was then performed with two of them, BBOT and perylene, in the place of the bisMSB, alongside the Type B form of Te-loading.

The bisMSB, BBOT and perylene are all used for the same purpose, to absorb light at the low wavelengths and to re-emit at higher wavelengths above the absorption brought by the tellurium loading. Figure 4.4 shows the absorption

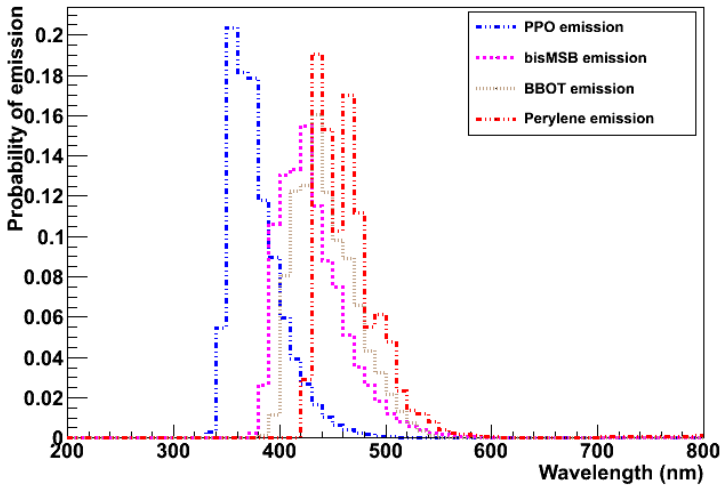

Figure 4.3: The emission spectrum of the wavelength shifters PPO (blue), bisMSB (purple), BBOT (brown) and perylene (Red).

Wavelength Shifter	Re-emission time (ns)	Re-emission probability
bisMSB	1.4	0.96
BBOT	1.4	0.9
perylene	6.4	0.9

Table 4.5: Re-emission time and probability for different wavelength shifters.

spectra of tellurium loaded scintillator with a) BBOT and b) perylene. It should be noted that while the BBOT is strongly absorbing up to 440 nm, the perylene absorbs up to 480nm, covering almost the whole region of absorption of the tellurium. Figure 4.3 shows the emission spectra of these wavelengths, compared to the PPO emission spectrum seen for unloaded scintillator, while Table 4.5 shows the probability of re-emission and delay time of re-emitted light for each wavelength shifter. Although the perylene has a slower emission time than the others which could affect the reconstruction, it emits at higher wavelengths above the absorption than the other wavelength shifters.

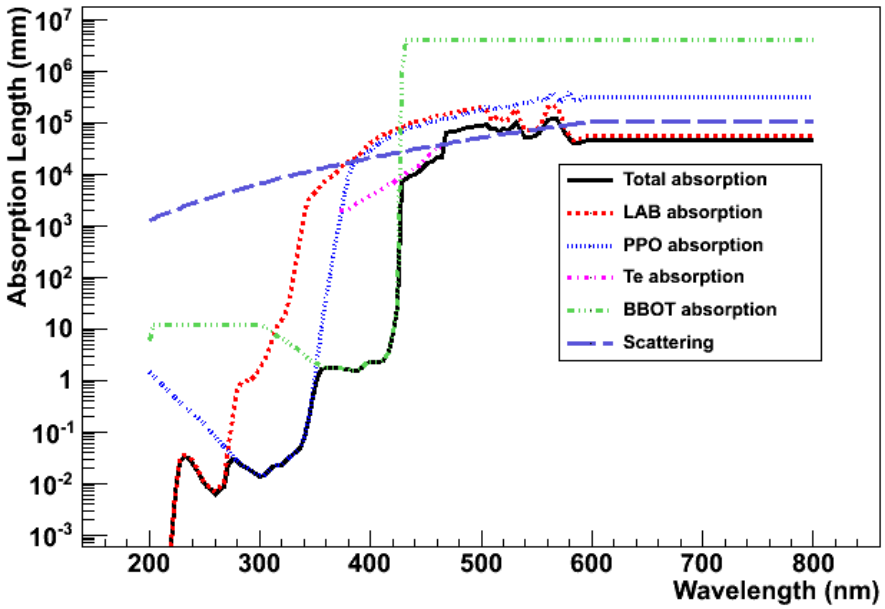

(a) Total absorption for Type B Te-loaded scintillator (at 0.1% loading) with BBOT as a secondary WLS)

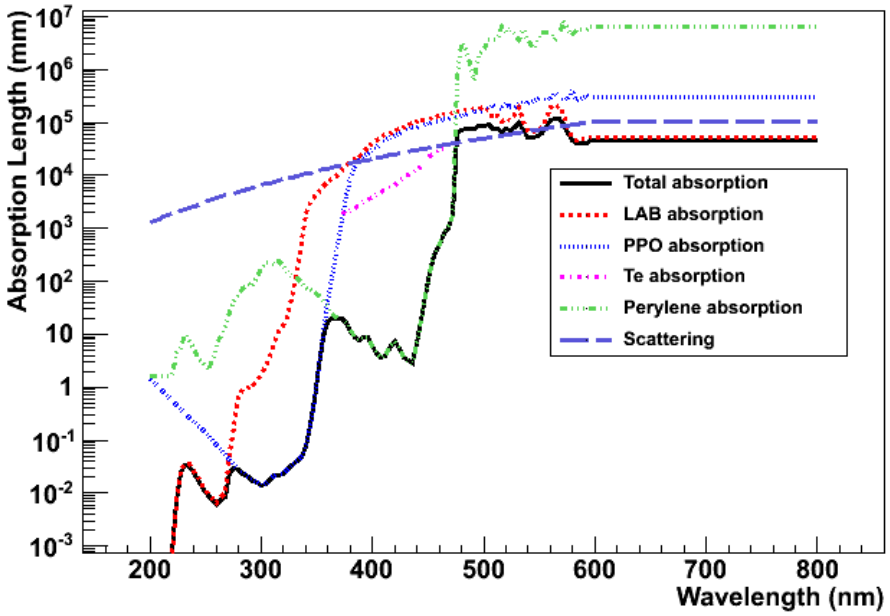

(b) Total absorption for Type B Te-loaded scintillator (at 0.1% loading) with perylene as a secondary WLS

Figure 4.4: Absorption spectra for Te-loaded scintillator with a) BBOT and b) perylene. The absorption from the LAB is shown in red, PPO in blue, the tellurium in purple and the secondary WLS in light blue. The total absorption is shown in black and the total scattering in pale blue.

Tables 4.6 and 4.7 show the Nhits per MeV and position resolution of each of these wavelength shifters across a range of loadings. It can be seen that the BBOT is an improvement on the bisMSB, in terms of both a larger number of hits and an improved resolution, however it doesn't improve things enough that percentage level loadings can be achieved because the light level still drops too quickly.

The perylene is a more promising development, maintaining over 200 PMT hits per MeV, even at the level of 1 % loading, as it shifts the wavelength of photons to above the tellurium absorption and so increased loading doesn't significantly increase the amount of absorption present. However the longer re-emission time from the perylene means that the position resolution isn't as good as for bisMSB and BBOT. At 3 MeV, a position resolution of around 19 to 20 cm is found. While this is worse than the bisMSB and BBOT, it is less than the gamma attenuation length of 26 cm and so does meet the requirements set for the position resolution. It should also be noted that this resolution does not get noticeably worse as the loading increases.

Loading (%)	Nhits per MeV		
	Te+bisMSB (B)	Te+BBOT (B)	Te+perylene (B)
0.1	358	357	322
0.3	234	242	304
0.5	178	188	292
1	119	127	269

Table 4.6: Nhits per MeV for different isotope concentrations using wavelength shifters bisMSB, BBOT and perylene alongside the Type B tellurium loading.

Loading (%)	Position Resolution (mm)		
	Te+bisMSB (B)	Te+BBOT (B)	Te+perylene (B)
0.1	99	94	191
0.3	124	111	194
0.5	140	124	197
1	175	154	195

Table 4.7: Position resolution at 3 MeV for different isotope concentrations using different wavelength shifters bisMSB, BBOT and perylene alongside the Type B tellurium loading.

4.3 Conclusion

The new scintillator Monte-Carlo provides the opportunity to investigate the performance of new scintillator mixtures. The study into the optimum level of PPO loading provides a good test of this new scintillator model and also a confirmation of the experimentally chosen scintillator mixture.

Studies into different forms of tellurium loading suggest that loading at the 0.3% level as initially planned should be possible with the currently existing techniques. Further tests with different wavelength shifters look promising for the potential to reach towards higher, percentage level, loadings of tellurium as planned for future stages of SNO+ but work is still currently ongoing as various different loading techniques and purifications are still undergoing development.

Chapter 5

Reconstruction in the scintillator phase

It is important to be able to accurately reconstruct the position, time and energy of events if the signal and backgrounds observed with the SNO+ detector are to be understood. Several fitters have been developed to deal with this, in both the water and scintillator phases of running, with loaded and unloaded scintillator. The work described on these fitters builds on previous work from SNO in the case of the quadFitter[74] and on more recent work by P.G.Jones in the case of the likelihood fitter[75].

This chapter briefly outlines how the fitters are implemented in the software and what is required of these fitters by the physics aims of SNO+. It then describes in detail two fitters: the quadFitter, which aims to return a quick but robust fit to the event vertex, and a likelihood fitter, which provides a more accurate fit.

5.1 Reconstruction in SNO+

5.1.1 Definitions

This chapter refers to the resolution and mean radial bias and uses these to characterise and compare the fitters. These properties are defined below:

Resolution is defined by compiling histograms of the differences between the fitted and true positions in the three co-ordinates x, y and z. A Gaussian profile is then fit to each of these to get the RMS deviation in each direction σ_x, σ_y and σ_z. To get the total resolution, these are then added in quadrature:

$$\text{Resolution} = \sqrt{\sigma_x^2 + \sigma_y^2 + \sigma_z^2} \tag{5.1}$$

Radial bias is defined as the difference between the fitted and true position, projected along the radial component of the true position:

$$\text{Radial\_Bias} = (\underline{\text{fitPos}} - \underline{\text{truePos}}) \cdot \widehat{\underline{\text{truePos}}} \tag{5.2}$$

To get the mean radial radial bias, a histogram of the radial biases is compiled, to which a Gaussian profile is fit. The mean of this Gaussian is taken to be the mean radial bias.

Radial bias is a useful measure due to the approximate spherical symmetry of the SNO+ detector. Ignoring a few elements such as ropes, the detector geometry should be identical across the x-y plane. This symmetry is broken in the z direction by the AV neck but this is a relatively small effect compared to the bias in the radial direction from the centre.

Other useful measures include that of the execution time of the fitter, the time it takes to fit an event, and the 'fit fraction', the fraction of successfully fit events. The tails of the fit are characterised by examining how well the reconstructed

position is described by the Gaussian distribution and looking for any outlying points.

5.1.2 Fitter structure

Before discussing the fitters themselves, it would be useful to briefly outline the structure of the fitters used in RAT, as developed for SNO+ by P.G.Jones, A.Mastbaum and S.Biller[76]. In order to allow fitters to be more easily maintained and to prevent duplication of effort in developing multiple fitters, a modular form is used whose parts can be interchanged. This enables, for example, the same fitter method to be used with different seeds or different PDFs. This is of particular use given the multiple phases of running involved in SNO+ as it means the same basic fitter can be used with different scintillator materials when accompanied by, for example, different PDFs.

The fitter structure consists of:

Method - Contains the main fitter algorithm

Optimiser - Runs the fitter method for a proposed fit vertex and iterates until the vertex converges on a solution in order to maximise or minimise a certain value

PDF - Returns a probability of a PMT hit given a proposed vertex

Seed - Provides the fitter with an initial proposed vertex

PMT selector - Chooses a sub-set of PMTs to be used in the fit

The method is required for all fitters but the other parts of the structure are optional. For example, the quadFitter uses only a method, whereas the likelihood fitter uses a method, optimiser, PDF and seed.

5.1.3 Requirements for position fitter

When determining whether or not the fitters are sufficient for the purposes of SNO+, several things must be considered: principally, the effect of the achieved position resolution on the energy resolution and on the reconstruction of external backgrounds.

One factor is the effect of the position resolution on the energy resolution. Since the energy is reconstructed based on the number of PMT hits produced by an event, which will have a radial dependence, a poorly reconstructed position can result in a poor fit to the energy of the event. However, within the fiducial volume, away from the edge of the detector, the change in number of hits is gradual enough that this isn't a large effect. For 0.3 % loading of tellurium, to affect the energy resolution by 5 % requires a position resolution of worse than 35 cm at 2.5 MeV. For unloaded scintillator, this effect is even more slight, requiring a resolution of worse than 150 cm. Thus, this isn't a limiting factor on the required resolution.

One potential problem is that of external backgrounds, from outside the scintillator volume, which can reconstruct within the scintillator. These tend to fall off exponentially as one moves in from the edge of the acrylic vessel (AV). This leads to the choice of fiducial volume as a sphere which cuts off at a radius short of the AV. The Compton scattering length of 2.6 MeV gammas in the scintillator is 26 cm so this requires a low radial bias and a resolution of under 26 cm such that as few as possible of these events will reconstruct within this fiducial volume. The identification of these backgrounds and choice of fiducial volume is discussed in more detail in Chapter 6.

Another requirement is that the tails of the fit are understood, in this case by seeing how well they are described by a Gaussian fit and minimising the amount of outlying points. The cause of any remaining outlying points should be understood.

5.2 quadFitter

The quadFitter is based on an idea developed early on in SNO[74]. This was less successful than other likelihood-based fitters due to the directional nature of Cherenkov light, but its results should be helped greatly by the isotropy of the scintillation light, as well as the greater number of hit PMTs. Thus, this idea was re-adapted for use in scintillator with the aim of providing a fitter that is quick to run as well as relatively independent of and easy to adapt for different materials. This could then be used on its own or as a seed for more sophisticated fitters.

The idea behind the quadFitter involves taking 4 PMT hits and calculating an event vertex based on their positions and times, assuming straight line paths for photons travelling between the event vertex and each PMT. This 'quad point' will be a rather poor estimate of the event vertex, due to the relatively long emission time from scintillation, meaning that not all photons begin at the same time, as well as a large probability that the photon hasn't travelled directly from the initial event vertex but instead will have been scattered or re-emitted after absorption. However, if this calculation is repeated many times for random combinations of PMTs, a 'quad cloud' of these points can be built up. Combining these quad points, a good fit to the vertex time and position can be calculated, while remaining unaffected by any individual outlying point.

5.2.1 Calculation

Assume an event occurs at a position $\underline{r_0}$ and time τ. This event creates photons which travel in straight line paths directly to the PMTs, causing hits at 4 PMTs at positions $\underline{r_1}$,$\underline{r_2}$,$\underline{r_3}$,$\underline{r_4}$ and times t_1,t_2,t_3,t_4 respectively. From these four hits, an estimate for the initial vertex can be directly calculated.

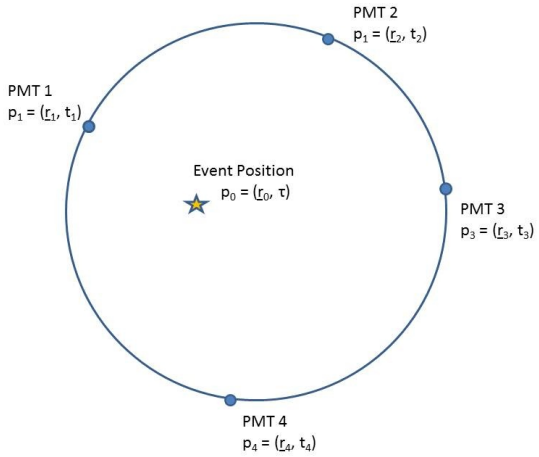

Assuming the light to have a straight line of flight through a single medium,

$$(\underline{r_i} - \underline{r_0})^2 = v^2 \times (t_i - \tau)^2$$
$$|p_i - p_0|^2 = 0$$
$$p_i^2 - 2p_i.p_0 + p_0^2 = 0$$

where $p_0 = (\underline{r_0}, \tau)$ is the 4-vector of the event vertex, $p_i = (\underline{r_i}, t_i)$ is the postion and time of a PMT i and v is the effective speed of light within the medium. The value of this is discussed below in section 5.2.3.

Considering two hit PMTs from the same event,

$$p_2^2 - 2p_2.p_0 + p_0^2 = 0$$
$$p_1^2 - 2p_1.p_0 + p_0^2 = 0$$
$$(p_2 - p_1).p_0 = \tfrac{1}{2}(p_2^2 - p_1^2)$$

Expanding this to 4 PMTs gives:

$$M.\underline{r_0} - v^2\tau\underline{N} = \underline{K}$$

where $M = \begin{pmatrix} x_2 - x_1 & y_2 - y_1 & z_2 - z_1 \\ x_3 - x_1 & y_3 - y_1 & z_3 - z_1 \\ x_4 - x_1 & y_4 - y_1 & z_4 - z_1 \end{pmatrix}$, $\underline{N} = \begin{pmatrix} t_2 - t_1 \\ t_3 - t_1 \\ t_4 - t_1 \end{pmatrix}$, $\underline{K} = \frac{1}{2}\begin{pmatrix} p_2^2 - p_1^2 \\ p_3^2 - p_1^2 \\ p_4^2 - p_1^2 \end{pmatrix}$

A possible solution to this is $\underline{r_0} = \underline{G} + v\tau\underline{H}$, where $\underline{G} = M^{-1}\underline{K}$ and $\underline{H} = M^{-1}\underline{N}$.

It can then be substituted back to solve for τ.

$$(\underline{r_1} - \underline{r_0})^2 = v^2(t_1 - t_0)^2$$
$$(\underline{r_1} - \underline{G} - v\tau\underline{H})^2 = v^2(t_1 - \tau)^2$$
$$(\underline{r_1} - \underline{G})^2 + v^2\tau^2H^2 - 2v\tau(\underline{r_1} - \underline{G}).\underline{H} = v^2t_1^2 - 2v^2\tau t_1 + v^2\tau^2$$
$$(H^2 - 1)v^2\tau^2 - 2v^2((\underline{r_1} - \underline{G}).\underline{H} - t_1)\tau + (\underline{r_1} - \underline{G})^2 - v^2t_1^2 = 0$$

This quadratic can be solved for the event time, τ. At this point, any non-real or unphysical values, such as imaginary times or times outside the event window, are rejected. τ can then be used to get the event position, $\underline{r_0}$.

5.2.2 Code logic

In the initialisation, the code reads input parameters from a database file that sets the values of a cutoff on the number of PMT hits and the effective speed, as well as the number of quad-points that will be calculated. The effective speed will be dependent on the scintillator material used and so these parameters are given in the database file separately for several different materials. The code will check to see if the parameters exist for the current scintillator material and use them if found. If separate parameters don't exist for this material, it will use those of unloaded scintillator.

To begin with, the code checks the number of PMT hits against a low nhits cutoff. This is to remove events that wouldn't be reliably fit due to low statistics. This is typically done for events with less than 10 hits.

Next, the code draws four different PMTs at random before doing the calculation described in section 5.2.1, producing a quad point ($\underline{r_0}$, τ). Some checks are then performed to ensure the result is sensible: checking that τ is real and that it occurs before the four PMT times, i.e. that the event occurs before the photons have reached the PMTs. After this, it checks that the event position is somewhere within the detector before adding the quad point to a results table.

This process is repeated until a specified number of quad points have been

generated. The number of required quad points depends on the required run time and accuracy and is discussed further in section 5.2.4. If it takes too many attempts to generate enough quad points, something must be wrong with the fit and so it stops, marking the fit as invalid. The upper limit on the number of attempts is set as a parameter by the user.

These results are filled into four tables, one for each position co-ordinate and the time co-ordinate, which are then sorted and the median value of each is taken. These are returned as the fitted event vertex.

5.2.3 Choice of effective velocity

Modelling the speed of the photons as they travel through the detector entails complications as the group velocity of the photons in the medium will depend on the refractive index of the material and, therefore, also on the wavelength of the photon. Since there is no way of measuring the wavelength of individual photons as they reach the PMTs, an overall 'effective' speed that is averaged over the detected wavelengths is used. In addition to this, the wavelength-dependent optical properties of the medium, such as scattering and absorption, will act to slow photons or deviate them from the direct paths. There is also the possibility of re-emission which can change the wavelength of a photon, and so its speed, as it travels. These issues are often difficult to separate and, so, an empirical approach was taken in which the chosen effective speed is that which minimises the radial bias of the fitted events.

Figure 5.1 shows trial values of the effective speed plotted against the radial bias they produce. To determine the best value, this is fit linearly and the value which causes zero radial bias is calculated.

Figure 5.2 shows the effective speeds generated for various materials: unloaded scintillator as well as 0.1, 0.3 and 0.5% loadings of the double beta decays isotopes

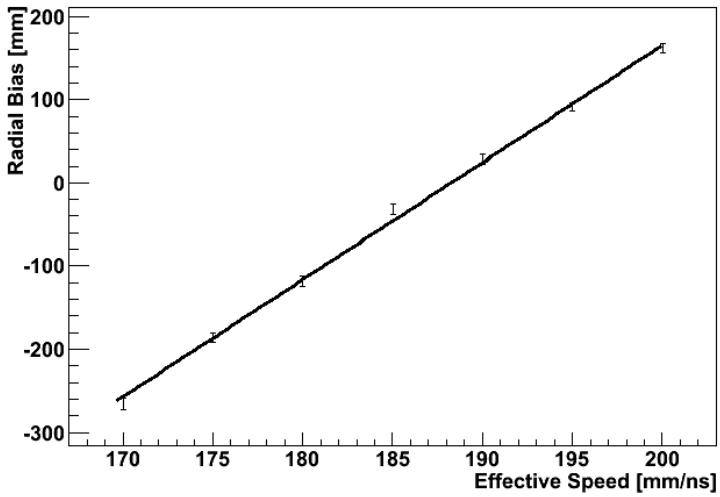

Figure 5.1: Radial bias plotted against the effective speed and fit using a straight line. The crossing point at which the radial bias is zero is taken as the position of best fit. This example is for unloaded scintillator, using 3 MeV electrons.

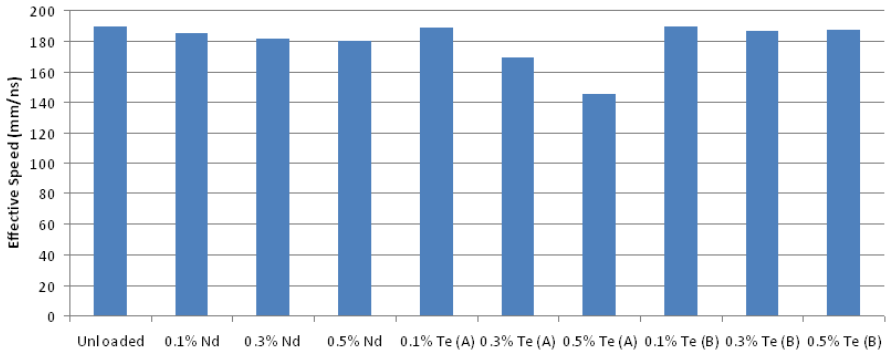

Figure 5.2: The effective speed found that minimises the radial bias of the quadFitter (for events at 3 MeV filling a fiducial volume of 5.5m) plotted for a number of materials including unloaded scintillator as well as various loadings of Te and Nd loaded scintillators.

Nd and Te. The Te-loaded scintillator is considered for two forms, defined in Chapter 4, as Type A and Type B. Comparing these to the group velocity of the scintillator, which is 188 mm/ns at 400 nm and 190 mm/ns at 425 nm, it is expected that the effective speeds should be slower than this due to the effect of scattering and re-emission acting to make photons take longer to reach the PMTs. For the unloaded scintillator, the speed is calculated to be 188.8nm, close to that expected from the group velocity. For the neodymium, which brings absorption peaks in the higher wavelength region, as the amount of isotope loading increases,

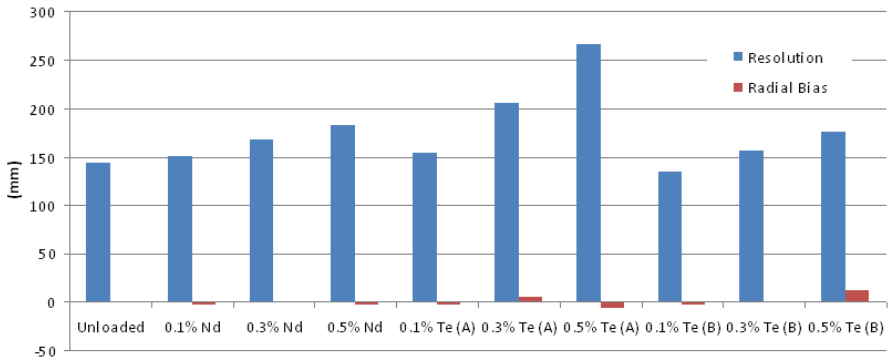

Figure 5.3: The resolution (blue) and mean radial bias (red) plotted for each material using the effective speed shown in Figure 5.2. This is calculated for 1000 3 MeV electron events filling a volume of 5.5 m.

the effective speed slows slightly to 180 mm/ns at 0.5% loading. For Type A tellurium, which has additional absorption as well as a significant increase in the scattering, the effective speed decreases significantly with increased loading, as the scattering acts to 'slow' the photons and increase their time of flight before reaching the PMTs. The Type B tellurium loaded scintillator has no additional scattering but does have a larger absorption than Type A and, as the loading level increases, this causes it to slow slightly to 187 mm/ns.

Figure 5.3 shows the resolution and radial bias of each material when reconstructing 3 MeV electrons within a fiducial radius of 5.5 m. As can be seen, the speed is chosen such that the magnitude of the radial bias has been minimised. In all cases, the mean radial bias at 3 MeV is less than 1 cm. The resolution and bias will be discussed further in section 5.2.6. It should be noted that, although the overall radial bias within 5.5 m has been tuned to zero, the radial bias may still be non-zero at a given radius and so must still be characterised.

5.2.4 Choice of the number of quad points

In choosing the numbers of quad points, a balance needs to be found between the accuracy that can be gained by generating additional points and the increase in CPU time needed to generate these extra points. Since one of the advantages of

the quadFitter is that is quick to run, the time it takes to fit events should be kept low while still returning accurately fitted positions.

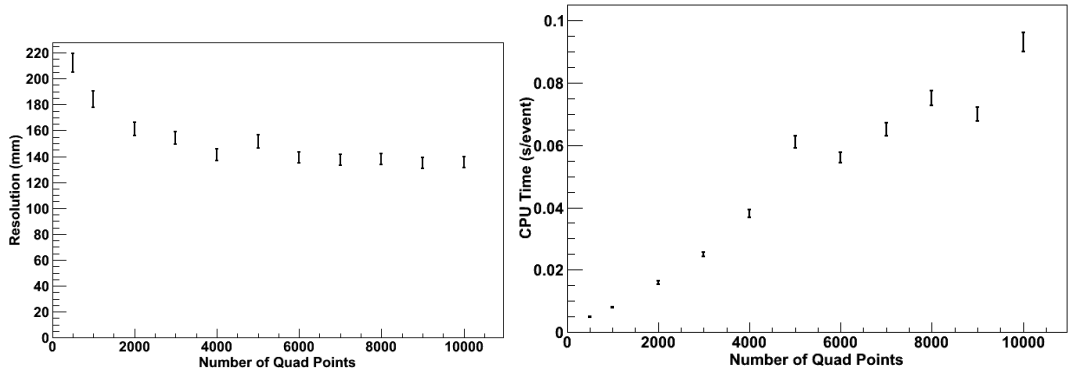

(a) Number of quad points vs resolution (b) Number of quad points vs execution time

Figure 5.4: The resolution and execution time of the quadFitter for different number of points in the quad cloud.

Figure 5.4 shows the the resolution and execution time of the quadFitter for different total number of points in the quad cloud. These were generated for 1000 3 MeV electron events spread isotropically throughout the detector, using unloaded scintillator, within a volume of 5.5 m. This was done so as to avoid events near the edge of the acrylic vessel, where significant optical effects occur due to the larger angles with respect to the acrylic surface and where the straight line assumptions made in the calculation of the fit begin to break down. It can be seen that as the total number of points increases, the resolution improves but the execution time also increases. However, above 5000 quad points, the resolution stops showing any significant improvement. Hence, 4000 was chosen as the default value as a reasonable compromise between speed and accuracy. The user is also given the option to change the value used during initialisation of the fitter.

5.2.5 Approximations

One major assumption made was that of the photon travelling on a straight line path from the scintillator all the way through to the PMTs. In reality, it will pass

through material boundaries from the scintillator to the acrylic vessel and from the acrylic vessel to the water shielding and, in each case, it will undergo refraction. To take account of the refraction of the photon, the method was modified to use a calculation of the true optical path and time of flight from the scintillator, through the acrylic vessel to the PMTs[77]. This took account of the different refractive indices and group velocities of each material, finding the path via a trial and error method of tracing rays from the start position and refracting across material boundaries to get the final position at the PMTs. It then adjusted the initial direction and repeated until the calculated final position was acceptably close to the desired final position. Unfortunately, this could be slow, at times requiring multiple iterations. Since one of the main goals of the quadFitter is to provide a quick result, and the benefits of including this correction were found to be minimal, it was decided to bypass this correction and stick with straight line paths.

Other assumptions include that of a single effective speed, independent of the initial position and energy of the event, and of a single photon causing each PMT hit. In actuality, a PMT can be hit by multiple photons from the same event. This can be identified by the charge deposited in the PMT, although not reliably, and the timing information of the two photons can't be separated. This is particularly common for higher energy events and those near the edge of the detector which would have a larger number of photons per PMT in a given solid angle than usual. Thus, the best effective speed is likely to change, especially towards the edge of the detector. The effect of these assumptions will be discussed further in section 5.2.6 on the energy and radial dependence of the fitter.

5.2.6 Results

In characterising the quadFitter, the energy and radial dependence of the resolution and radial bias were investigated, first for unloaded scintillator and then for loaded scintillators, assuming the optical properties of the double beta decay isotopes neodymium and tellurium. The tails of the fit are also discussed.

Energy dependence

The dependence of the quadFitter performance on the deposited energy of an event was investigated by generating 1000 electron events spread isotropically through the scintillator volume, across the energy range 0.1 to 10 MeV, divided into 11 energy bins. The resolution and radial bias were then calculated for each bin for events within a fiducial volume of 5.5 m and are shown in Figure 5.5.

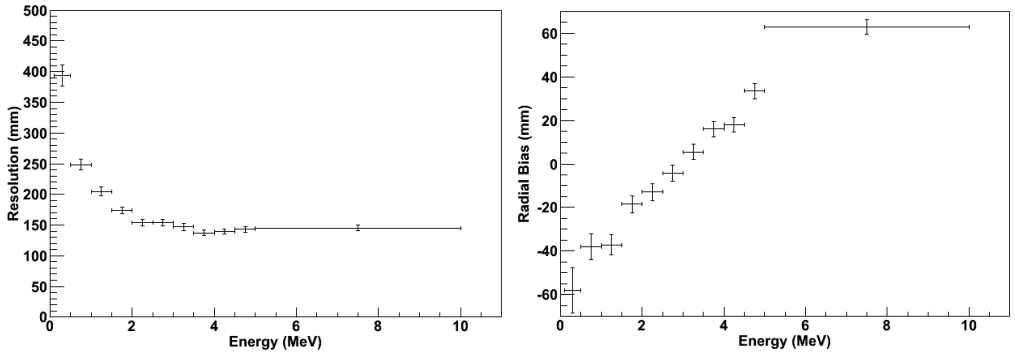

(a) quadFitter resolution vs energy (b) quadFitter radial bias vs energy

Figure 5.5: The resolution and radial bias of the quadFitter for events generated with 0.1 to 10 MeV electrons, spread isotropically throughout the detector with a fiducial volume of 5.5 m, using unloaded scintillator.

The resolution of the quadFitter inproves from about 25 cm at 0.5 MeV to 15 cm at 2 MeV. Above 2 MeV, it remains roughly constant with energy around 14 cm.

The radial bias increases with energy. At 3 MeV, the bias is close to zero. This is expected since, as discussed in 5.2.3, the effective speed used in the detector is tuned using simulations of 3 MeV electrons, being in the region of interest for

a double beta decay search in SNO+. As the energy increases, the radial bias increases, pushing events out towards the edge of the detector. This is most likely due to multiple hits on the same PMTs. At higher energies, the number of multiple hits in nearby PMTs will increase. Since the quadFitter doesn't take account of this effect, a bias is introduced. Despite this, the radial bias remains low, less than 4 cm even in the worst cases of very low or high energy.

The execution time stays almost constant at around 0.04 seconds per event, which is as expected since the same number of quad points are calculated each time irrespective of the number of hits.

Radial dependence

Similarly, the radial dependence of the quadFitter was investigated by generating 1000 3 MeV electron events within 8 radial shells through the scintillator. The resolution and radial bias were then calculated for each bin as shown in Figure 5.6.

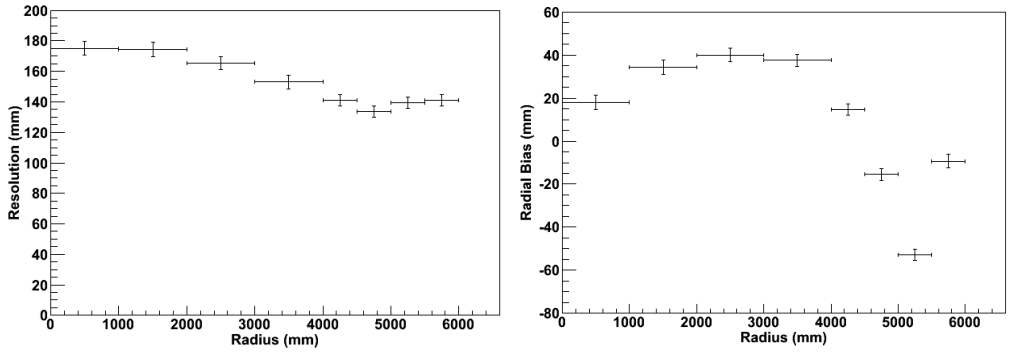

(a) quadFitter resolution vs radius (b) quadFitter radial bias vs radius

Figure 5.6: The resolution and radial bias of the quadFitter at different radii for 3 MeV electron events in unloaded scintillator.

The resolution of the quadFitter has a slight radial dependence, ranging between 18 cm at the centre of the detector and 14 cm around 4 to 5 m. The radial bias falls to zero around 4.5 m, but rises to around 5 cm near the edge of the AV. This variation can be understood by noting that the fitter has been tuned to

work for events within a fiducial volume of 5.5 m. The majority of events in this volume with occur between 4 to 5 m so it is these events show the best resolution and minimal radial bias.

Events near the centre show worse resolution and a larger radial bias, as the most suitable effective speed in this region is likely to be different to that nearer the edge. This is because a photon beginning in the centre of the detector is more likely to be absorbed and re-emitted along its path to the PMTs than the same photon beginning nearer the edge.

The resolution and radial bias become larger near the edge of the AV, between 5.5 and 6 m. This region is non-trivial to deal with as the assumption of a straight line path breaks down significantly due to the stronger effect of refraction and total internal reflection at the interface between the scintillator and the acrylic vessel, caused by more extreme angles with respect to the acrylic surface. Events in this region can also be fit using the nearAV fitter, a fitter which uses the characteristic geometric pattern of the hits caused by total internal reflection to fit the position, as developed by S.Morgan[78], P.G.Jones and K.Majumdar[79], and so would take account of these optical effects. Despite the radial dependence, the quadFitter works well across all regions; the resolution varying between 14 and 18 cm and the radial bias always being less than 5 cm in either direction.

Material dependence

The investigations into the energy and radial dependence of the quadFitter were repeated for different loading levels of the double beta decay isotopes neodymium and tellurium, using the optical properties described in Chapter 4. As discussed in Section 5.2.3, a different effective speed in the scintillator is used for each material to take account of the different amounts of absorption and scattering.

- Nd-loaded scintillator

The energy and radial dependences are plotted for 0.1, 0.3 and 0.5% Nd as

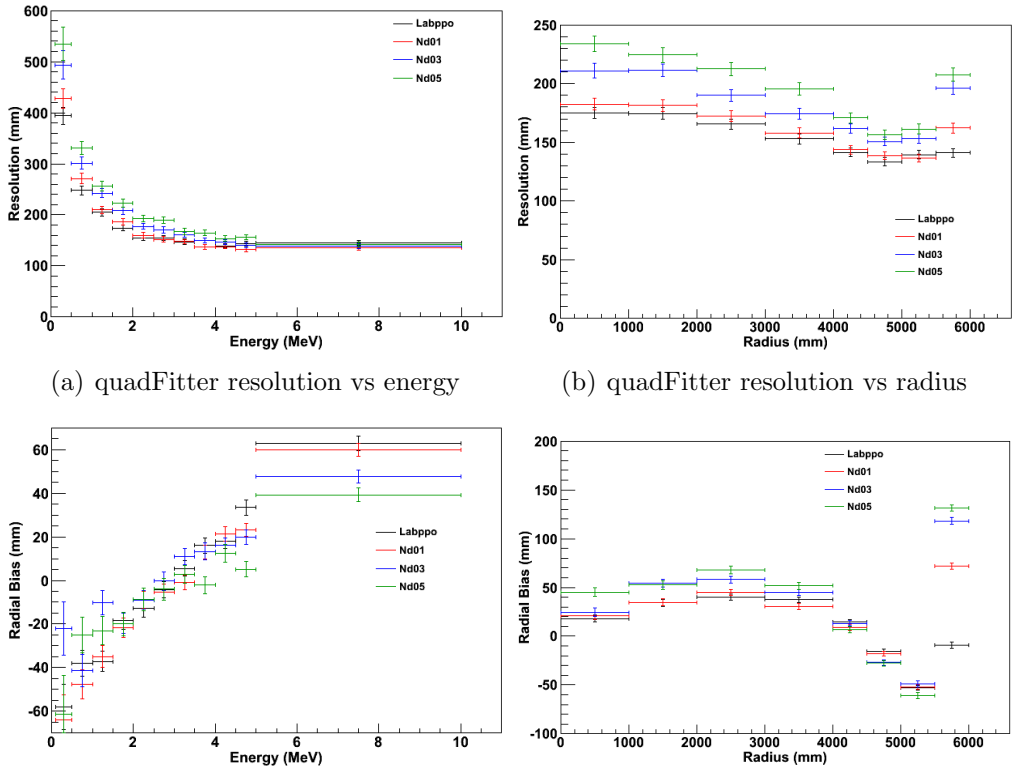

(a) quadFitter resolution vs energy

(b) quadFitter resolution vs radius

(c) quadFitter radial bias vs energy

(d) quadFitter radial bias vs radius

Figure 5.7: The resolution and radial bias of the quadFitter at different energies and radii generated by simulating electron events in a detector filled with unloaded scintillator and 0.1, 0.3 and 0.5% Nd-loaded scintillator. The energy events are simulated for events filling the detector in 11 different energy bins while the radial events are simulated at 3 MeV in 8 different radial bins.

well as unloaded scintillator on Figure 5.7. Neodymium loading brings additional absorption peaks above 400 nm, reducing the number of hits produced by an event. The results follow a similar trend to that of the unloaded scintillator for the radial bias, pushing events out towards the edge of the detector as energy increases, with the best results around 3 MeV and at 4 to 5 m. The resolution gets slightly worse as loading increases, rising from about 15 cm to 18 cm at 0.5% loading.

As the loading increases, the resolution becomes noticeably worse in the centre of the detector, 23 cm at 0.5% compared to 18 cm for the unloaded scintillator. This is due to the additional absorption having a much larger effect on the photons from the centre, which travel the farthest average distance to the PMTs, so the number of hit PMTs and the statistics availiable to the fitter drop. Within the

fiducial volume, the radial bias becomes larger as the loading increases but is limited to less than 7 cm, even at the 0.5% loading of Nd. This suggests that adding Nd into the scintillator doesn't adversely affect the performance of the quadFitter.

- Te-loaded scintillator (Type A)

Type A Te-loading brings with it some additional absorption in the 400-450 nm region as well as a significant increase in the scattering. In order to lessen these effects, it is accompanied by a secondary wavelength shifter which absorbs photons in this 400-450 nm region and re-emits them at higher wavelengths, where the amount of absorption and scattering is less significant. The energy and radial dependence for 0.1, 0.3 and 0.5% loading are shown on Figure 5.8 alongside that of the unloaded scintillator. The energy dependence and radial dependence follow similar trends as were observed for the unloaded scintillator.

As loading increases, the resolution worsens from 15 cm with unloaded scintillator to 20 cm with 0.3% loading and 28 cm at 0.5% at 3MeV. This is mainly due to the increased amount of scattering as the loading of the isotope increases, which mean that it is more likely that photons will be scattered before they reach the PMTs. This results in less direct light and so the assumption of the photon travelling in a straight line from the initial event to the PMT becomes less applicable. Since the photon is more likely to be scattered the farther it has to travel through the scintillator, the radial dependence of the resolution and radial bias becomes stronger at higher loading with radial bias as large as 12 cm for 0.3% loading and 22 cm for 0.5% as well as resolutions that are significantly worse towards the centre of the detector.

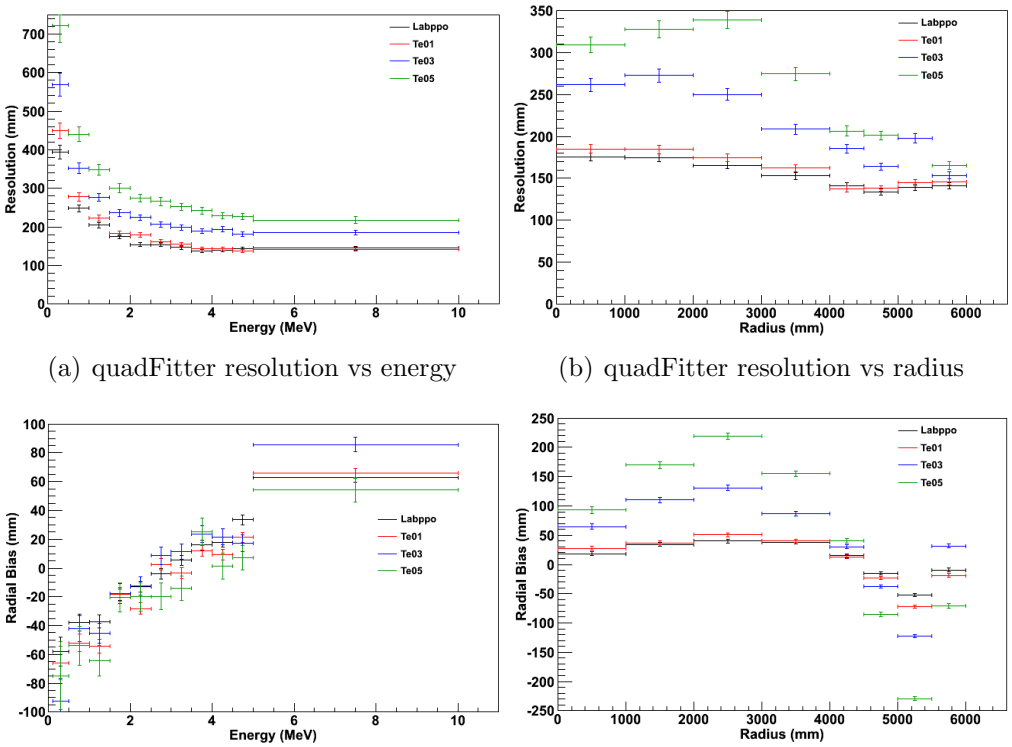

(a) quadFitter resolution vs energy

(b) quadFitter resolution vs radius

(c) quadFitter radial bias vs energy

(d) quadFitter radial bias vs radius

Figure 5.8: The resolution and radial bias of the quadFitter at different energies and radii, generated by simulating electron events for a detector filled with unloaded scintillator and 0.1, 0.3 and 0.5% Type-A Te-loaded scintillator. The energy events are simulated for events filling the detector for 11 different energy bins while the radial events are simulated at 3 MeV in 8 different radial bins.

- Te-loaded scintillator (Type B)

As just shown, large scattering on the order of a couple of metres becomes a significant problem for the position fitters and so a second formulation of the tellurium loading was developed. This has no extra scattering above the unloaded scintillator level but a significant amount of absorption in the 400-450 nm region. Again, it uses a secondary wavelength shifter to move photons up above this region of higher absorption. The energy and radial dependence for 0.1, 0.3 and 0.5% loading are shown on Figure 5.9 with that of the unloaded scintillator.

As can be seen, the energy dependence and radial dependence follow similar trends as were observed for the unloaded scintillator. The effect of loading worsens the resolution, due to the extra absorption decreasing the number of PMT hits

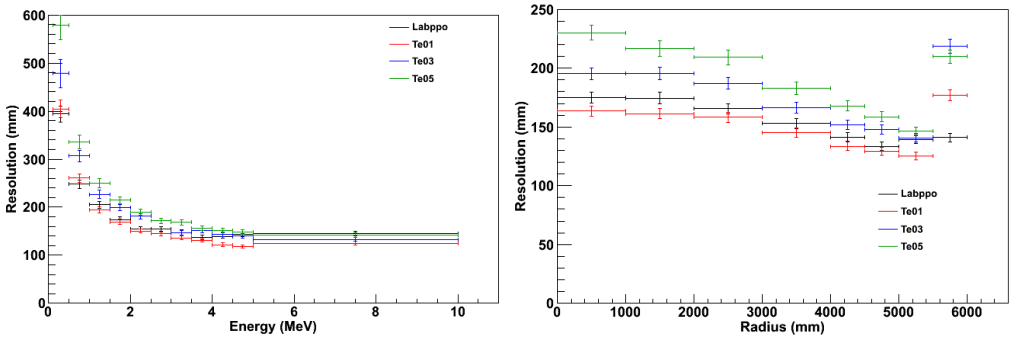

(a) quadFitter resolution vs energy

(b) quadFitter resolution vs radius

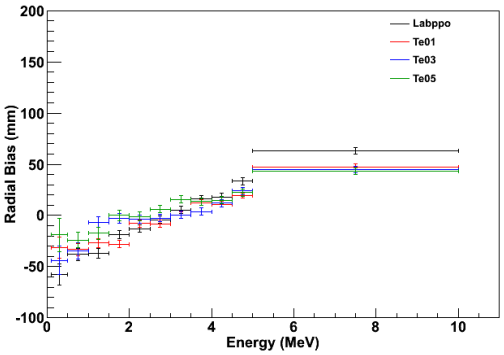

(c) quadFitter radial bias vs energy

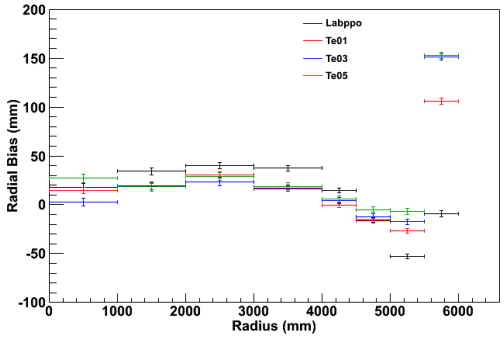

(d) quadFitter radial bias vs radius

Figure 5.9: The resolution and radial bias of the quadFitter at different energies and radii, generated by simulating electron events for a detector filled with unloaded scintillator and 0.1, 0.3 and 0.5% Type-B Te-loaded scintillator. The energy events are simulated for events filling the detector for 11 different energy bins while the radial events are simulated at 3 MeV in 8 different radial bins.

and so the fitter has less statistics to work with. Despite this, the resolution, at 3 MeV, remains better than 20 cm throughout the detector volume, even in the centre where the drop in the number of PMT hits, and so resolution, should be the worst. The resolution rises from about 15 cm to 18 cm at 0.3% loading at 3 MeV. Within the fiducial volume, the radial bias is limited to less than 5 cm.

Reconstruction tails

The tails of the fit were investigated by simulating 50,000 3 MeV electron events, in the centre of the detector and between 3 and 4 m, the results of which are plotted in Figure 5.10. In each position, the bulk of the events are described well by the Gaussian fit although around 5-10 events out of 50,000 are found to fit more

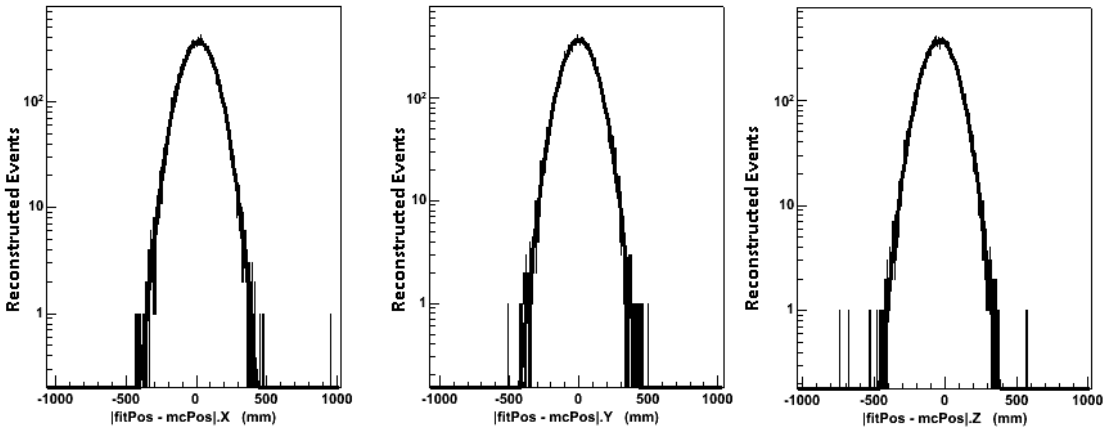

(a) Events at centre of the detector

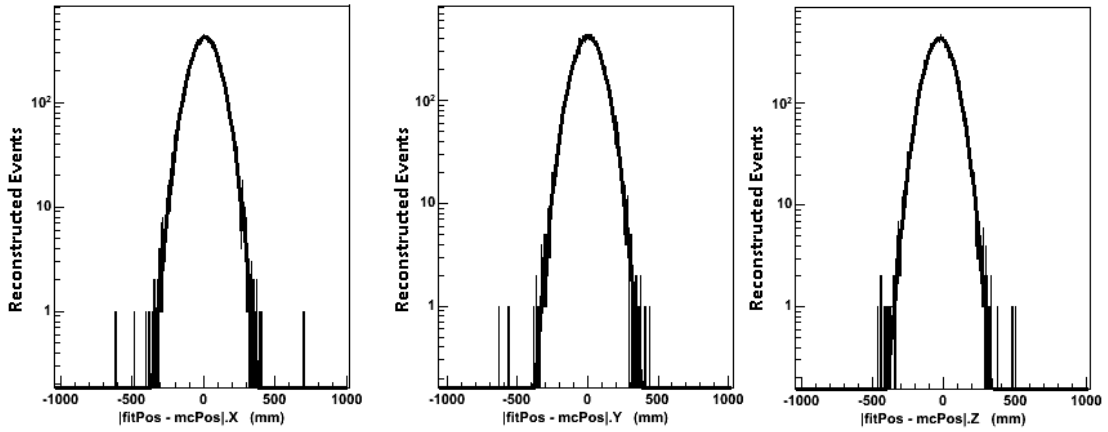

(b) Events between 3 and 4 m radius

Figure 5.10: The difference between fitted and Monte-Carlo positions for the x, y, z components and the distance between the fitted and Monte-Carlo positions generated for 50,000 events fit using the quadFitter in a) the centre of the detector and b) between 3 and 4 m radius.

than 50 cm away, however the majority of these points return a better fit from the likelihood fitter, allowing these misfits to be identified. The exception to this is a single point which returns a poor fit for both the quadFitter and likelihood fitter, which is discussed in detail in the reconstruction tails section of the likelihood fitter.

5.2.7 Potential further modifications

It is is possible that things could be improved further by using charge weighting on the PMTs or even a position or energy dependent effective speed. This might be especially useful in the limit of high scattering, in which the fitter performance begins to struggle and the radial dependence of the fitter becomes much more noticeable. However, as previously mentioned, one of the major strengths of the quadFitter is that it is quick and versatile and so the gain in resolution or bias is probably offset by the extra tuning and execution time required.

5.2.8 Summary of quadFitter properties

The quadFitter is quick, reasonably accurate and relatively invulnerable to changes in the detector geometry or materials used, meeting the requirements necessary for the resolution and bias. Although one can do better with a likelihood method, this should provide a quick and reliable method of getting a reconstructed vertex which can then be used as an accurate seed for a likelihood fitter or as a result in its own right.

Running in unloaded scintillator, the quadFitter reconstructs events, at 3 MeV, with a resolution of 15 cm and a radial bias of less than 5 cm across the entire detector volume with close to zero failed fits. The fitter is relatively quick; on the Oxford batch system, it takes 0.05 s/event to fit. For comparison, a 3 MeV electron event typically takes around 8 s/event to simulate.

With a recalcuation of the effective speed of photons within the scintillator, the quadFitter also performs well when run using scintillator loaded with double beta decay isotopes. With 0.5% loading of neodymium, it achieves 19 cm resolution and a maximum radial bias of 7 cm at 3MeV while, with 0.3% loading of tellurium (Type B), it reconstructs with a resolution of 18 cm and a radial bias of less than 5cm throughout the detector at 3 MeV.

5.3 Likelihood fitter

5.3.1 Likelihood fitter

A 1D likelihood fitter for time and position had previously been developed for use in scintillator by P.G.Jones[75]. This used a PDF of the scintillation emission times. Time residuals of PMT hits were calculated, assuming a straight line path through the different materials of the detector, and a Minuit optimiser was used to find the event position and time which maximises the log likelihood when comparing the time residuals to the scintillation time PDF:

$$logLike = \sum_{i}^{N} \log P_i \tag{5.3}$$

where P_i is the probability returned from the PDF for a PMT 'i' and a trial event vertex.

This worked but had several issues, such as being designed to treat every scintillator material the same, regardless of that material's absorption and scattering, as well as occasionally failing to converge on a fit at lower energies.

Several modifications were made to improve the fitter including:

Addition of an effective speed within the scintillator, found by minimising the radial bias

A new PDF based on the actual PMT hit times

Separate PDFs and effective speeds for different scintillator mixtures

A new optimiser based on the Powell method from Numerical Recipes

The use of the quadFitter as a seed

The reasons leading to these changes and their results are discussed further in the following sections.

5.3.2 New PDF and effective speed

A new PDF was generated consisting of time residuals based on the calibrated PMT hit times. This should give the best comparison between PDF and reconstruction since the calibrated hit times are what is observed in the real event data. The time residuals are calculated using:

$$t_{res} = t_{PMT} - t_{path} - t_{event} \tag{5.4}$$

To calculate t_{path}, a straight line path is assumed and the distances travelled in each material (scintillator, acrylic and water) are calculated based on event position and final PMT position, using a standard routine written by P.G.Jones. The time of flight is found as:

$$t_{path} = \frac{d_{scint}}{v_{scint}} + \frac{d_{av}}{v_{av}} + \frac{d_{h2o}}{v_{h2o}} \tag{5.5}$$

where d_x and v_x are the distance travelled and speed of the photon in volume x. Within the acrylic and water shielding regions, the group velocity of the peak photon wavelength as detected at the PMTs can be used[75] but this is not possible for the scintillator. The wavelength of the photons, in acrylic and water, will be unchanged as they travel while, in the scintillator, there may be absorption and re-emission, shifting photons to higher wavelengths and changing their group velocities.

As with the quadFitter, a pragmatic approach was used, with the correct effective speed in scintillator being that which minimises the radial bias of the reconstructed events. As well as compensating for the changing nature of the photon's wavelength, this should also implicitly take into account processes like scattering and re-emission which act to slow the photon on its path through the scintillator. This is found by simulating events within a volume of 5.5 m (to avoid

total internal reflection and optical effects near the acrylic vessel) and plotting the reconstructed radial bias against the effective speed, as shown in Figure 5.11. This is then fit linearly and the speed at which the radial bias is zero is read off. The results are shown in Figure 5.12 and 5.13.

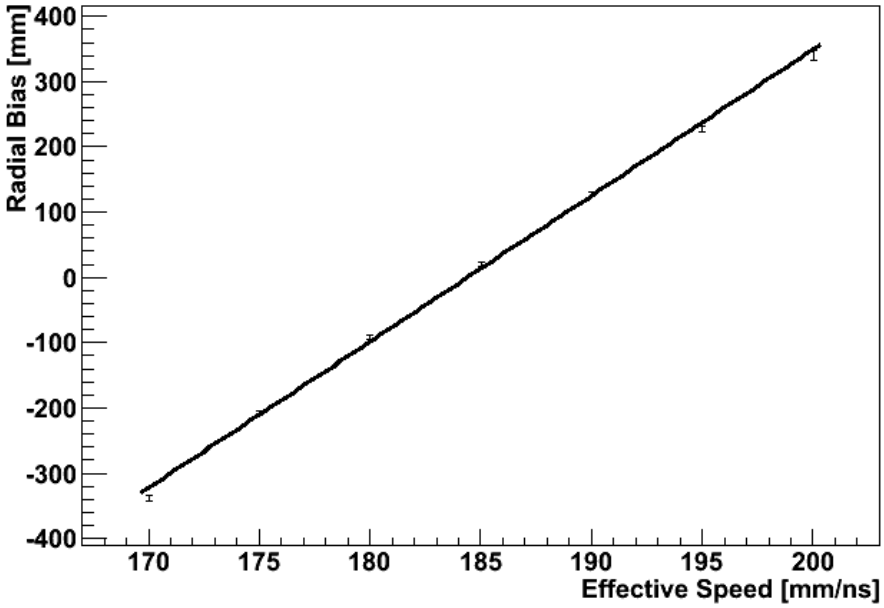

Figure 5.11: Radial bias plotted against the effective speed and fit using a straight line. The crossing point at which the radial bias is zero is taken as the position of best fit. This example is for unloaded scintillator, using 3 MeV electrons.

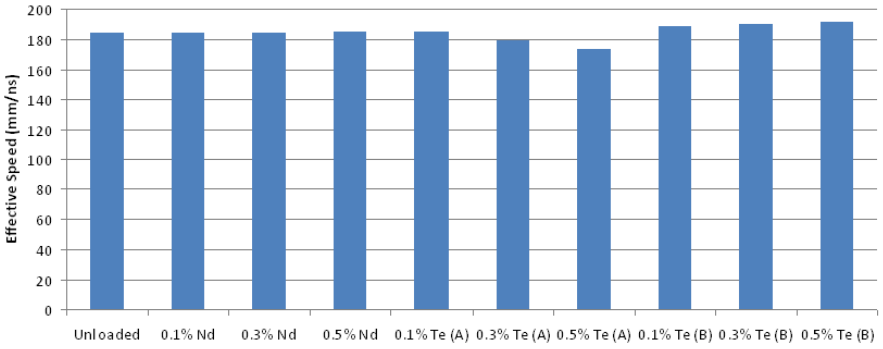

Figure 5.12: The effective speed that minimises the radial bias of the likelihood fitter (for events filling a fiducial volume of 5.5m at 3 MeV) plotted for a number of materials including unloaded scintillator as well as various loadings of Te and Nd loaded scintillators.

Figure 5.12 shows the effective speeds generated for various materials: unloaded scintillator as well as 0.1, 0.3 and 0.5% loadings of the double beta decays

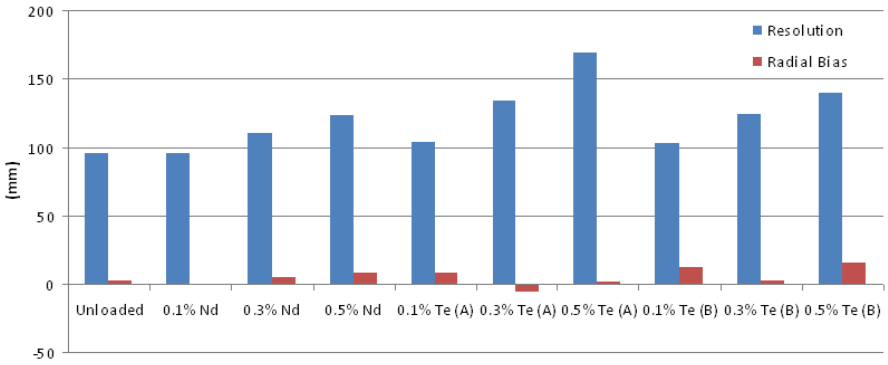

Figure 5.13: The resolution (blue) and mean radial bias (red) plotted for each material using the effective speed shown in Figure 5.12. This is calculated for 1000 3 MeV electron events filling a fiducial volume of 5.5 m.

isotopes neodymium and tellurium, again discussed in the two forms of loading, Types A and B, described in Chapter 4. For the neodymium and Type B tellurium loading, which have additional absorption in the higher wavelength region but no extra scattering, the effective speed increases slightly as the loading increases. If the absorption is increased, the scattered light, which travels farther before reaching the PMTs than the direct light, is more likely to be absorbed and so the effective speed could increase. However, for the Type A tellurium, where loading brings absorption as well as a large increase in scattering, the effective speed decreases noticeably as the scattering increases and so the photons are more likely to travel a greater distance before reaching the PMTs.

Figure 5.13 shows the resolution and radial bias of each material when reconstructing 3 MeV electrons within a fiducial radius of 5.5 m. As can be seen, the speed is chosen such the magnitude of the radial bias has been minimised. In all cases, the mean radial bias at 3 MeV is less than 1 cm. The resolution and bias will be discussed further later in the chapter.

Once the experiment is running, the effective speed used in the likelihood fitter and quadFitter will act as tunable parameters, which will be found by attempting to minimise the radial bias when fitting data from calibration sources at known positions in the detector.

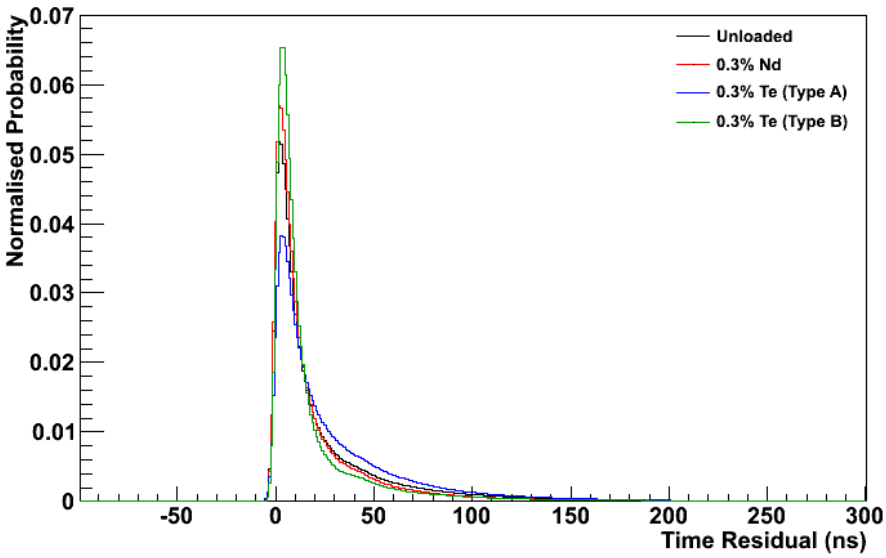

Figure 5.14: Time residual PDFs generated by simulating 20,000 3 MeV electron events evenly distributed across the detector. This is shown for unloaded scintillator and for 0.3 % loadings of neodymium and type A and B of tellurium.

Figure 5.14 shows time residual PDFs for unloaded scintillator as well as 0.3% loadings of neodymium and type A and B of tellurium loading, generated by simulating 20,000 3 MeV electron events spread evenly across the detector and using a fiducial volume cut of 5.5 m. At early and late times (less than -10 ns or greater than 220 ns), the PDF begins to suffer from low statistics, as it begins to be dominated by detector noise and the tails of the distribution. The PDF in these regions has been approximated to flat, extrapolating outwards.

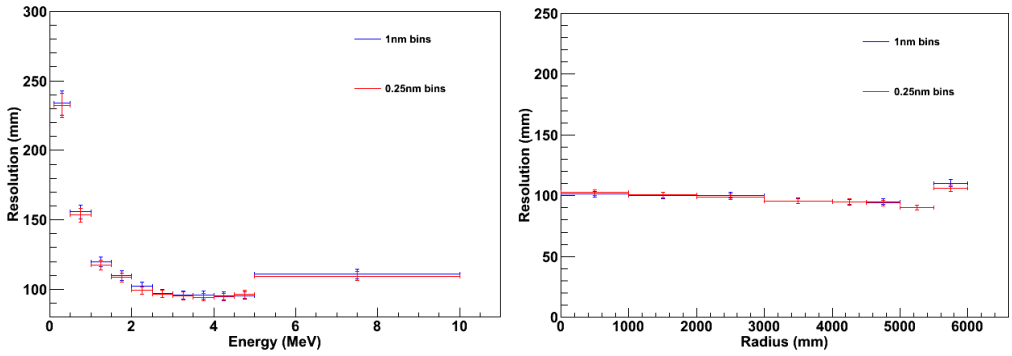

Figure 5.15: Comparison of the energy dependence (for events within a fiducial volume of 5.5 m) and radial dependence (at 3 MeV) of the resolutions achieved using PDFs with bin widths of 1 ns (blue) and 0.25 ns (red).

A bin width of 1 ns was chosen after comparisons with a PDF of bin width 0.25 ns, shown on Figure 5.15. Little difference was observed in the achieved resolution and radial bias between the two PDFs but the execution time was slower when using the smaller bins. Hence, the 1 ns width was chosen.

A PDF and effective speed was calculated for each material and these are loaded upon initialisation of the fitter. If no PDF is found for a particular material, the PDF for unloaded scintillator is used.

5.3.3 Improvements to the optimiser

On previous versions of this fitter, Minuit was used as an optimiser. That version of the fitter struggled with a significant portion of events being misfit. It was determined that these misfits were due to the Minuit optimiser getting stuck on statistical variations in the data and being unable to converge on a satisfactory fit. In order to correct this, a new optimiser was added based on the Powell method from Numerical Recipes[80]. This uses a multi-dimensional direction set minimisation. The Powell method works by minimising along each direction in turn and using this to find a new initial set of directions. It then repeats this process until the result converges.

This was tested by simulating 1000 electron events, spread isotropically through the detector at several energies from 0.1 to 5 MeV, and fitting the results using the likelihood fitter with both Powell and Minuit optimisers. The fraction of successful fits and the execution time of the fit are shown in Table 5.1. The resolution and radial bias, not shown in the table, are unaffected by the change in optimiser.

Although the Powell minimisation is slower than Minuit, it manages to successfully fit almost all the simulated events while Minuit runs into trouble, particularly at lower energies, with almost 20% of events going unfit at 0.5 MeV compared to less than 2% with the Powell minimisation.

	Fraction of valid events		CPU Execution Time (s/event)	
Energy (MeV)	Powell	Minuit	Powell	Minuit
0.1	0.900	0.498	0.043	0.036
0.5	0.993	0.833	0.096	0.062
1	0.998	0.965	0.202	0.117
3	0.998	0.967	0.386	0.226
5	0.994	0.923	0.569	0.329

Table 5.1: Fraction of successfully fit events and the execution time of the likelihood fitter for both the Powell and Minuit optimisers, found using 1000 events simulated isotropically throughout the detector at five different energies.

5.3.4 Improvements to the seed

Previously the fitter used a position seed generated by taking a centroid fit of the charge deposited in the hit PMTs. The centroid fitter takes the vector sum of the hit PMTs, weighted by the charge deposited in the PMT squared:

$$\underline{fitPos} = \frac{\sum Q^2 \cdot \underline{pmtPos}}{\sum Q^2} \tag{5.6}$$

This was extremely quick but very inaccurate. Using the quadFitter, which is still quick but significantly more accurate, as a seed, should provide a seeded position closer to the final reconstructed position and so reduce the number of misfits.

Again, this was tested by simulating 1000 electron events, spread isotropically through the detector at several energies from 0.1 to 5 MeV, and fitting the results using the likelihood fitter with seeds from both the quadFitter and centroid fitter. The fraction of successful fits and the execution time of the fit are shown in Table 5.2. The resultant resolution and radial bias, not shown in the table, are unaffected by the change in seed.

The quadFitter seed is slightly slower than the centroid seed but manages to successfully fit more of the events at low energies while the fitter using the centroid seed fails for about a third of events at 0.1 MeV, compared to 10% with the quadFitter seed, and is a few percent worse at 0.5 MeV. The likelihood fit

	Fraction of valid events		CPU Execution Time (s/event)	
Energy (MeV)	Quad	Centroid	Quad	Centroid
0.1	0.905	0.709	0.044	0.024
0.5	0.993	0.982	0.112	0.103
1	1.000	0.998	0.175	0.184
3	0.992	0.992	0.461	0.430
5	0.991	0.991	0.500	0.456

Table 5.2: Fraction of successfully fit events and the execution time of the likelihood fitter when using both quadFitter and centroid fitter as seeds, found by simulating 1000 events spread evenly throughout the detector at five different energies.

itself is quicker when using the better seed of the quadFitter but overall becomes a little slower when the time taken to generate the quadFitter itself is taken into account. However this is only a slight change in the overall execution time of the fitter.

5.3.5 Results

To characterise the performance of the likelihood fitter, the energy and radial dependence of the resolution and radial bias were investigated for unloaded scintillator as well as scintillator loaded with neodymium and tellurium. The tails of the fit were also investigated.

Energy Dependence

The energy dependence of the likelihood fitter was investigated by generating 1000 electron events spread evenly through the scintillator volume in each of 11 energy bins, covering the range 0.1 to 10 MeV. The resolution and radial bias were then calculated for each bin for events within a fiducial volume of 5.5 m. The results are shown in Figure 5.16. The resolution of the fitter increases from about 16 cm at 0.5 MeV to 11 cm above 2 MeV. The radial bias increases with energy. At 3 MeV, the bias is close to zero, since the effective speed used in the fitter is tuned using simulations of 3 MeV electron, being in the region of interest for a double

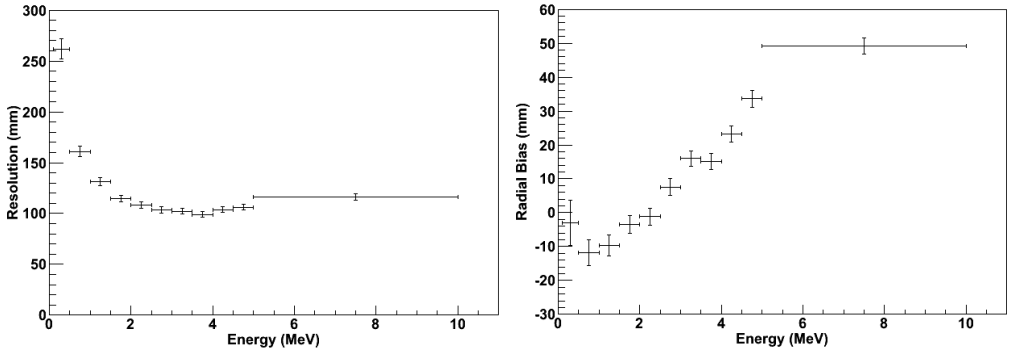

(a) Likelihood fitter resolution vs energy (b) Likelihood fitter radial bias vs energy

Figure 5.16: The resolution and radial bias of the likelihood fitter for electron events generated in unloaded scintillator at 0.1 to 10 MeV, spread evenly through the detector with a fiducial volume of 5.5 m.

beta decay search in SNO+. As the energy increases, the radial bias increases, pushing events out towards the edge of the detector, although it remains less than 3 cm across the range 0 to 5 MeV.

Similar to the quadFitter, the improved resolution is caused by the additional statistics given by the increase in PMT hits at higher energies. Higher energies also result in multiple photons being incident on the same PMT. This results in a bias since a PMT hit by multiple photons will be more likely to record an early hit time, since the PMT will only record the earliest time at which it is hit in the event window.

Radial Dependence

The radial dependence of the likelihood fitter was also investigated by generating 1000 3 MeV electron events within 8 radial shells through the scintillator. The resolution and radial bias were then calculated for each bin and the results are shown in Figure 5.17. The resolution of the likelihood fitter has very little radial dependence in unloaded scintillator, ranging from 11 cm at the centre of the detector to 9.5 cm at around 4 to 5 m.

The radial bias increases gradually to zero around 4 to 5 m, increasing faster

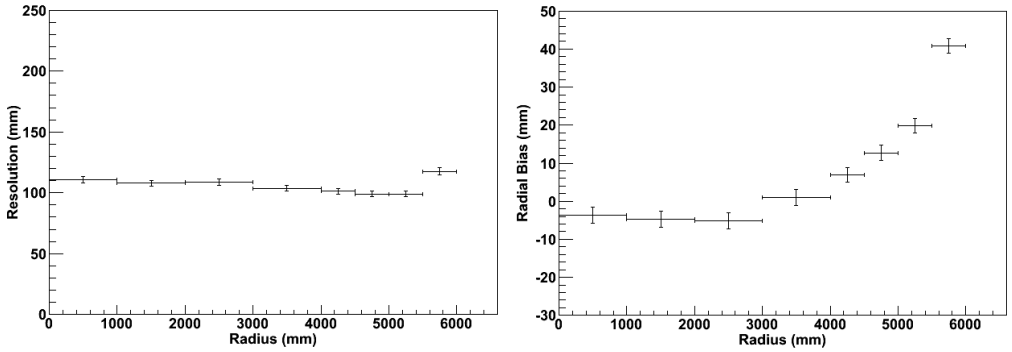

(a) Likelihood fitter resolution vs radius (b) Likelihood fitter radial bias vs radius

Figure 5.17: The resolution and radial bias of the likelihood fitter at different radii in unloaded scintillator, generated by simulating 3 MeV electron events.

towards the edge of the detector. Despite this, the size of the radial bias is below 1 cm for events within a 5 m radius. Closer to the edge, the radial bias becomes larger, although still less than 4 cm. This is due to the optical effects of refraction and total internal reflection observed near the AV breaking down the assumption of a straight line path through the detector for the photons.

The fitter works well across all regions without any great variation in performance with the resolution varying between 9 and 11 cm and the radial bias always being less than 4 cm in either direction and less than 1 cm below 4.5 m.

Material Dependence

These studies of the energy and radial dependence were repeated for different loadings of double beta decay isotopes. Different effective speeds and PDFs were used for each material to take account of the different optical properties.

- Nd loaded scintillator

The energy and radial dependences of the likelihood fitter are plotted for 0.1, 0.3 and 0.5% Nd in Figure 5.18, alongside those of unloaded scintillator. The results follow similar trends to the unloaded scintillator. The resolution, at 3 MeV, gets slightly worse as loading increases, rising from about 10 cm for unloaded scintillator to 13 cm at 0.5% loading as there are fewer PMTs to sum over when

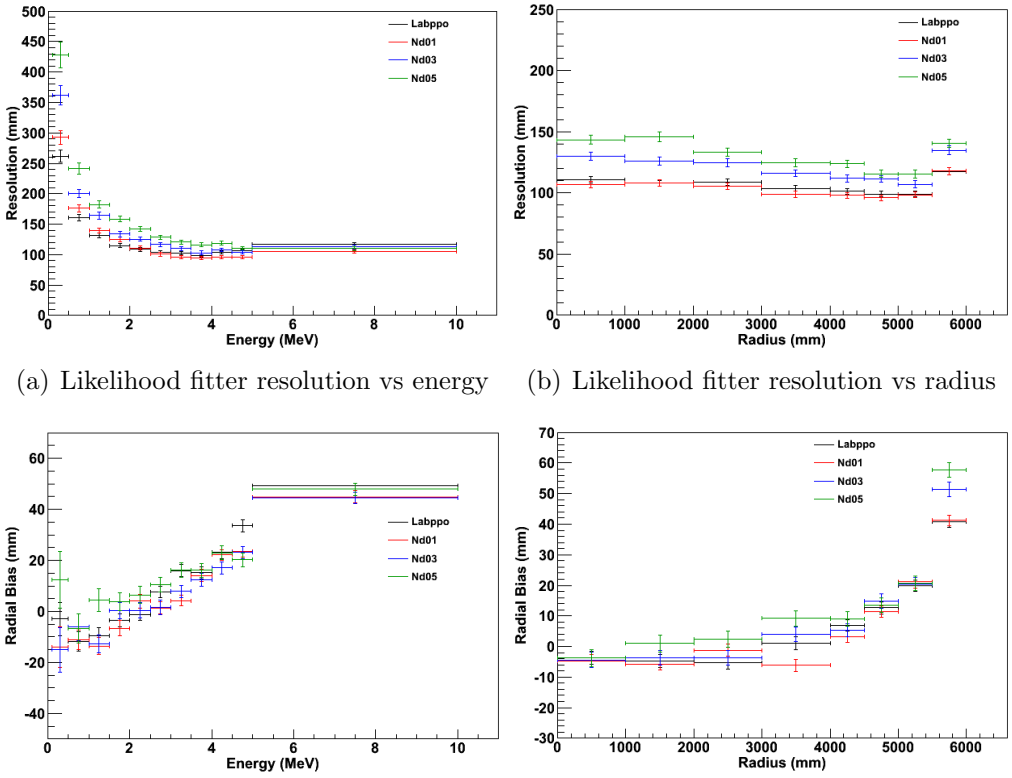

(a) Likelihood fitter resolution vs energy

(b) Likelihood fitter resolution vs radius

(c) Likelihood fitter radial bias vs energy

(d) Likelihood fitter radial bias vs radius

Figure 5.18: The resolution of the likelihood fitter at different energies and radii, generated by simulating electron events in a detector filled with unloaded scintillator and 0.1, 0.3 and 0.5% Nd-loaded scintillator. The energy events are simulated filling the detector in 11 different energy bins while the radial events are simulated at 3 MeV in 8 different radial bins.

calculating the log-likelihood. The radial bias is unchanged when compared to the unloaded scintillator. This suggests that adding neodymium into the scintillator won't adversely affect the performance of the likelihood fitter.

- Te loaded scintillator (Type A)

The energy and radial dependences are plotted for 0.1, 0.3 and 0.5% Te , using the type A optics described in Chapter 4, on Figure 5.19 with that of unloaded scintillator. The results follow similar trends to the unloaded scintillator but the resolution, at 3MeV, worsens as loading increases, rising from 10 cm unloaded scintillator to 18 cm at 0.5% loading. The radial dependence becomes much stronger due to the extra scattering, reaching around 25 cm in the centre compared to 15

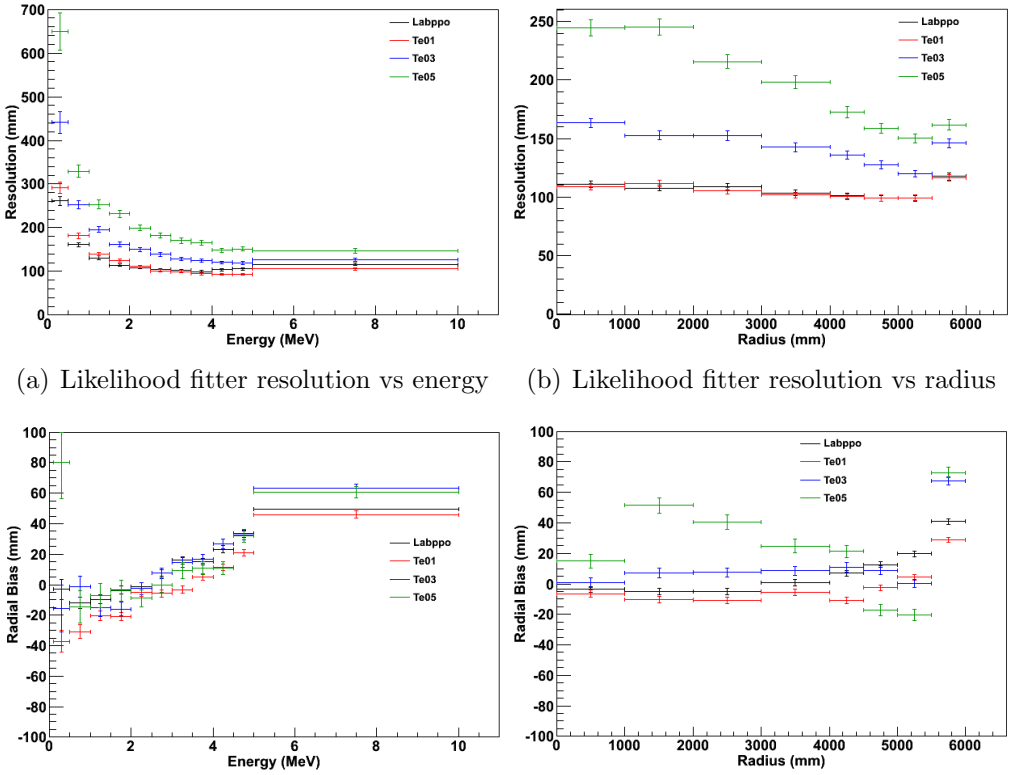

(a) Likelihood fitter resolution vs energy

(b) Likelihood fitter resolution vs radius

(c) Likelihood fitter radial bias vs energy

(d) Likelihood fitter radial bias vs radius

Figure 5.19: The resolution and radial bias of the likelihood fitter at different energy and radii generating by simulating electron events for a detector filled with unloaded scintillator and 0.1, 0.3 and 0.5% Type-A Te-loaded scintillator. The energy events are simulated for events filling the detector for 11 different energy bins while the radial events are simulated at 3 MeV in 8 different radial bins.

cm near the edge, with a similar increase in the amount of radial bias.

While a single PDF fitter such as this is still able to produce reasonable results with this formulation of Te-loaded scintillator, its radial dependence becomes much worse when compared to that of the unloaded scintillator.

- Te loaded scintillator (Type B)

These dependencies were also examined for the Type B formulation of tellurium loading, accompanied by bisMSB as a secondary wavelength shifter. The energy and radial dependence for 0.1, 0.3 and 0.5% loading are shown in Figure 5.20, with that of the unloaded scintillator.

Once again, the energy dependence and radial dependence follow similar trends as were observed for the unloaded scintillator. Increasing the loading worsens the

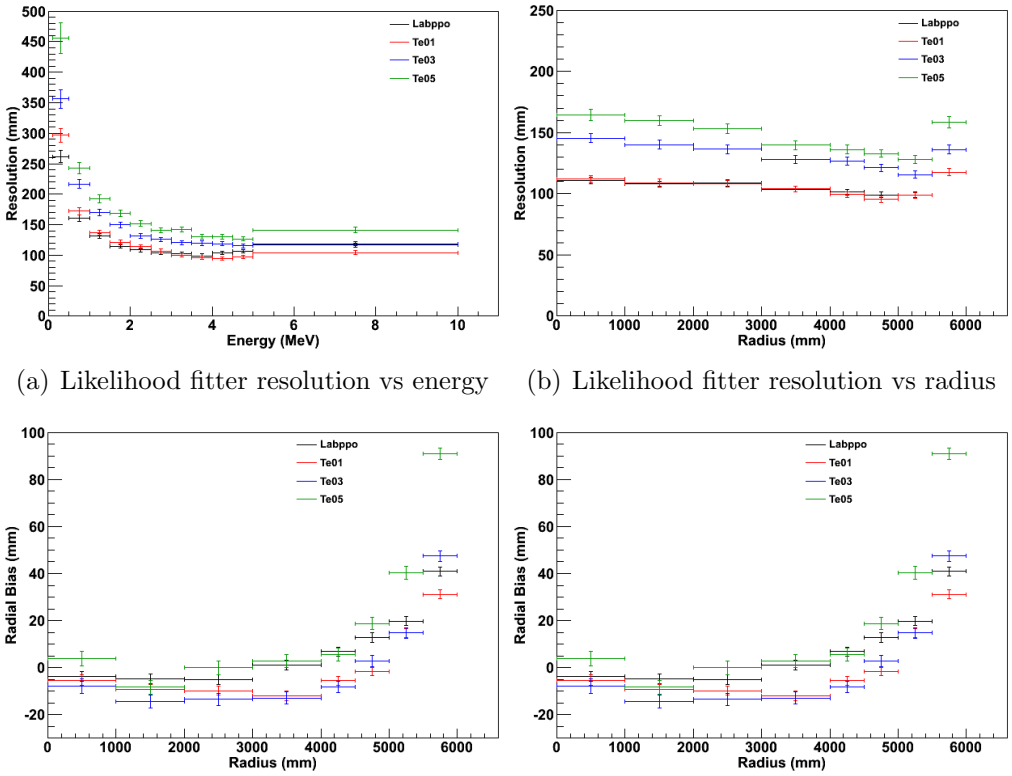

(a) Likelihood fitter resolution vs energy

(b) Likelihood fitter resolution vs radius

(c) Likelihood fitter radial bias vs energy

(d) Likelihood fitter radial bias vs radius

Figure 5.20: The resolution of the likelihood fitter at different energies and radii, generated by simulating electron events in a detector filled with unloaded scintillator and 0.1, 0.3 and 0.5% Type B Te-loaded scintillator. The energy events are simulated for events filling the detector in 11 different energy bins while the radial events are simulated at 3 MeV in 8 different radial bins.

resolution as the number of hits drops due to the extra absorption, rising from about 10 cm for unloaded scintillator to 14 cm at 0.3% loading at around 3 MeV. Despite this, the resolution still remains less than 15 cm at 3 MeV all through the detector, even in the centre where the drop in the number of PMT hits due to the absorption is the highest. The radial bias is similar to that found for unloaded scintillator. These results show that the position resolution for the type B tellurium loading isn't drastically affected by the additional absorption.

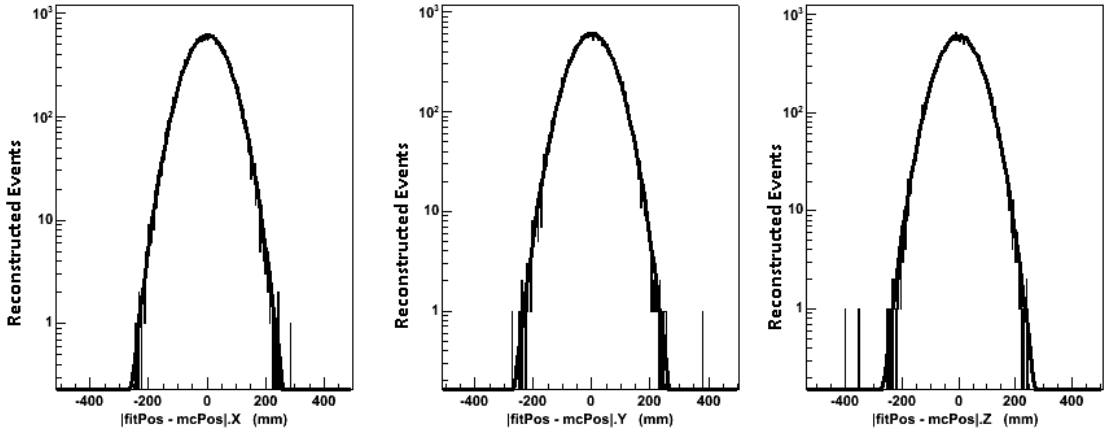

(a) Events in the centre of the detector

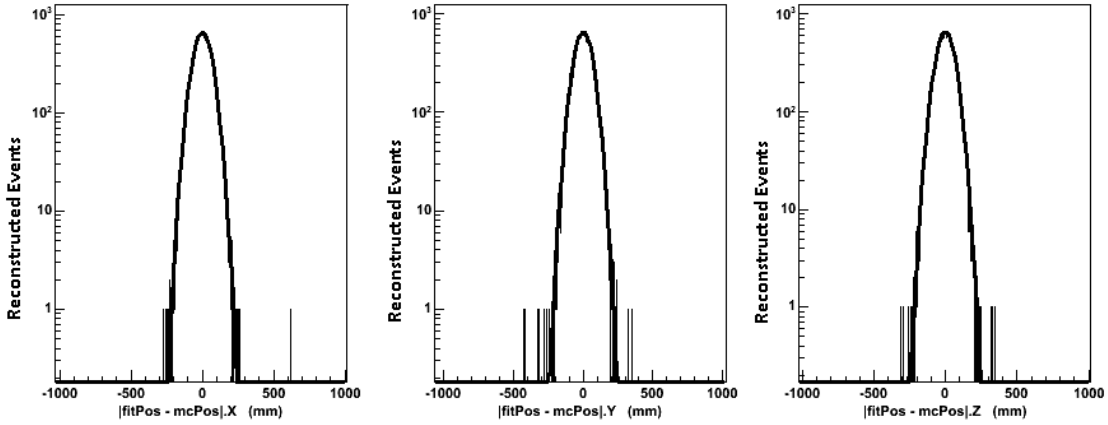

(b) Events between 3 and 4 m radius

Figure 5.21: The difference between fitted and Monte-Carlo positions for the x, y, z components and the distance between the fitted and Monte-Carlo positions generated for 50,000 events fit using the likelihood fitter in a) the centre of the detector and b) between 3 and 4 m radius.

Reconstruction Tails

The tails of the fit were investigated by simulating 50,000 3 MeV electron events, in the centre of the detector and between 3 and 4 m, the results of which are plotted in Figure 5.21. The majority of events are found to be well described by the Gaussian fit with only one 1 event out of 50,000 is found to fit more than 50 cm away in each position. The quadFitter result for this event is also in the tails of the fit suggesting that the cause of this is something intrinsic to the event rather than caused by the fit. This event doesn't have an unusual number of hits,

figure of merit/likelihood value or position and the time residuals appear to be distributed normally. The positions of the PMT hits look to be skewed such as to give this fit, e.g. an excess of hits in the positive x-direction causing the fit to have a bias in the x-direction.

5.3.6 Potential further modifications

While the likelihood fitter works well across different energies, positions and materials, it could potentially be improved. The current fitter is tuned to give the best results at 3 MeV but, by using the number of PMT hits as an estimate of the energy of the event, a different effective speed and PDF could be used for different energy regions and so potentially reduce the radial bias and improve the resolution at lower and higher energies.

Similarly, while the unloaded scintillator and neodymium loading don't show a strong radial dependence, the Type A form of tellurium reveals that large amounts of scattering can introduce a noticeable radial dependence. In this case, different PDFs for different regions of the detector could prove useful.

While the current PDF deals only with the hit time and assumes that the photon takes a direct line of flight from event to PMT, in high scattering situations, this approximation will become less valid. In those cases, the use of charge information could help. The charge deposited in each PMT could also provide a tool to deal with PMTs hit by multiple photons.

5.3.7 Summary of likelihood fitter properties

With these improvements, the likelihood fitter looks to be a useful tool in fitting events. With the new optimiser and seed, the proportion of events that are successfully fit improves noticeably, particularly at low energy.

For 3 MeV electrons, it will reconstruct events with a resolution of 10 cm and a

radial bias of less than 1 cm. By using new effective speeds and PDFs for different materials, it also proves to work for loading of different double beta decay isotopes, showing a resolution of 13 cm for 0.5% Nd-loading and 14 cm for 0.3% Te-loading (Type B). While at 0.4 seconds per event at 3 MeV, it is relatively slow compared to the quadFitter, it is still quick compared to the time taken to simulate a Monte Carlo event, which is around 8 seconds per event at 3 MeV.

This meets the neccessary requirements in terms of position resolution and bias. The behaviour of the fitter tails, although only misfitting 1 in 50,000 events, may warrant further investigation but are probably explained by the distribution of the PMT hits of the event.

5.4 More general treatment of scattering

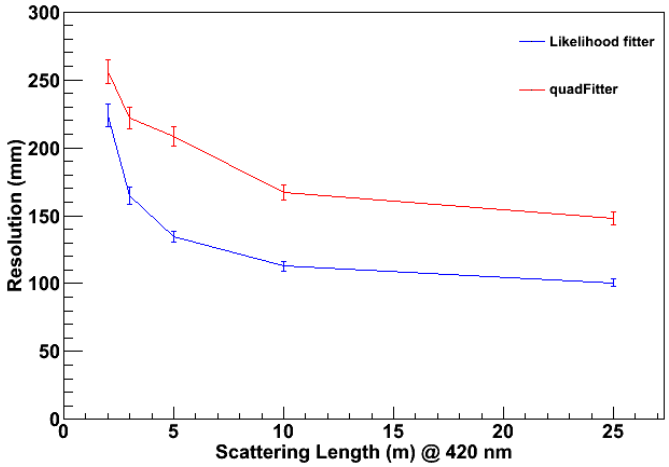

Figure 5.22: The resolution of the likelihood fitter and the quadFitter at 3 MeV, reco-ordinated for different amounts of scattering. The scattering length along the x-axis is given as the Rayleigh scattering length at 420 nm.

In order to investigate the general affect of increased scattering on the position resolution, new PDFs and transit times were generated for both the quadFitter and likelihood fitter. For unloaded scintillator, the Rayleigh scattering length at 420 nm has been measured to be around 25 m. This was then scaled down to 10,

5, 3, and 2 m and the fitters were re-coordinated to reduce the radial bias. The resolution at 3 MeV was then found by simulating electron events with these new scattering lengths. This is plotted on Figure 5.22.

It should be noted that the fitters are reasonably robust with respect to scattering, still giving fitter resolutions of just over 20 cm for the likelihood fitter and 26 cm for the quadFitter at a scattering length of 2 m. However, by 1 m scattering length, they begin to struggle, particularly in the case of the likelihood fitter which only returned around 50% of the events it was asked to fit. In this case, a new approach would be required. However, in general, the fitters are able to handle moderate amounts of scattering once tuned to the new optical properties.

5.5 Conclusion

As covered in this chapter, the quadFitter and likelihood based position fitter meet the requirements necessary, reconstructing the position across a range of energies and through the entirety of the fiducial volume of the SNO+ detector. In addition, they can be adapted to different scintillator mixtures and show a good ability to cope with the increased absorption and scattering brought by the loading of double beta decay isotopes.

Chapter 6

Identification of Tl208 external backgrounds

One of the most significant backgrounds in SNO+ will be from natural radioactive decays in the acrylic vessel (AV), hold-down ropes and PMTs. These are known as external backgrounds as they originate from sources outside the scintillator volume. One major contribution to this is from ^{208}Tl in the AV which will be produced from 35% of Thorium chain decays and will decay to ^{208}Pb with a halflife of around 3 minutes producing a β and several γs of energies up to 2.614 Mev.

If these 2.6 MeV gammas travel into the scintillator, they can reconstruct at energies within the double beta decay signal window and so could be mistaken for signal events, providing a background for any search for double beta decay in SNO+. Since the amount of external background events will fall off with the distance from the edge of the detector, this will impose a limit upon the chosen fiducial volume of SNO+.

This chapter describes a technique developed using the characteristic shape of the time residuals of these external backgrounds from the AV to distinguish these events from potential signal (electron) events and how this can be applied to increase the fiducial volume of SNO+. The application of this technique to

other external backgrounds from the hold-down ropes, water shielding and PMTs is then investigated.

6.1 Defining the fiducial volume of SNO+

In order to limit the effect of external backgrounds, a fiducial volume is defined within which events will not be background dominated. Outside this, events are statistically likely to be background events and, so, most of the signal information is contained within the fiducial volume.

In SNO+, the fiducial volume is defined, in this thesis, as the radius within which the number of reconstructed events from external backgrounds becomes equal to the number of events from ^{8}B solar neutrinos, which are irreducible and, so, put a fundamental limit on the number of backgrounds. In the event of a full analysis, the fiducial volume will be fit taken into account both signal and background but this method will give an estimate of how the technique described in this chapter can reduce the level of external backgrounds.

Figure 6.1 a) shows the expected number of events per year reconstructing in the tellurium signal window within a given fiducial volume for ^{208}Tl events from the AV, assuming an activity of 1.38×10^{6} decays per year[81], in black and for the solar ^{8}B neutrino flux in blue. Using the definition of the fiducial volume as the volume such that the amount of external background events is equal to that of the solar neutrinos, considering the AV backgrounds alone and ignoring activity from the ropes and PMTs, which will be discussed later in the chapter, SNO+ will have a fiducial radius of 3.9 m for the tellurium signal window.

Also shown are the same results within the neodymium signal window. In this case, external backgrounds from the AV produce a fiducial volume of 5.1 m. This is a larger volume than for tellurium as the background rate is lower at this higher energy, further from the energy peak caused by the 2.6 MeV gamma. ^{208}Tl can

produce signals in the tellurium window from just the energy deposition of the single 2.6 MeV gamma while the neodymium window relies upon the high energy tails of the reconstruction of a single gamma or on the additional energy deposition from the lower energy gammas to raise itself into this window.

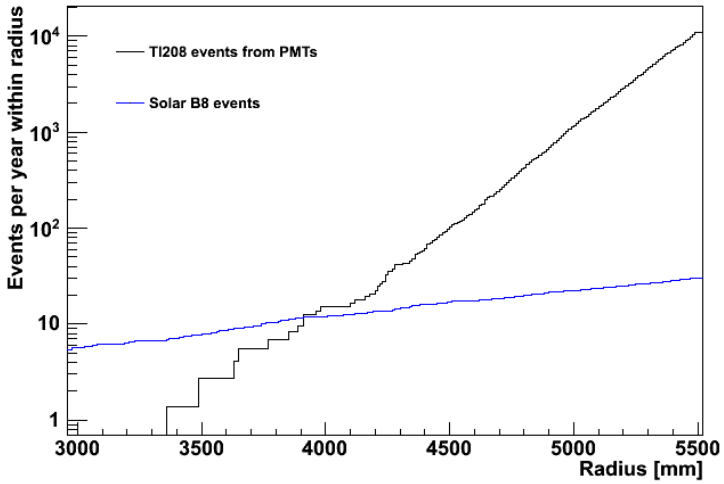

(a) Te energy window

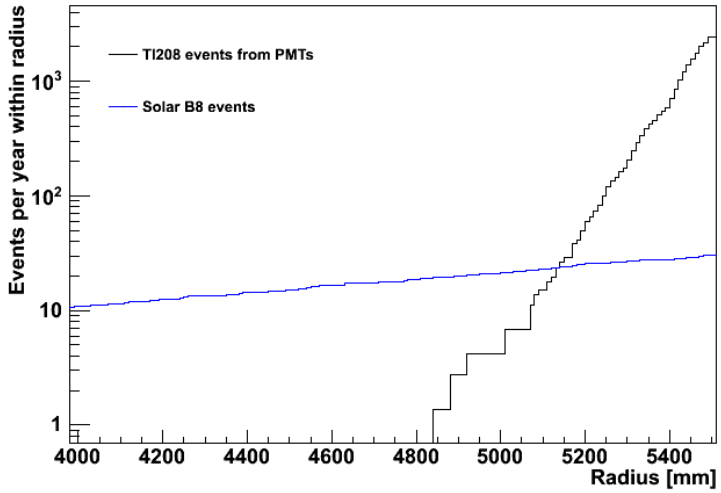

(b) Nd energy window

Figure 6.1: Events per year reconstructing within a given fiducial radius in a) the tellurium energy window about 2.5 MeV and b) the neodymium energy window at 3.3 MeV from ^{208}Tl decays in the AV. This plotted alongside the events from solar ^{8}B neutrinos. These plots are for unloaded scintillator.

6.2 Background identification

6.2.1 Technique to identify these events

A technique was developed to identify a subset of these events. This is based on looking for early light from low energy gammas in the decay and from multiple Compton interactions along the the trajectory. This is observed as differences in the shape of the time residuals of the early light between the ^{208}Tl events in the AV and signal (electron) events reconstructing at the same position and energy, shown on Figure 6.2. The bulk of the light produced in the event will be from the 2.6 MeV gamma but additional light will be produced as lower energy gammas make it into the scintillator and deposit their energy closer to the edge of the detector volume or the beta from the decay produces Cherenkov light in the acrylic vessel. This light may reach the nearby PMTs first and so cause a smearing out of the rising edge of the PMT time residual distribution.

Another contribution to the rejection will be based on the direction nature of those gammas which reconstruct in the scintillator. Those that make it into the scintillator, particularly in the case of the ropes or the PMTs, will be travelling inwards towards the centre of the detector. As they travel inwards, they can deposit their energy through multiple Compton scatters near the edge of the detector as opposed to betas which will lose all their energy in a very short distance. Since the optics change quickly with radius near the AV, due to the refraction, the resulting time residual shape will change. This effect isn't noticed with internal gamma events as they are less likely to be focussed along the radial direction.

6.2.2 Application of this to individual events

In order to seperate these on an event by event basis, two time residual PDFs were generated, in the same way as defined for the likelihood fitter described in section

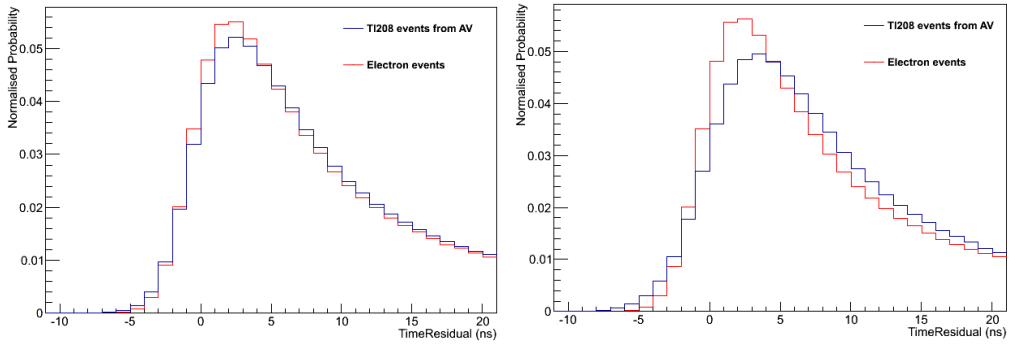

(a) Te energy window (b) Nd energy window

Figure 6.2: Comparison of the normalised time residual distributions of ^{208}Tl events from the AV, in blue, and electron events, in red, both reconstructing between 5.4 and 5.5 m and in the a) tellurium energy window and b) neodymium energy window. These plots are for unloaded scintillator.

5.3, for ^{208}Tl events in the AV and for electron events at the same reconstructed energy and position. An individual event is then compared to each of these PDF in turn and a log-likelihood value calculated for each. The difference between these two likelihood values is then calculated:

$$\Delta = \text{logLike(electron)} - \text{logLike(Tl208)} \tag{6.1}$$

It is expected that signal events should return a value greater than zero while the external background events should be less than zero, thus allowing the two event types to be distinguished. Figure 6.3 shows this value Δ plotted for a test sample of electron events, in black, and of ^{208}Tl events, in red. A significant fraction of the ^{208}Tl events can then be separated from the electron events by cutting for these events at an appropriate value of Δ. As might be expected from the time residuals comparisons, the neodymium likelihood difference shows stronger seperation than that of the tellurium energy window.

Due to the effects of absorption and scattering, as well as optical effects such as refraction and total internal reflection near the AV, the shape of the time residual PDFs will have a radial dependence and so different sets of the PDFs

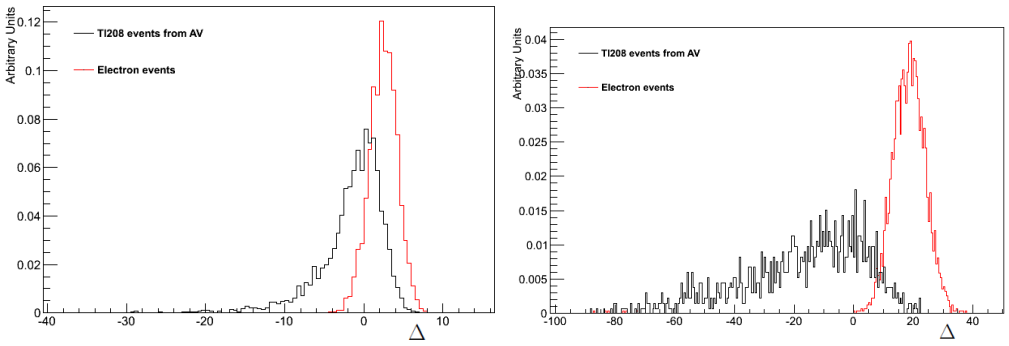

(a) Te energy window (b) Nd energy window

Figure 6.3: Comparison of the likelihood difference value Δ for test samples of ^{208}Tl events from the AV, in black, and electron events, in red, both reconstructing between 5.4 and 5.5 m and in the a) tellurium energy window and b) neodymium energy window. These plots are for unloaded scintillator.

were used at different radii. This presents problems due to limited statistics when trying to create PDFs for lower radii as, since the events fall off exponentially with radius, generating enough Monte-Carlo events requires a lot of computing time and storage. This is particularly true in the case of the neodymium energy window as this has a lower event rate to begin with due the energy window being further from the 2.6 MeV gamma.

The optimised position of this cut will depend on the relative levels of all other backgrounds and on the signal loss. For the following analysis, the cut hasn't been optimised but has been fixed at a position of 0.

6.3 Performance for backgrounds from the AV

Figures 6.4 a) and b) show the results of this cut for the tellurium and neodymium energy windows in unloaded scintillator. The cut applied to tellurium will move the fiducial volume from 3.9 m out to 4.2 m at a loss of 7.6 % of the signal. This would increase the fraction of the signal in the active volume of the detector from 27.5 % at 3.9 m to, including only that which passes the cut, to 31.7 % at 4.2 m.

For the neodymium window, the fiducial volume is pushed from 5.1 m to 5.2 m

with a signal sacrifice of less than 0.1 %, since there is a much clearer seperation at higher energies. This would increase the active fraction from 61.4 % to 65.1 %.

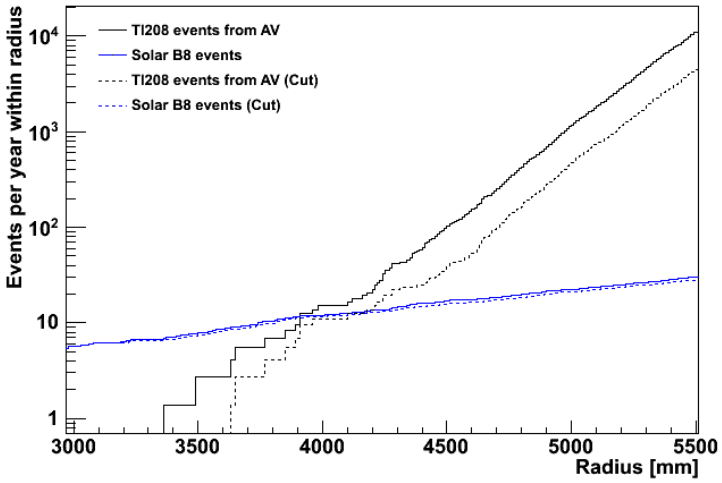

(a) Te energy window

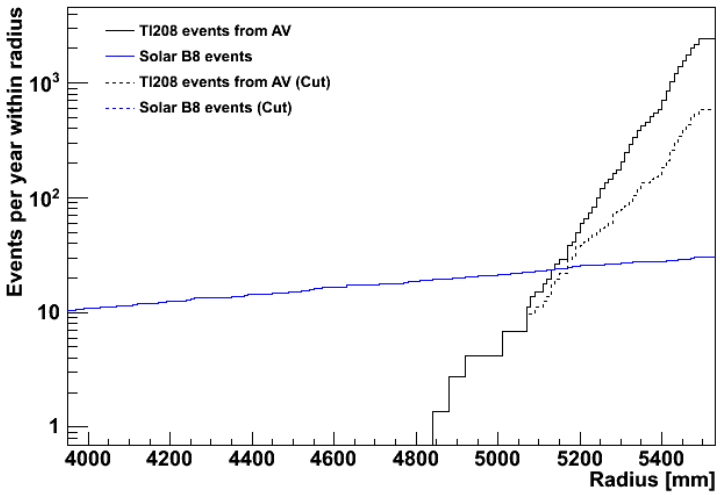

(b) Nd energy window

Figure 6.4: ^{208}Tl events per year from the AV reconstructing within a given fiducial radius, in a) the tellurium signal window around 2.5 MeV and b) the neodymium signal window at 3.3 MeV, shown with and without the rejection cut. Also shown are the events from solar ^{8}B neutrinos. These plots are for unloaded scintillator.

6.3.1 With different materials

In order to investigate how the different optical properties, introduced by the loading of double beta decay isotopes into the scintillator, will affect the fiducial

volume and the performance of the identification technique, new PDFs were generated and the optimal fiducial radius, with and without the cut, calculated for two different techniques of tellurium loading, labelled in Chapter 4 as Type A and B, shown in Figures 6.5 and 6.6, and for neodymium loading, shown in Figure 6.7.

For the type A tellurium loading, it should be noted that the identification technique still works, improving the fiducial radius from 3.9 to 4.1 m for 0.1 %, 4.2 to 4.4 m for 0.3 %, and 4.2 to 4.3 m for 0.5 %. For the type B tellurium loading, the identification technique is similarly unaffected by the additional optics, improving the fiducial radius from 4.0 to 4.2 m for 0.1 % and 4.3 to 4.6 m for 0.3 % with a loss of of 5-7 % of the signal. The cut also continues to work for lower concentrations of neodymium loading.

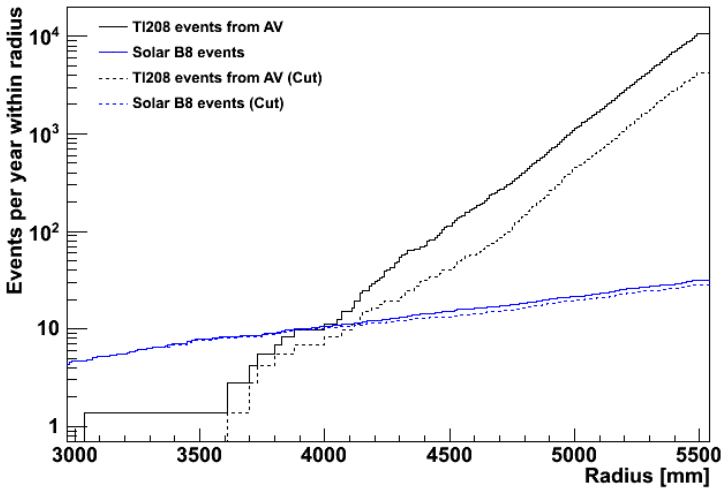

(a) 0.1 % loading

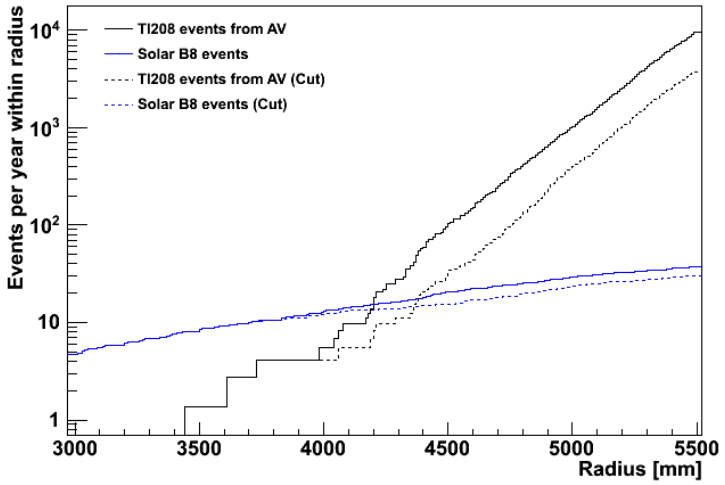

(b) 0.3 % loading

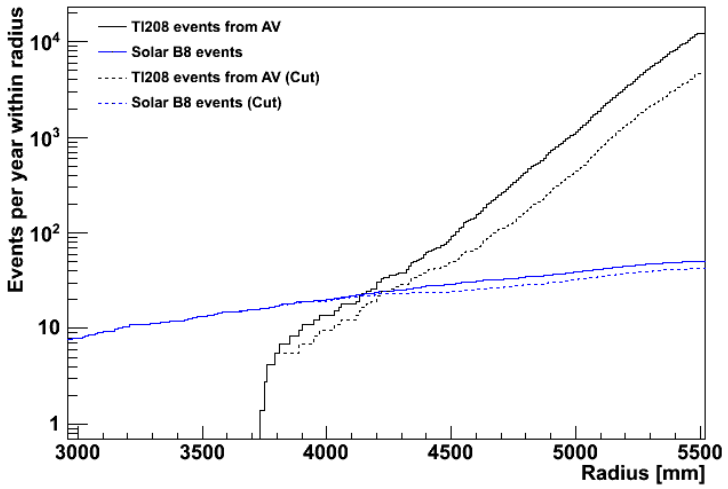

(c) 0.5 % loading

Figure 6.5: ^{208}Tl events per year from the AV reconstructing within a given fiducial radius, assuming a tellurium signal window around 2.5 MeV. Also shown are the events from solar ^{8}B neutrinos. These plots are for Type A Te-loaded scintillator for loadings of 0.1 %, 0.3 % and 0.5 %.

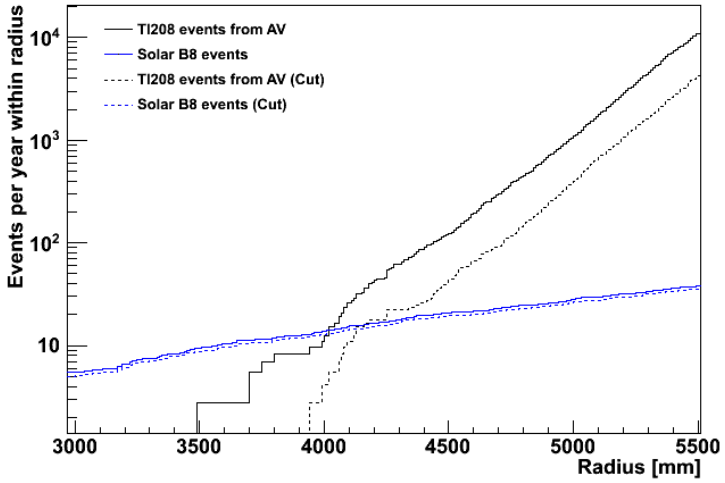

(a) 0.1 % loading

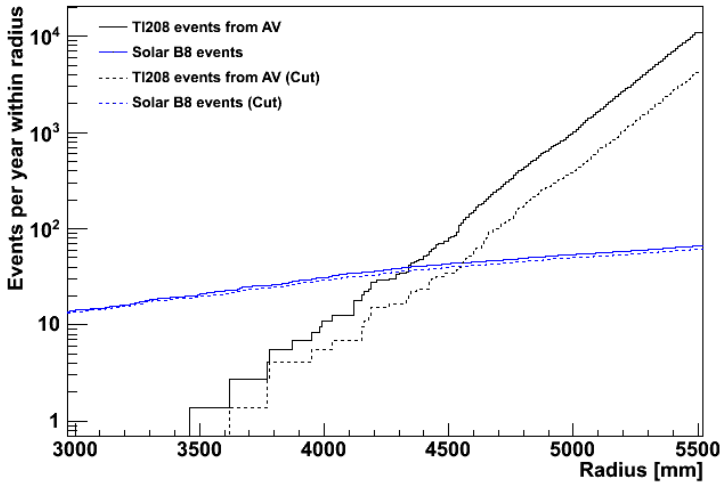

(b) 0.3 % loading

Figure 6.6: ^{208}Tl events per year from the AV reconstructing within a given fiducial radius, assuming a tellurium signal window at 2.5 MeV. Also shown are the events from solar ^{8}B neutrinos. These plots are for Type B Te-loaded scintillator for loadings of 0.1 % and 0.3 %.

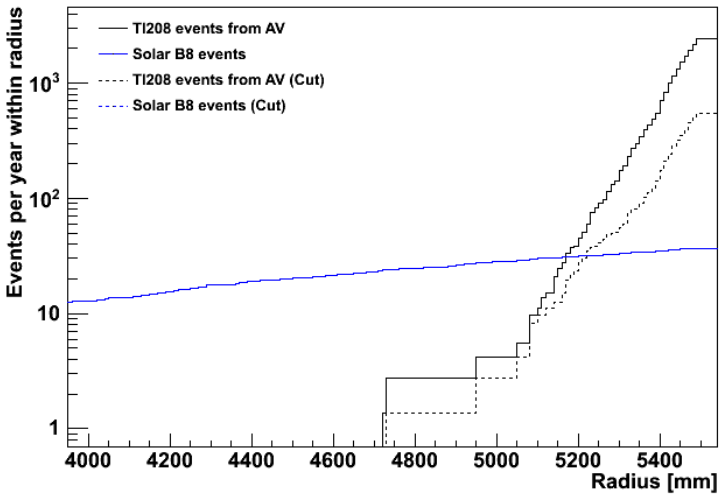

(a) 0.1 % loading

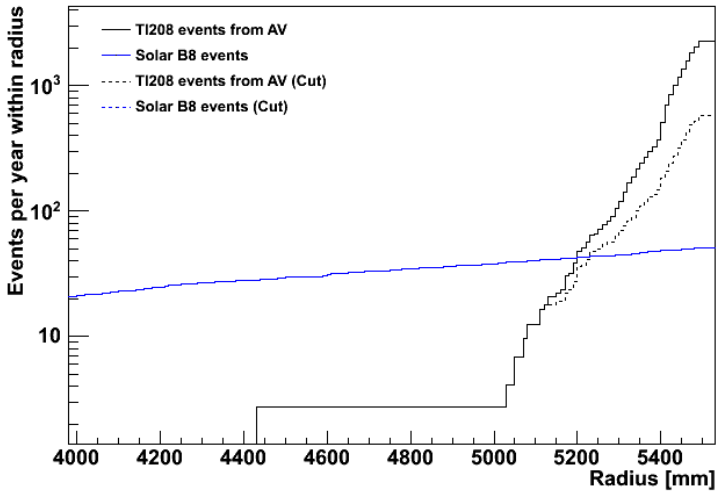

(b) 0.3 % loading

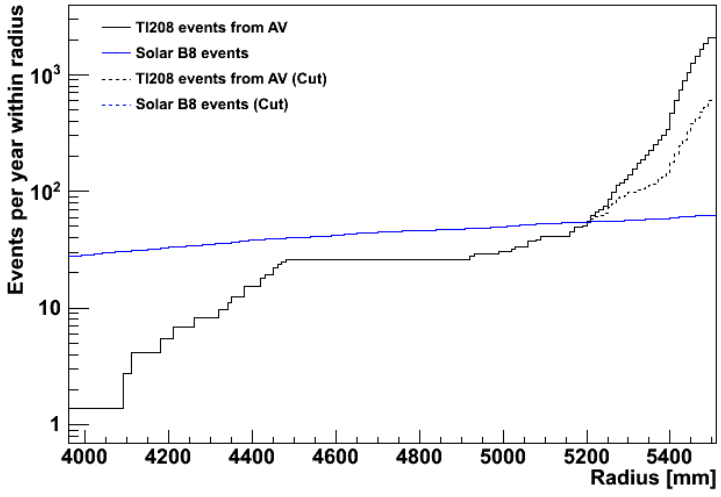

(c) 0.5 % loading

Figure 6.7: ^{208}Tl events per year from the AV reconstructing within a given fiducial radius, assuming a neodymium signal window around 3.3 MeV. Also shown are the events from solar ^{8}B neutrinos. These plots are for Nd-loaded scintillator for loadings of 0.1 %, 0.3 % and 0.5 %.

Interestingly, it looks as if the effect of increasing the loading of the scintillator leads to an increased fiducial radius for the tellurium energy region. This can be understood by considering the shapes of the signal, solar background and AV background energy spectrum, shown on Figure 6.8. As the resolution worsens, the energy window of the signal will get wider and so increase the solar and external backgrounds in the window. For the ^{208}Tl, it is dominated by a peak at 2.6 MeV, quite close to to the tellurium signal peak at 2.5 MeV, so these already have a significant amount of overlap, with only the tails outside the energy window, and so the widening energy window only results in a slight increase in the background level. The ^{8}B solar background, on the other hand, is effectively flat in this region and so the larger energy window covers much more of the solar energy spectrum and so these backgrounds increase significantly. Since the definition of the fiducial volume is limited by the solar background level, that means the fiducial volume, as defined here, can actually increase as the resolution worsens. This is not an artifact of the cut but can be seen on the uncut events as well.

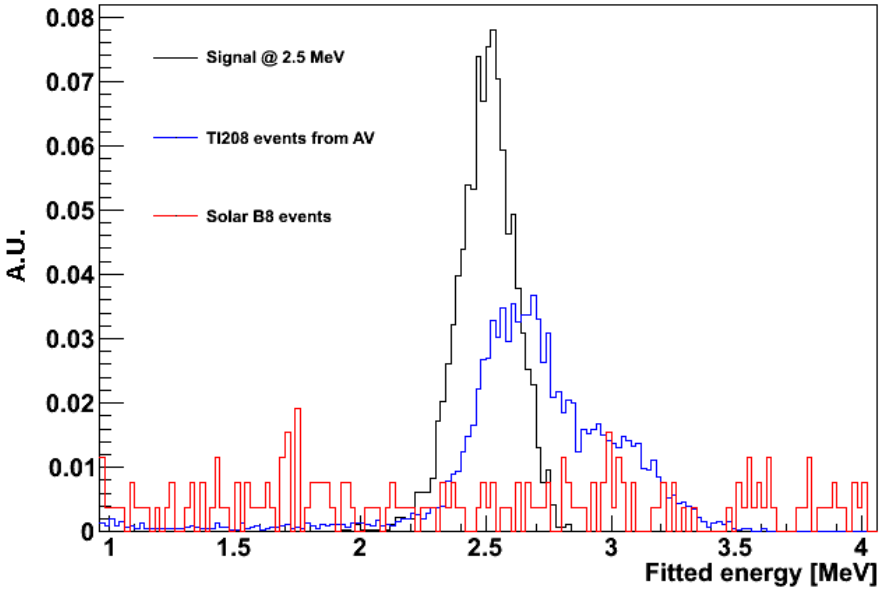

Figure 6.8: Normalised reconstructed energy spectra of ^{208}Tl decays from the AV, solar ^{8}B events and an electron signal at 2.5 MeV.

6.3.2 General behaviour with position and energy resolution

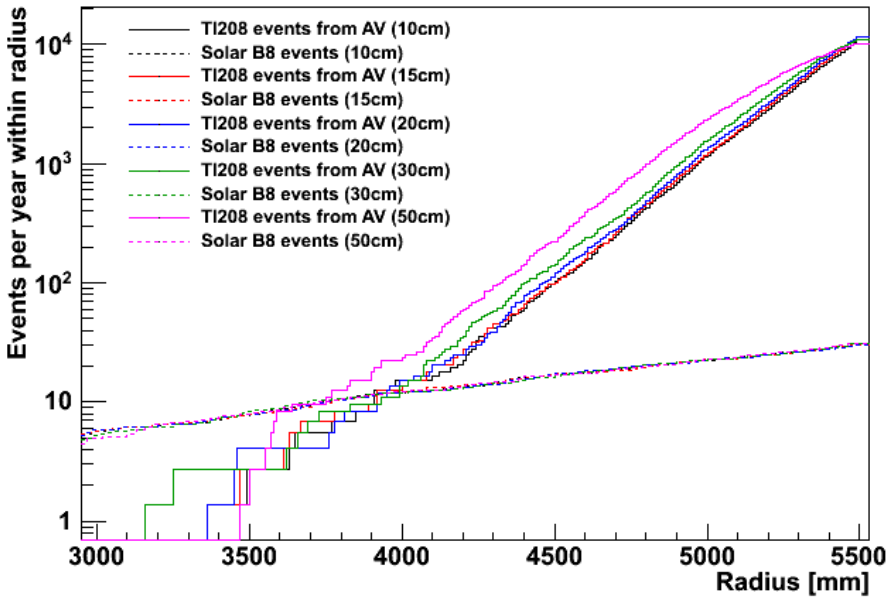

Figure 6.9: Events per year reconstructing within a given fiducial radius from ^{208}Tl decays in the AV and ^{8}B solar neutrinos for artificially worsened position resolutions.

The effect of position resolution was investigated by artificially worsening the position resolution of the scintillator, while keeping the same light levels, by adding a random number drawn from a Gaussian distribution to the fitted position in each of the x, y and z directions. This technique was used to generate new results for position resolutions of 15, 20, 30 and 50 cm to be compared to the 10 cm seen for unloaded scintillator. The results are plotted on Figure 6.9. It can be seen that for position resolutions of 20 cm and below, the change in resolution doesn't make a great deal of difference to the reconstructed position of the external backgrounds or the fiducial volume. By 30 cm, a shift towards the centre of the detector begins to be noticeable and, by 50 cm, this effect becomes large enough to shift the fiducial radius inward by over 10 cm. This could be expected as the Compton scattering length of the gammas in scintillator is 26 cm and so a position resolution worse than this would begin to cause a noticeable effect on how the gammas reconstruct.

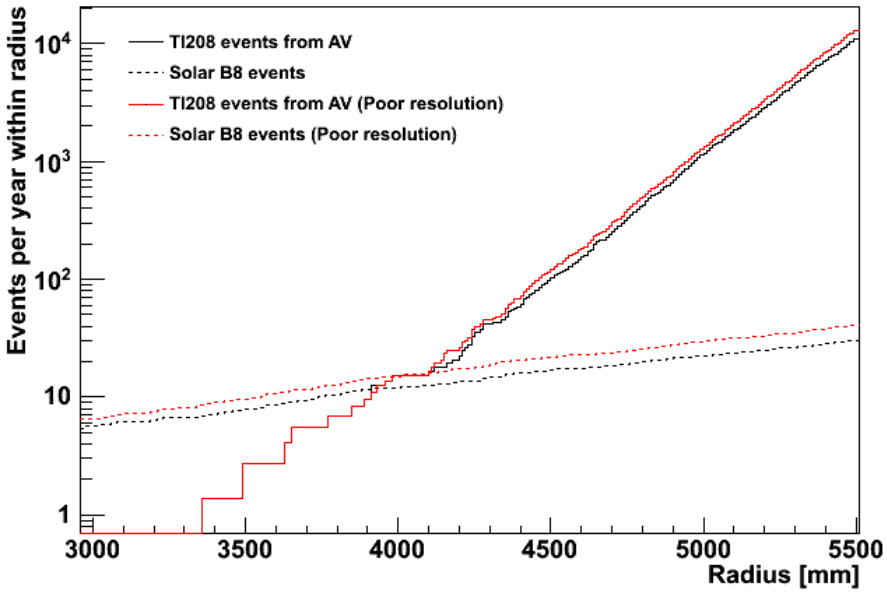

Figure 6.10: Events per year reconstructing within a given fiducial radius from ^{208}Tl decays in the AV and ^{8}B solar neutrinos for an artificially worsened energy resolution.

This puts a constraint on the requirements of the position reconstruction.

The effect of the energy resolution was tested by widening the spread of the number of PMT hits used to calculate the energy by one sigma using random numbers drawn from a Gaussian distribution. This is shown in Figure 6.10. As observed when investigated the material dependence, it is seen that the poor energy resolution increases the number of AV backgrounds slightly but increases the solar backgrounds significantly resulting in a larger fiducial volume.

6.4 Performance for ropes

Another major source of background, around the same level as that of the AV backgrounds, is expected to come from radioactive decays in the hold-down ropes. This has an expected decay rate of 2.3×10^6 decays per year for ^{208}Tl[81]. This analysis was repeated, using the same PDF, for the decays in the ropes and the results are shown in Figure 6.11 for unloaded scintillator. The results show that the

technique can also be applied to backgrounds from the hold-down ropes, pushing the fiducial volume outwards from 3.8 to 4.0 m, with a signal sacrifice of 6 %, increasing the active volume of the detector from 25.4 % to 27.9 %, taking into account only the signal that passes the cut.

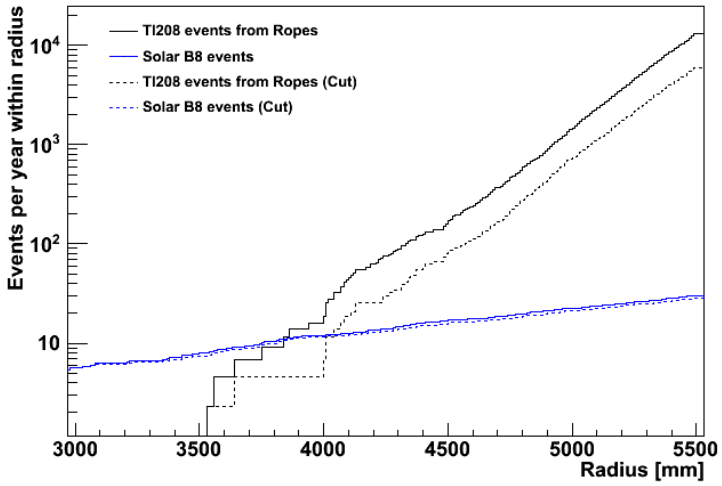

Figure 6.11: ^{208}Tl events per year from the hold-down ropes reconstructing within a fiducial radius, assuming a tellurium signal window around 2.5 MeV, shown with and without the rejection cut. Also shown are the events from solar ^{8}B neutrinos. This plot is for unloaded scintillator.

Since the ropes lay on top of the AV, it is likely that these backgrounds will not be evenly distributed throughout the detector. To investigate this effect, the top and bottom half of the detector were considered seperately as two distinct fiducial volumes and the analysis was repeated. The results are shown in Figure 6.12 and it can be seen that there are significantly more rope backgrounds in the top half of the AV, although the rejection technique applies to both, the top half improving its fiducial volume from 3.6 to 4.0 m while the bottom half sees an increase of 4.2 to 4.5 m, both with a sacrifice of 5-7 % of the signal.

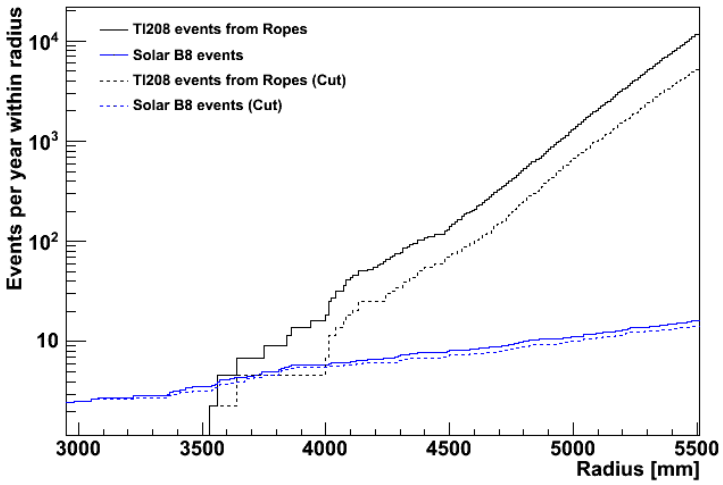

(a) Events in top half of detector

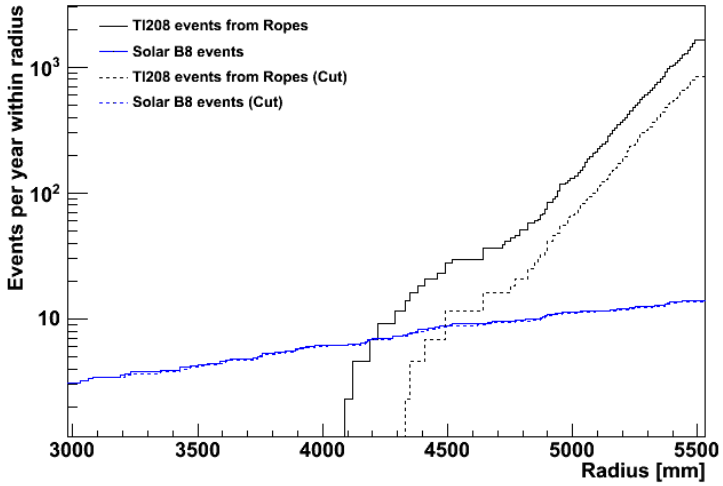

(b) Events in bottom half of detector

Figure 6.12: ^{208}Tl events per year from the hold-down ropes reconstructing within a fiducial radius in a) the top half and b) the bottom half of the detector, assuming a tellurium signal window around 2.5 MeV, shown with and without the rejection cut. Also shown are the events from solar ^{8}B neutrinos in that region of the detector. These plots are for unloaded scintillator.

6.5 Performance for other external backgrounds

Other external backgrounds that must be considered are decays from dust on the inner surface of the AV, in which 4.2×10^5 ^{208}Tl decays per year are expected, in the water shielding between the PSUP and the AV, expecting 3.74×10^6 per year, and from the PMTs, expecting 1.47×10^{10} decays per year[81]. These were simulated for unloaded scintillator and the indentification technique applied, the results are shown in 6.13. As before, the technique succeeds in tagging the background events.

Despite their high rate, the gammas from the PMTs are suppressed by a factor of order 10^{-6} by the time they reach the edge of the acrylic vessel due to the self shielding of the detector. This makes a direct simulation difficult so instead they have been approximated by simulating a lower rate of gammas, beginning at a radius of 6.1 m, pointing directly inward, a reasonable assumption as those gammas which reach the AV will have a strongly forward direction with the average angle relative to the centre of the detector being $<\cos\theta>$=0.957.

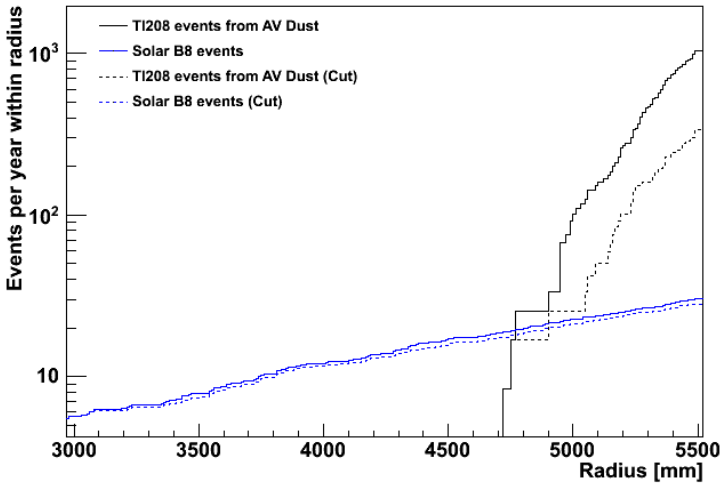

(a) Tl208 in dust on the AV surface

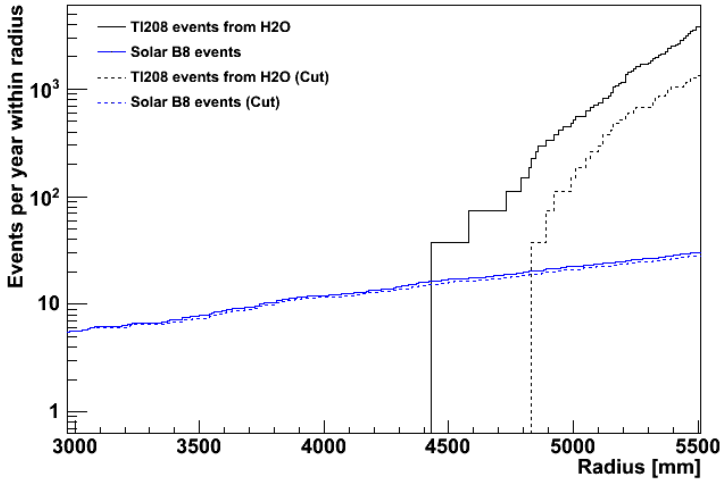

(b) Tl208 in water shielding

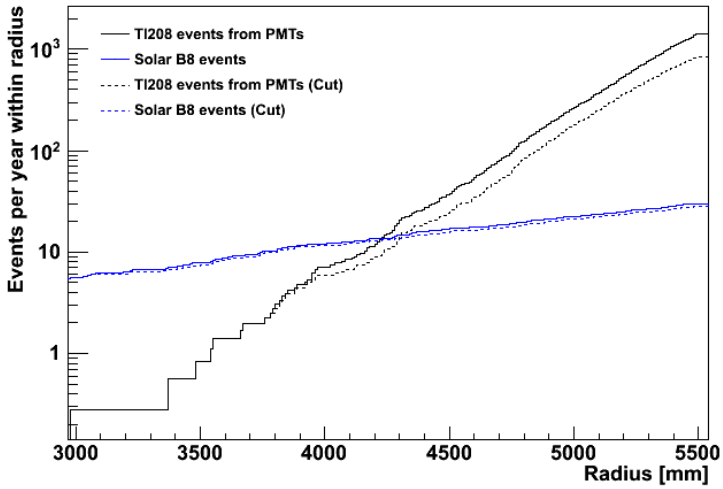

(c) Tl208 from PMTs

Figure 6.13: Events per year reconstructing within a given fiducial radius from ^{208}Tl decays in a) dust on the AV surface, b) the water shielding and c) from the PMTs within the tellurium signal window around 2.5 MeV, shown with and without the rejection cut.

6.6 Combined Tl208 backgrounds

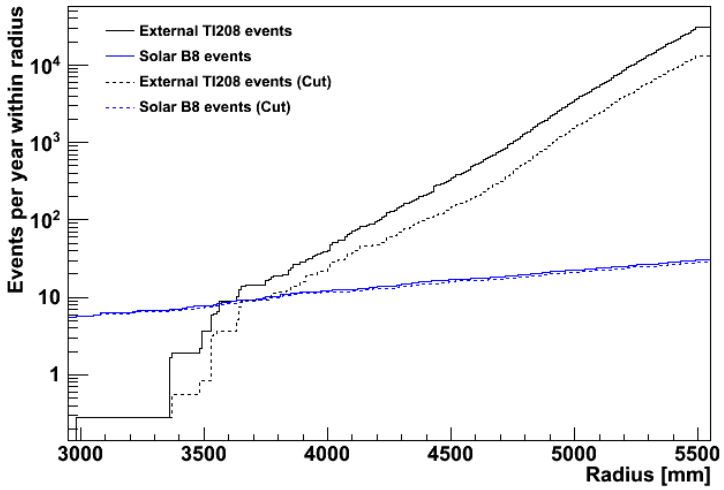

Figure 6.14: Events per year reconstructing with a fiducial radius from all ^{208}Tl external backgrounds within the tellurium signal window around 2.5 MeV, shown with and without the rejection cut.

Figure 6.14 shows a combined plot of the external ^{208}Tl backgrounds from decays in the AV, hold-down ropes, dust on the AV surface, water shielding and PMTs. Considering only the ^{208}Tl backgrounds gives a fiducial volume of 3.55 m, which can be expanded to a radius of 3.75 m using the background tagging technique. This improves the active volume of the detector from 20.7 % to 22.9 %, allowing for the 6-7 % signal sacrifice.

6.7 Conclusion

The fiducial volume of SNO+ will be limited by external backgrounds from outside the scintillator which reconstruct inside the detector. In the case of tellurium, these backgrounds will constrain the fiducial volume at 3.55 m, 20.7 % of the scintillator volume. Using the likelihood-based background identification technique described in this chapter, the external background can be tagging and the fiducial volume of the detector increased to 3.75, allowing for the 6-7 % signal sacrifice, this gives an active volume of 22.9 %.

This technique hasn't yet been fully optimised for the PDFs and position of the cut, which will require a full analysis, taking into account the final optical properties of the scintillator, fitters and all known backgounds, such as ^{214}Bi decays from the U-chain, but it has been shown to tag a significant fraction, 40-60 % depending on the source, of the external background events with a sacrifice of only 6-7 % of signal events. The technique has been shown to be robust in terms of the different loadings and optical properties of the scintillator as well as to be applicable to a variety of sources of external background.

Chapter 7

Reconstruction in the water phase

Before running with scintillator, SNO+ will run with a short 'Water Phase' in which the inner vessel will be filled with ultra pure water. This will allow determination of the level of external backgrounds as well as testing and calibration of the PMTs and electronics. There will also be the chance to do some physics in the form of a search for certain modes of nucleon decay, described in more detail in Chapter 8.

In order to do these, fitters are required for the water phase. Due to the vastly different number of hits seen in the two phases, around 10 hits per MeV for water phase but up to 500 hits per MeV in scintillator, as well as the isotropic nature of scintillation light compared to the directional Cherenkov light seen in water, the scintillator phase fitters can not be used and so new fitters were developed to determine the position, direction and energy of events. These were based on fitters used in SNO[82] and were designed to fit into the SNO+ fitter structure[76], described in Section 5.1.2.

The requirements of these fitters are those of a position resolution of around 30 cm, equivalent to that achieved during SNO[83], the tails of which are to be

understood, while the direction fit, which is required in the nucleon decay search to reject solar backgrounds, must be known such that over 90 % of the solar backgrounds can be identified with little signal loss.

7.1 Position fitter

The existing position fitter, created by P.G.Jones, consists of a likelihood method which maximises the log-likelihood when comparing the time residuals of PMT hit times to a PDF from SNO data.

$$logLike = \sum_{i}^{N} \log P_i \tag{7.1}$$

A timing cut was used such that the likelihood sum is only summed over PMTs whose hit time is within 50 ns of the median PMT hit time. This acts such as to only consider the prompt Cherenkov light and ignore later light which is more likely to have came from scattered or reflected light or detector noise.

The fitter used a Minuit optimiser to maximise the log-likelihood. In order to avoid any false maxima, the maximisation is performed for 12 different random positions around the detector and returns the vertex with the highest likelihood value. This did not use any initial seed.

This returned reasonable results for the position resolution but didn't always manage to return a successfully fit event, particularly at lower energies. Several modifications were made to this fitter to improve the resolution and number of successfully fit events, including:

A new PDF based on PMT hit times

Changing the optimiser to use the Powell method of optimisation

Using the quadFitter as a seed

The effects of these changes are discussed in the following sections.

7.1.1 New PDF

The previous fitter used a PDF generated from SNO data in D_2O. This was updated to use a PDF generated from data simulated in RAT for a detector filled with H_2O, as shown on Figure 7.1. This should allow for the differences in optical properties between the two materials as well as taking into account the changes to the PMT and concentrator properties for SNO+.

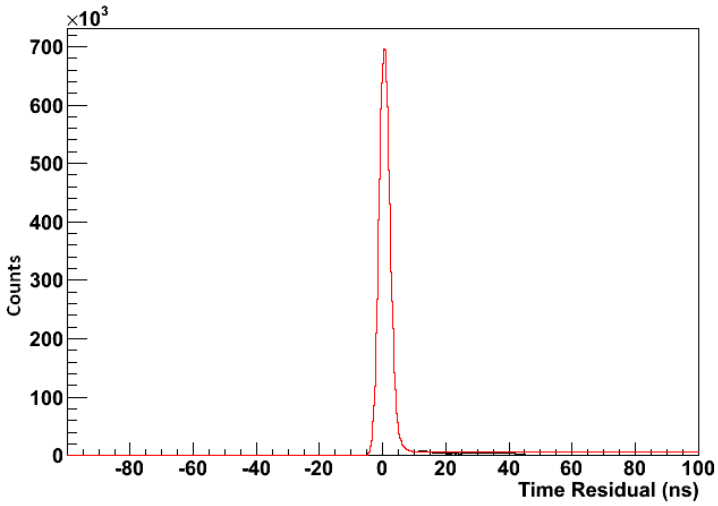

Figure 7.1: Time residual PDF for events in water.

The PDF consists of time residuals based on the PMT hit times, generated from 6 MeV electron Monte-Carlo events, filling the detector within a fiducial radius of 5.5 m. The time residuals are calculated using the same straight line path method as used for the scintillator, described in section 5.3.2, to calculate the distance travelled. Rather than use an effective speed, as is used in scintillator, it uses the group velocities of photons in the water and acrylic at 400 nm[84].

7.1.2 Change of optimiser

The waterFitter previously used a Minuit optimiser. It uses this with a 'metaOptimiser' which attempts an optimisation with the seeded position before repeating this with several more randomly-generated seed positions. It then returns the

	Fraction of events fit		Fraction of events beyond 3σ	
Energy (MeV)	Powell	Minuit	Powell	Minuit
5	0.998	0.991	0.027	0.050
6	0.996	0.988	0.020	0.022
8	0.998	0.989	0.012	0.019
10	0.995	0.984	0.015	0.019

Table 7.1: The fraction of events fit and the fraction of events which reconstruct in the tails of the distribution, more than 3σ from their true position, for events, simulated through the detector at 5, 6, 8 and 10 MeV, fit using both Powell and Minuit optimisers.

reconstructed vertex with the highest likelihood value. This was adapted for use with the Powell optimiser[80] described in chapter 5 and tested at a range of energies. The results are shown in Table 7.1 in terms of the fraction of events fit and the fraction which misfit by more than 3σ.

The Powell optimiser returns a greater fraction of fit events as well as reducing the number of events in the tails of the reconstruction, i.e. those events which have been fit more than 3σ away from their true position. The resolution of the fitter remains unchanged.

7.1.3 Using the quadFitter as a seed

	Fraction of events fit		Fraction of events beyond 3σ	
Energy (MeV)	Quad	Centroid	Quad	Centroid
5	0.997	0.999	0.026	0.054
6	0.997	0.998	0.015	0.030
8	0.997	0.999	0.014	0.011
10	0.995	0.996	0.013	0.014

Table 7.2: The fraction of events fit and the fraction of events with reconstruct in the tails of the distribution, more than 3σ from their true position, for events, simulated through the detector at 5, 6, 8 and 10 MeV, fit using seeds from the quadFitter and centroid fitter.

The waterFitter was adapted to use the quadFitter, described in Section 5.2, as a seed and was tested by fitting simulated events at a range of energies. Table 7.2 compares the fraction of events which return a fit for the cases where the

quadFitter is used as a seed and where the centroid is used. It also shows the fraction of events which reconstruct outside 3σ from their true position. Although not shown here, the resolution and execution time of the fitter remain unchanged with the two different seeds. The use of a quadFitter seed reduces the fraction of events in the tails of the position fit, as indicated by the events fitting beyond 3σ, particularly at lower energies.

7.1.4 Results

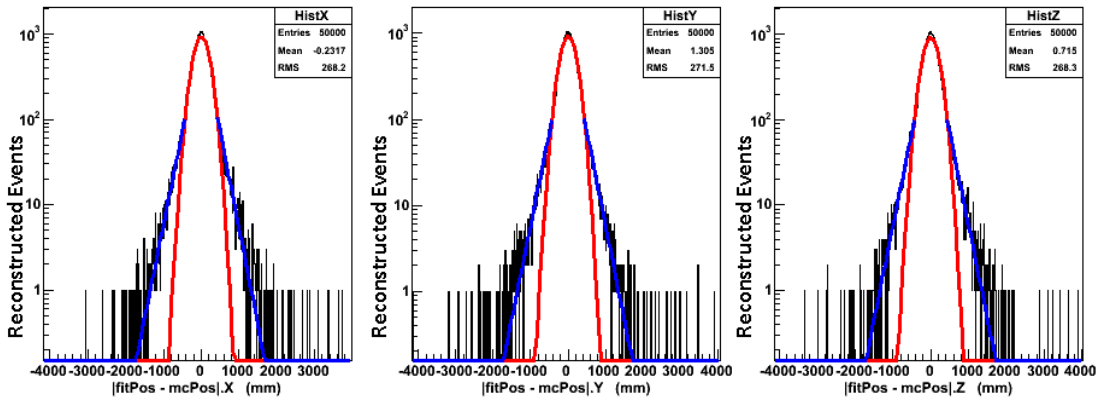

(a) 6 MeV

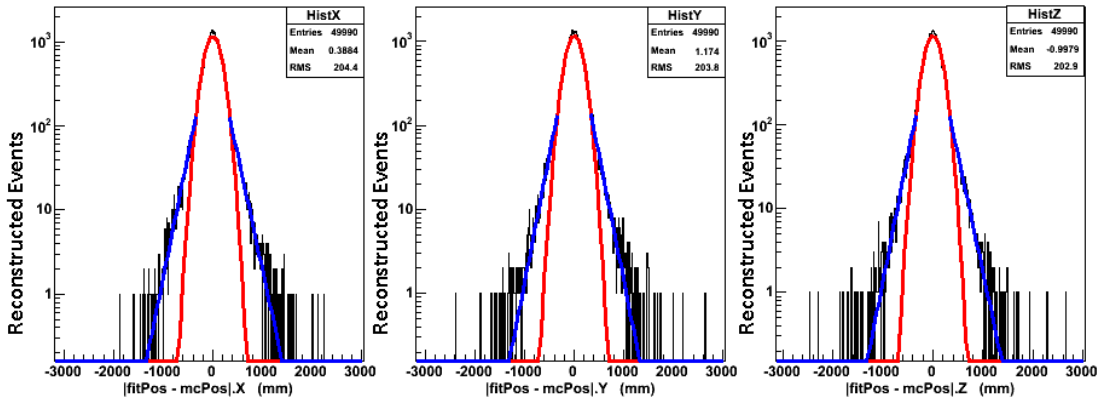

(b) 10 MeV

Figure 7.2: The difference between fitted and Monte-Carlo positions for the x, y, z components and the distance between the fitted and Monte-Carlo positions generated for 50,000 events at the centre of the detector fit using the waterFitter at a) 6 MeV and b) 10 MeV.

Figure 7.2 shows 50,000 electron events simulated at a) 6 MeV and b) 10

MeV at the centre of the detector. This is fit with a Gaussian, shown in red, with exponential tails, shown in blue. The central region is well-described by the Gaussian but, from 2σ outwards, the distribution becomes wider due to the tails of the fit and so exponentials are used. The width of the Gaussian, σ, and slope of the exponential, τ, are shown in Table 7.3. Overall, a resolution is found of 28.3 cm at 10 MeV and of 35.9 cm at 6 MeV.

	6 MeV		10 MeV	
	σ (mm)	τ (mm)	σ (mm)	τ (mm)
x	206	195	164	154
y	208	201	164	144
z	208	198	163	149

Table 7.3: The Gaussian width, σ, and exponential tail outside 2σ, τ, given in mm, which describe the reconstructed position of the waterFitter at 6 and 10 MeV, for each component x, y and z.

Energy dependence

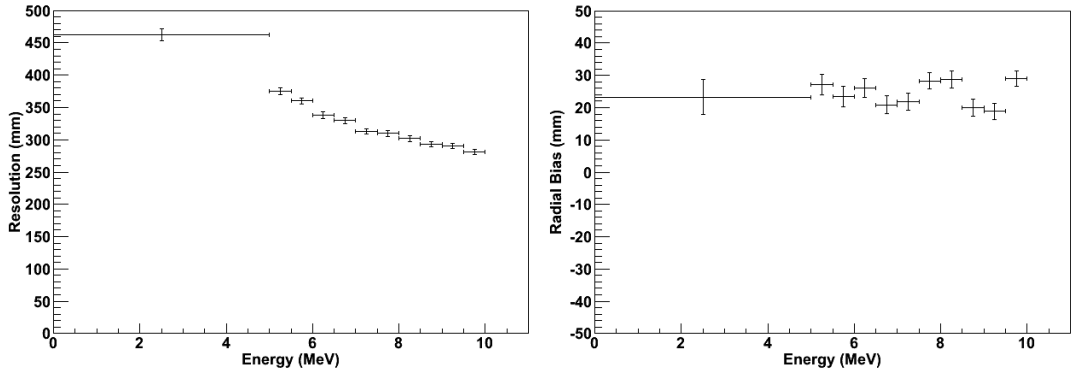

Figure 7.3: The resolution and radial bias of events reconstructed by the waterFitter at energies between 0.1 to 10 MeV, from simulations of electrons spread isotropically through the detector.

Figure 7.3 shows the energy dependence of the waterFitter's position fit. The position resolution improves with energy, as the number of hits and so the statistics available for the fitter increases, from around 35 cm at 6 MeV to 28 cm at 10 MeV. A radial bias of between 2 and 3 cm outwards, towards the edge of the detector,

is observed. This results from the use of the PMT selecter, which aims to reduce the effect of noise hits and scattering light by considering only PMT hits within 50 ns of the median hit time. Removing this PMT selector removes this bias but at the cost of larger tails in the fit.

Not yet considered is the effect of 'fitter pull'[74]. This occurs due to the directional nature of the Cerenkov light which causes the majority of early hits to be within the Cerenkov cone while the later-arriving scattered light will be distributed throughout the detector. To compensate for this, the fitted position is likely to shift towards the Cerenkov cone and so bias events in the direction of the initial particle. This will be washed out within the directionally-isotropic analysis of this thesis but is expected to show a significant effect for individual events. Future work will continue to investigate this, which will be taken into account when using real data to calibrate the fitters.

Radial dependence

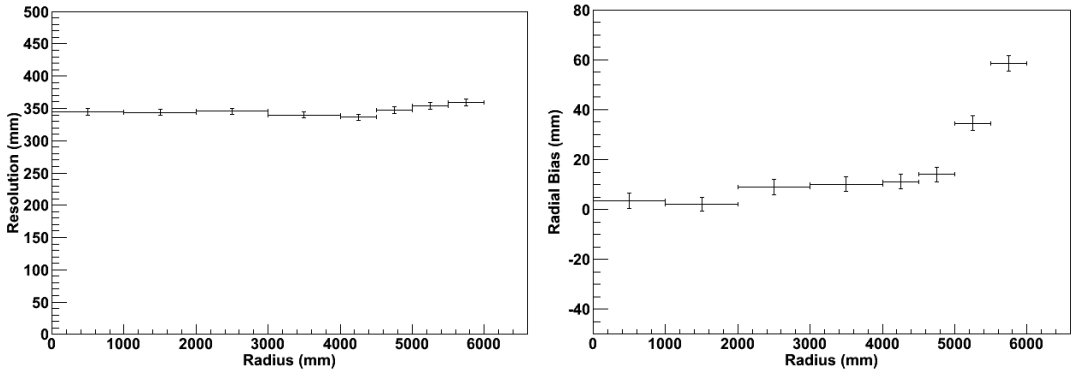

Figure 7.4: The resolution and radial bias of events reconstructed by the waterFitter at different radii for 6 MeV electrons.

Figure 7.4 shows the radial dependence of the waterFitter's position fit. The position resolution shows no strong radial dependence while the radial bias increases towards the edge of the detector.

7.2 Direction fitter

A direction fitter was created for SNO+ based on a likelihood method. An initial seed is first calculated by taking the centroid of the hits and giving the direction as the unit vector between the centroid and the fitted position:

$$\underline{fitDir} = \frac{\sum Q^2(\underline{pmtPos} - \underline{fitPos})}{\sum Q^2} \tag{7.2}$$

This gives a reasonable initial estimate for the direction. This is then used a seed for a likelihood fit for the direction. The likelihood fit compares the angle of PMT hits for the event relative to a trial direction. This is compared to a PDF, shown on Figure 7.5, consisting of the angle between the direction of the initial particle and the straight line path between a hit PMT and the event vertex and a likelihood value is calculated. A PMT selector, the same as used for the position fit, is used which only considers events within 50 ns of the median PMT hit time. This reduces the effect of noise hits and late light.

An optimiser based on the Powell method is used to maximise this likelihood value and a fitted direction is returned. A 'metaOptimiser' is used which attempts to reduce the chance of getting stuck in a false maxima by repeating this for several randomly generated seeds and returning the median direction. This helps to reduce the tails of the fit.

7.2.1 Results

The angular resolution is defined, as it was in SNO[85], as a sum of two exponentials, describing the sharp peak and the longer tail of the reconstruction:

$$R(\theta, \phi) = e^{(\alpha_1 + \beta_1 cos\theta)} + e^{(\alpha_2 + \beta_2 cos\theta)} \tag{7.3}$$

where cosθ is the angle between the initial direction of the electron and its recon-

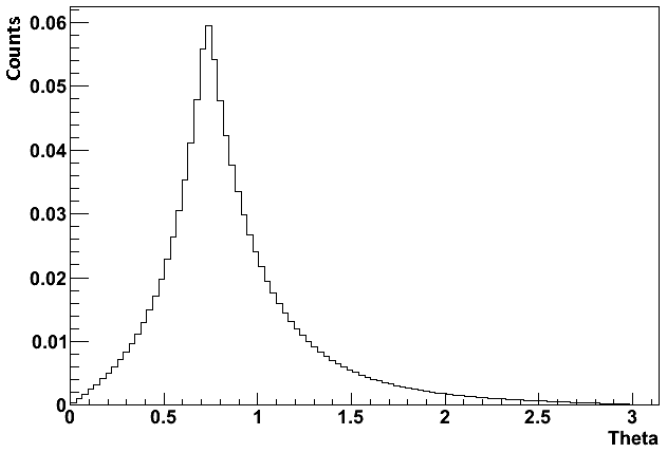

Figure 7.5: PDF showing the angle between the initial direction and the vector from the reconstructed position to the position of each PMT hit.

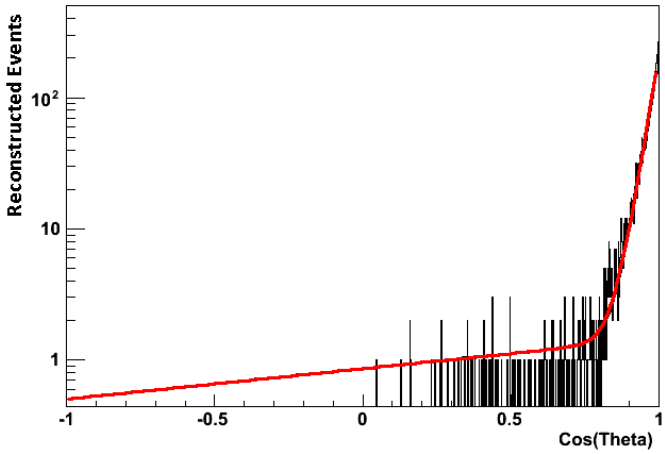

Figure 7.6: The angle between the initial Monte-Carlo direction and reconstructed direction of electrons simulated at 10 MeV is plotted in black while the angular resolution function is plotted in red.

structed direction, defined as $\widehat{\text{fitDir}}.\widehat{\text{mcDir}}$

The direction reconstruction is shown in Figure 7.6 with the angular resolution function plotted in red. The results of the angular resolution fit are given as:

α_1 = -26.432, β_1 = 31.761

α_2 = - 0.155, β_2 = 0.532

The fit can also be described by considering the angles that contain 50 %, 80% and 95% of the reconstructed events:

$\cos\theta_{50\%} = 0.976$

$\cos\theta_{80\%} = 0.936$

$\cos\theta_{95\%} = 0.832$

Energy dependence

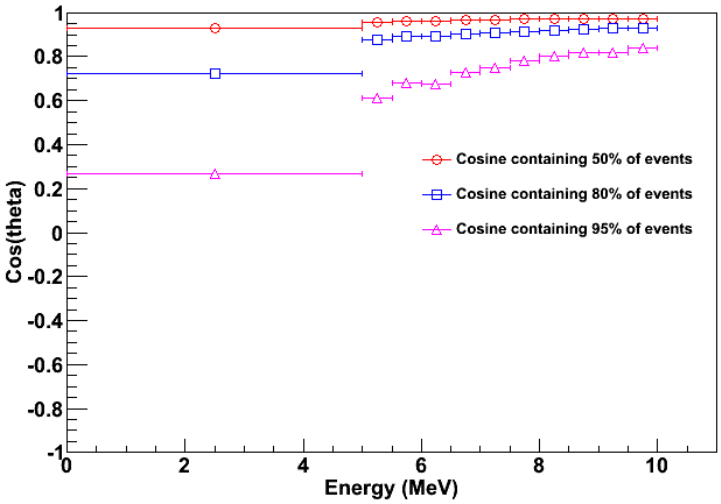

Figure 7.7: The cosine angle, relative to the initial direction of the electron, which encloses 50, 80 and 95% of reconstructed events. These are generated from electrons of energies 0.1 to 10 MeV, spread isotropically through the detector.

Figure 7.7 shows the energy dependence of $\theta_{50\%}$, $\theta_{80\%}$ and $\theta_{95\%}$. As the energy of events increases, the direction fit improves and so it takes a smaller angle to enclose a given fraction of the reconstructed signal.

Radial dependence

Figure 7.8 shows the radial dependence of $\theta_{50\%}$, $\theta_{80\%}$ and $\theta_{95\%}$. As can be seen, there is no significant radial dependence on the direction fit.

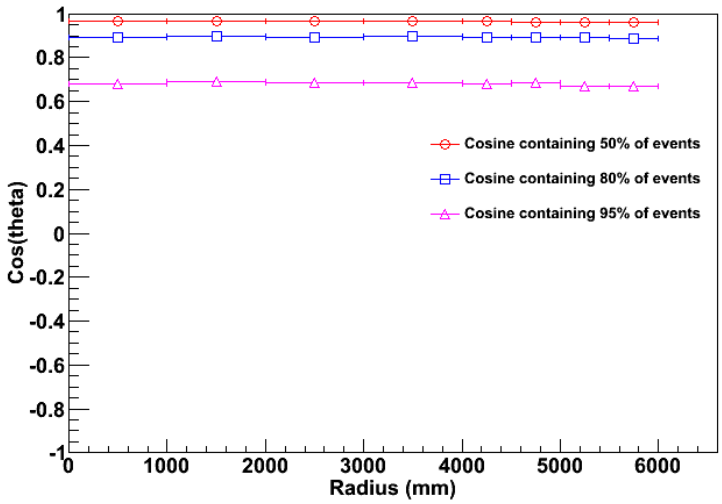

Figure 7.8: The cosine angle, relative to the initial direction of the electron, which encloses 50, 80 and 95% of reconstructed events. These are generated at different radii for 6 MeV electrons.

7.3 Conclusion

Reconstruction algorithms have been developed for the water phase of SNO+, fitting the position and direction of events. The position fitter achieves a resolution of around 30 cm, equivalent to that achieved during SNO, with the tails of the fit able to be described by an exponential. The direction fit manages to identify 95% of directional electron events at a loss of less than 10% isotropic events. It should be noted, however, that for real data, the effect of the angular distribution caused by the solar neutrinos themselves also needs to be taken into account.

Chapter 8

Nucleon Decay in the SNO+ detector

During its initial water phase, SNO+ has the ability to search for invisible nucleon decay and potentially set a new limit or even to make a significant discovery. Invisible nucleon decay occurs as a nucleon decays to a final state undetected by the experiment, e.g. $n \rightarrow 3\nu$. The decay is then detected based on the products of the remaining nucleus as it de-excites. This process has been previously investigated by some experiments such as SNO[51] and KamLAND[52] but the current limits are not as stringent as those found for the more well-known modes of kaon or pion final states.

Due to its location deep underground, SNO+ will have a low cosmogenic background. In addition, the background for this search will be lower than that of the same search in SNO as the use of H_2O rather than D_2O removes any background from neutral current events. Another advantage is that the gammas produced from ^{16}O modes have a higher branching ratio than the ^{12}C nuclei used in the search by KamLAND. Thus, it is expected that a new limit on the lifetime of invisible modes of nucleon decay can be set with only a short period of running.

8.1 Expected signal

An expected signal for invisible nucleon decay could occur as a nucleon in the ^{16}O of the water molecules decays to some undetected final state. The nucleon will leave a hole state in the nucleus. If the hole is in an inner shell, the nucleus will be in an excited state and so may emit gamma rays as it de-excites.

In the case of a decaying neutron, nucleon decay will produce $^{15}O^*$ which will then de-excite and has been predicted to, 44 % of the time, produce a 6.18 MeV gamma with 2 % of decays expected to produce a 7.03 MeV gamma. For a decaying proton, the nucleus is left as a $^{15}N^*$ state which then de-excites emitting gammas, with 41 % of decays expected to give a 6.32 MeV gamma while 4 % of decays are predicted to produce a 7.01 MeV gamma[86].

These signals will be in a region of the SNO+ energy spectrum in which few backgrounds are expected. These energies are above most natural radioactive backgrounds while backgrounds from solar neutrinos will be able to be tagged based on direction.

8.2 Backgrounds

Although low backgrounds are expected in the 5-9 MeV energy region, several forms of background do need to be considered when setting a limit:

Internal radioactive decays

External radioactive decays

Solar neutrinos

Reactor anti-neutrino

Internal backgrounds will arise from natural radioactive decays from the U and Th chains, principally through the decays of ^{208}Tl, producing a 2.6 MeV gamma alongside other lower energy gammas and betas of energies up to 1.8 MeV, and

of ^{214}Bi, decaying predominantly via beta decay with a maximum endpoint of 3.3 MeV along with some associated gammas. Assuming the water can be purified to the level of the D_2O in SNO[87], background levels are estimated at 0.88×10^{-15} g/g of H_2O for ^{232}Th and 6.63×10^{-15} g/g of H_2O for ^{238}U, producing 5.8×10^4 decays per year of ^{208}Tl and 3.7×10^6 decays per year of ^{214}Bi. The calculation of these background levels is shown in Appendix B.

External backgrounds are expected at rates of 1.29×10^7 decays of ^{214}Bi and 1.38×10^6 decays of ^{208}Tl per year from the acrylic vessel and of 4.06×10^6 decays of ^{214}Bi and 2.3×10^6 decays of ^{208}Tl per year from the hold-down ropes[81]. The majority of these can be neglected by assuming a fiducial volume of 5.5 m.

Solar neutrinos form a background to this search, however, due to the directional nature of the Cherenkov light, these should be able to suppressed using a directional cut. The level of this background is well known from measurements by SNO, expecting about 3200 interactions per year for the unoscillated flux and around 1100 when taking account of oscillations. These numbers come from background estimates described in more detail in Appendix B.

Reactor anti-neutrinos will interact via inverse beta decay, producing a positron and a neutron, $\overline{\nu}_e + p \rightarrow e^+ + n$. The positron will produce light immediately, with an energy depending on the energy of the initial incoming neutrino, while the neutron will undergo neutron capture and, after a short delay, produce a 2.2 MeV gamma. In principle, this neutron capture could be used to tag reactor neutrino events but this could be problematic due to the low numbers of PMT hits involved and the high backgrounds in the region. In this thesis, as a worst case estimate, no tagging of reactor neutrino events was applied. Background estimates of this, described in more detail in Appendix B, predict a rate of 168 interactions per year for the unoscillated flux and of around 110 interactions per year when taking the oscillations into account.

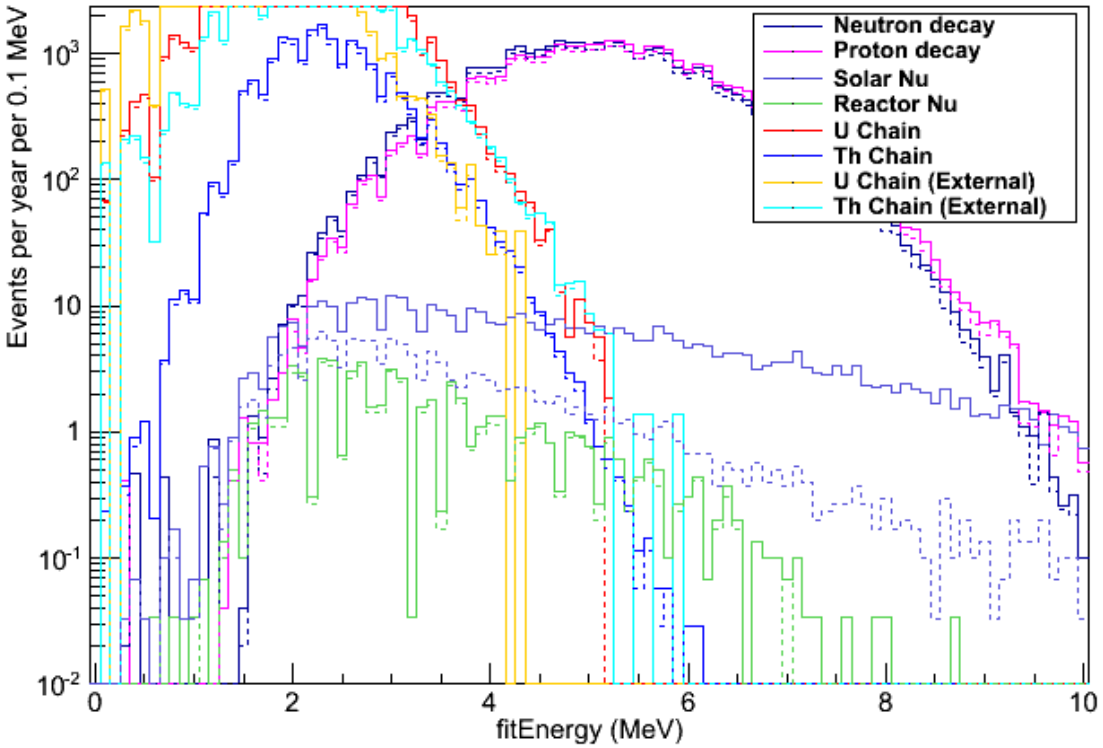

Figure 8.1: Expected energy spectrum for the water phase backgrounds of solar neutrinos, reactor anti-neutrinos and radioactive decays from the uranium and thorium chains. Also shown are the shapes of the signal gammas from nucleon decay in both the protons and neutrons of ^{16}O. The dashed lines show the spectrum with a direction cut applied to remove the solar neutrino backgrounds.

Figure 8.1 shows the energy spectrum of these water phase backgrounds alongside the potential signal gammas from the invisible decay of protons and neutrons in ^{16}O. The solid lines show this data with no direction cut applied while the dashed lines show the same spectrum using a direction cut, removing events with reconstructed directions within $\cos\theta = 0.8$ of the solar neutrino direction. This results in a sacrifice of 10% of the signal and isotropic backgrounds while removing 85-90 % of the solar backgrounds.

The expected backgrounds in various energy windows are shown in Table 8.1 with, and without, the direction cut applied. Also shown are the efficiencies of detecting the signal gammas from neutron and proton decay in each energy window.

	Energy window (MeV)					
	5 - 9		5.5 - 9		6 - 9	
	Uncut	Cut	Uncut	Cut	Uncut	Cut
U	26.0	22.3	1.0	0.0	0.0	0.0
Th	6.2	5.3	0.7	0.6	0.1	0.1
U (AV)	0.0	0.0	0.0	0.0	0.0	0.0
Th (AV)	24.8	24.8	4.1	4.1	1.4	1.4
U (Ropes)	0.0	0.0	0.0	0.0	0.0	0.0
Th (Ropes)	16.1	16.1	0.0	0.0	0.0	0.0
Solar	158.1	23.1	126.0	16.2	96.7	10.8
Reactor	7.9	7.2	4.4	4.0	2.6	2.3
Total (per year)	239.2	98.9	135.3	24.9	100.7	14.5
Total (per month)	19.9	8.2	11.3	2.1	8.4	1.2
Efficiency (n)	0.566	0.508	0.384	0.343	0.223	0.200
Efficiency (p)	0.620	0.557	0.437	0.392	0.269	0.240

Table 8.1: Table shows the expected number of background events per year reconstructing in the energy windows 5, 5.5 and 6 to 9 MeV as well as the efficiencies of detecting the gammas from both neutron and proton decay. These are presented with no direction cut applied and with a cut at $\cos\theta$=0.8, removing 85-90% of solar backgrounds.

8.3 Choice of blindness scheme

As shown in Table 8.1, above 5 MeV and with a direction cut applied, the backgrounds in an energy window above 5 MeV are expected to be low. To carry out a search for nucleon decay, this region would be blinded and, after a given run time, the observed number of events in this window would be compared to the expected rate from known backgrounds in order to set a limit, based on Poisson statistics. In choosing the nature of this blindness scheme, it is necessary to consider the requirements of calibration and of the analysis of backgrounds in the water phase.

During the water phase, calibration sources will be run to calibrate the PMTs and electronics, using the optical fibre system and the laserball, to determine the energy and position resolution, using the ^{16}N source, or to allow the source itself to be calibrated, in the case of the optical fibre system. Many of these sources will be tagged, meaning their events will be identified in the data stream and so will not interfere with the blinded analysis. More generally, for processes such as data

cleaning, which aims to identify bad events caused by detector noise and so would need access to the whole energy range, water data could be left unblinded for an initial period of time to allow analysis of the full range of data before blinding takes place.

In the water phase, background analyses of internal and external backgrounds will be carried out. In the case of the external backgrounds, this is to measure and constrain the rates of the external backgrounds from the AV, hold-down ropes and PMTs while measurements of the internal backgrounds will provide the internal U and Th content of the water as well as also giving a measurement of the rate of leaching of Pb210 decay products from the acrylic vessel into the body of the detector.

The internal background analysis will require an energy window of 4.5 to 5 MeV and so the blinded energy window considered for nucleon decay shouldn't impose on this[88]. If it appears that this region isn't sufficient to constrain these backgrounds, the nucleon decay window can be unblinded in two steps: unblinding from 5 to 5.5 MeV in order to further analyse the internal backgrounds while 5.5 MeV and above could remain blinded as data taking for the nucleon decay continues. Similarly, the measurement of external backgrounds is concerned with lower energies and so, using an expected fiducial volume cut of 5.5 m, will not affect the choice of blindness for the nucleon decay analysis[89].

The length of data taking is currently undefined as this will depend on how easily the backgrounds and electronics can be understood and on the readiness of the scintillator processing system to begin filling the detector with scintillator. Initial estimates suggest there will be somewhere between one and three months of water phase running[90]. In this thesis, a conservative estimate of a livetime of one month is assumed.

8.4 Analysis

Using a Poisson method, as described by O.Helene[91], which finds the upper limit on the number of signal events s by finding the value $S_{90\%}$ such that, given the values of b, the expected background, and n, the number of observed events, there is a 90% chance that the signal, s, is less than or equal to this value. This is found by numerically solving the integral:

$$\int_0^{S_{90\%}} A \times (s+b)^n \times e^{-(s+b)}/n! = 0.9 \tag{8.1}$$

where A is a normalisation factor such that the integral tends to 1 as $S_{90\%}$ tends to infinity. In setting the limits shown on Table 8.2, it is assumed that there are no nucleon decay events observed so n_{obs} can be set equal to nearest integer to b. A month of running is assumed at the background levels outlined in 8.1.

An upper limit of the lifetime τ can then be calculated using:

$$\tau > \frac{N_{nucleons}}{R} = \frac{N_{nucleons} \times \epsilon \times f_T}{S_{90\%}} \tag{8.2}$$

where the number of protons/neutrons $\mathrm{N}_{nucleons} = 1.85 \times 10^{32}$, assuming a fiducial volume of 5.5 m, and an upper limit on the rate can be found as $R = \frac{S_{90\%}}{\epsilon \times f_T}$ where ϵ is the efficiency of detecting the decay gamma and f_T is the livetime as a fraction of a year, in this case $\frac{1}{12}$.

The upper limits on the signal events per month and the limits that can be set on the lifetime of the decay are presented in Table 8.2. The current limit, set by KamLAND, is $\tau > 5.8 \times 10^{29}$ years. As shown on the table, with just a month's running time, SNO+ has the ability to improve upon this limit by a factor of 2, with an energy window of 5.5 to 9 MeV and a direction cut to remove the solar neutrinos producing an upper limit of 1.38×10^{30} and 1.57×10^{30} years for the decay of neutrons and protons, respectively.

	Energy window (MeV)					
	5 - 9		5.5 - 9		6 - 9	
	Uncut	Cut	Uncut	Cut	Uncut	Cut
$S_{90\%}$	8.8	6.0	6.7	3.8	5.9	3.2
τ_n (10^{29} yr)	9.9	13.1	8.8	13.8	5.8	9.7
τ_p (10^{29} yr)	10.9	14.4	10.0	15.7	7.0	11.6

Table 8.2: Table shows the upper limit, at 90% CL, on the number of signal events after a month of running and the limit that this allows us to set on the lifetime of invisible nucleon decay (given in 10^{29} years). This is shown in various energy windows, with no direction cut applied and with a cut at $\cos\theta$=0.8.

8.5 Conclusion

For a couple of months, the SNO+ will run with the detector filled with H_2O to allow calibration and commissioning of the detector. During this phase, SNO+ has a unique sensitivity to certain modes of nucleon decay due to its low backgrounds. Using the estimates of backgrounds described in this chapter and assuming just one month of data taking, SNO+ can set a limit of 1.38×10^{30} and 1.57×10^{30} years on the decay of neutrons and protons into invisible modes. This would be close to an order of magnitude higher than the limit set by SNO and a factor of two better than the current best limit as set by KamLAND.

Chapter 9

Conclusion

Among the physics goals of the SNO+ are the search for the lepton number violating process neutrinoless double beta decay and the baryon number violating process of nucleon decay. Either of these would lead to beyond Standard Model physics and so a measurement or improvement on the current limit would help to constrain the development of extensions to the Standard Model. This thesis described various techniques that have been developed to improve the sensitivity of the SNO+ experiment to these measurements: through the development of an accurate Monte-Carlo, allowing simulations of improved loading techniques, through improved reconstruction algorithms and the development of new background identification techniques. It also presents an expected limit of a search for invisible modes of nucleon decay in SNO+ after only a short period of running.

This thesis has described a scintillator Monte-Carlo model designed for use in the SNO+ experiment. While this currently provides a good model of the processes which create and act on optical photons in the detector, this will be developed further and tuned to match the outputs observed from the calibration of the detector itself when taking data begins.

This model has been used to simulate a variety of scintillator mixtures, some of which have been described in this thesis. As discussed in Chapter 4, by introducing

a secondary wavelength shifter bisMSB, SNO+ is able to achieve 0.3% loading of tellurium, which is the aim for the first stage of the experiment's double beta decay phase. This work will continue as the collaboration investigates further loading techniques and wavelength shifters still under development in an aim to improve the light yield and so push the loading levels up to percentage level.

Two position fitters for scintillator have been presented, a likelihood fitter and the quadFitter, which uses the geometric pattern of hits, which are able to achieve resolutions of around 10 and 15 cm respectively. Work will continue on improving these fitters, particularly investigating if anything can be gained using a radial or energy dependence of input parameters of the fitters. Once the detector is filled with scintillator and data taking begins, these fitters will be calibrated and their performances evaluated using calibration sources.

A background tagging technique was discussed, which uses a likelihood method and the difference in the shape of the time residual distribution of external backgrounds and signal electrons to distinguish between events originating inside the scintillator and those originating from decays of ^{208}Tl from sources outside the detector. This was shown to apply to events from within the acrylic vessel, the hold-down ropes, the PMTs and the water shielding. Identifying these events reduces the number of external backgrounds reconstructing within the signal window for a search for the $0\nu\beta\beta$ of ^{130}Te and so allows a larger fiducial volume to be applied, increasing the sensitivity for such a search. This technique will refined further, with investigations proceeding into the possibility of combining the timing with the angular distribution of such events to increase the ability to tag and reject them.

The thesis presents, as its final chapter, an expected limit that can achieved by a search for invisible modes of nucleon decay in SNO+. By assuming the detector can meet similar levels of cleanliness as those achieved in SNO and using the known background levels of solar and reactor neutrinos, a limit of 1.38×10^{30} and

1.57×10^{30} years could be set on the decay of neutrons and protons into invisible modes. During its initial water phase, expected to take place in late 2013/early 2014, SNO+ will begin taking data to search for nucleon decay. Over the coming months, the background estimates and blindness scheme will be refined further and a full analysis plan developed. The water phase will allow measurements of both the internal and external backgrounds, providing real data rather than the estimates used in this thesis. Using these improved measurements of the background and using blinded data above 5 MeV, it should be possible, after only a short run time, for the SNO+ experiment to set a leading limit on invisible modes of nucleon decay, improving on the current best limit set by KamLAND by over a factor of two.

Appendix A

Effect of light yield upon energy resolution in a $0\nu\beta\beta$ search

In this calculation for the optimal light yield of a given loading of tellurium, the only backgrounds considered are the $2\nu\beta\beta$ background of ^{130}Te and the solar background of ^{8}B. As a flat background, the solar background reconstructing within the signal window will scale proportionally to the energy resolution ΔE while the 2ν background, which rises steeply away from double beta decay end point, is assumed to scale as ΔE^6.

If it assumed that the reconstructed energy is proportional to the number of PMT hits, nhits, the energy resolution can be defined as $\Delta E = \frac{1}{\sqrt{\text{nhits}}}$ so the rates of the two backgrounds become $a_{B8} \times (\text{nhits})^{-0.5}$ and $a_{2\nu} \times (\text{nhits})^{-3}$, where a_{B8} and $a_{2\nu}$ are two constants depending on the relative levels of the two backgrounds at a given loading.

Calculations by A.Mastbaum find, assuming 0.3% loading at 193 hits per MeV, 5.34 ^{8}B[92] and 2.58 2ν[93] events per year in the region of interest. The relative levels of the two backgrounds can then plotted for different assumed values of nhits per Mev, as shown on Figure A.1. If the minimum required nhits is defined to be that at which the 2ν background no longer dominates, it can seen that a

nhits per MeV of at least 150 hits is required.

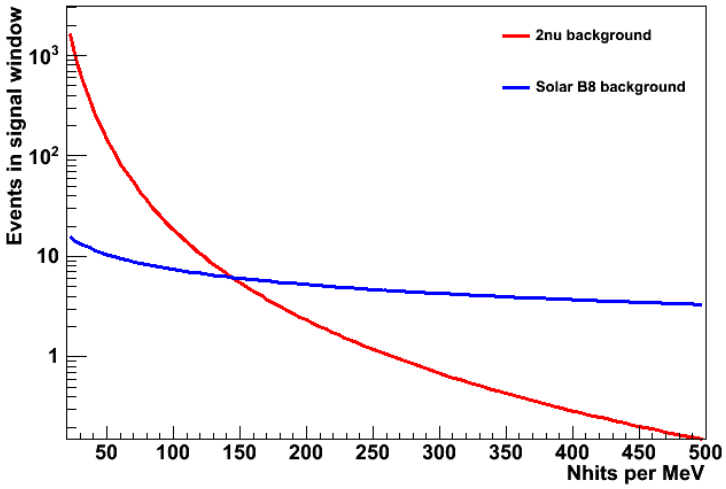

Figure A.1: Relative rate of events from the ^{130}Te 2ν background and solar ^{8}B backgrounds reconstructing in the energy window at different assumed light levels, given in nhits per MeV.

Appendix B

Water phase background rates

This appendix contains the calculations used to make estimates of the background rates in the water phase, from internal radioactive decays of U and Th in the water, from solar ^{8}B neutrinos and from reactor anti-neutrinos, used in the nucleon decay analysis of Chapter 8.

B.1 Internal backgrounds

The internal backgrounds that need to be considered for nucleon decay are from natural radioactive decays in the U and Th chains. These will lead to the decays of ^{208}Tl and ^{214}Bi, whose high energy tails may produce events above 5 MeV. Until the experiment switches on, these will not be measured but currently two possible cases are assumed, those of background levels equivalent to the D_20 in SNO and of levels equivalent to the water shielding, although it is probable that the actual background level will fall somewhere between the two. The numbers used are taken from the SNO background levels at the end of the NCD phase[87].

B.1.1 Equivalent to the D_20 in SNO

Assuming that SNO+ can achieve background levels for the H_2O equivalent to those achieved for the D_20 in SNO at the end of the NCD phase, backgrounds are expected of:

0.88×10^{-15} g/g of H_2O for ^{232}Th
6.63×10^{-15} g/g of H_2O for ^{238}U

1000 t of H_2O within the detector gives background levels of:

8.8×10^{-10} kg of ^{232}Th or 2.27×10^{15} atoms
6.63×10^{-9} kg of ^{238}U or 1.66×10^{16} atoms.

^{232}Th has a lifetime of 1.4×10^{10} yrs, with 36 % of decays branching to ^{208}Tl. This gives an expected rate of 5.8×10^4 decays per year of ^{208}Tl within the H_2O.

^{238}U has a lifetime of 4.5×10^9 yrs, all of which decay through ^{214}Bi, giving 3.71×10^6 decays per year of ^{214}Bi within the H_2O.

B.1.2 Equivalent to the water shielding in SNO

Assuming that SNO+ can achieve background levels for the H_2O equivalent to those achieved for the water shielding in SNO at the end of the NCD phase, backgrounds are expected of:

3.0×10^{-14} g/g of H_2O for ^{232}Th
3.5×10^{-13} g/g of H_2O for ^{238}U

1000 t of H_2O within the detector gives background levels of:

3×10^{-8} kg of ^{232}Th or 7.74×10^{16} atoms
3.5×10^{-7} kg of ^{238}U or 8.81×10^{17} atoms.

^{232}Th has a lifetime of 1.4×10^{10} yrs, with 36 % of decays branching to ^{208}Tl. This gives an expected rate of 2×10^{6} decays per year of ^{208}Tl within the H_2O.

^{238}U has a lifetime of 4.5×10^{9} yrs, all of which decay through ^{214}Bi, giving 1.96×10^{8} decays per year of ^{214}Bi within the H_2O.

B.2 Solar neutrinos

The total ^{8}B solar neutrino flux has been predicted at 5.69×10^{6} per cm^2 per second, from the BS05(OP) solar model described in[94]. The Solar Standard Model flux spectrum for ^{8}B neutrinos[95] was scaled to this level and convoluted with the elastic scattering cross-section, taken from the SNO code and based on a paper by J.N.Bahcall[96]. This gives the rate of 3.36×10^{-37} interactions per second per target electron.

This was then multiplied by the number of electrons in the detector, 3×10^{32}, to get a total number of 3175 interactions expected per year, ignoring neutrino oscillations. Neutrino oscillations were then applied, scaling this by around a factor of three, to give around 1060 interactions per year from electron neutrinos.

B.3 Reactor anti-neutrinos

Reactor anti-neutrino backgrounds were estimated with a flux of 2.88×10^{5} per cm^2 per second above threshold[97]. The energy spectrum of the neutrino flux was normalised to this and convoluted with the inverse beta-decay cross-section[98]:

$$\sigma = 0.0952 \times (\frac{E_e \times p_e}{1MeV}) \times 10^{-42} cm^2 \tag{B.1}$$

where $E_e = E_\nu - (M_n - M_p)$, $p_e = \sqrt{E_e^2 - m_e^2}$, E_ν is the energy of the initial neutrino and M_n, M_p and m_e are the neutron, proton and electron masses.

This was then multiplied by the number of free protons in the detector, 6×10^{31},

considering two protons per water molecule. This neglects those protons bound in the oxygen atom as these are too tightly bound in the nucleus to interact at these energies.

$$Rate = N_{protons} \times \int Flux.\sigma \tag{B.2}$$

This predicts a rate of 168 events reactor anti-neutrinos interactions per year, ignoring neutrino oscillations. Neutrino oscillations were applied to simulations of reactor events, using a Monte-Carlo processor, dropping the event rate to around 110 events per year, which produces around 180 events per proton $\times 10^{32}$ per year, the rate expected from independent calculations of this for SNO+[99].

Bibliography

[1] A.Sakharov *Pisma Zh. Eksp. Teor. Fiz. 5* (1967) .

[2] P. D. Bari, "An introduction to leptogenesis and neutrino properties," *Contemporary Physics* **53** no. 4, (2012) .

[3] E. Fermi *Z. Phys.* **88** (1934) 161–177.

[4] C.L.Cowan, F.Reines, F.B.Harrison, H.W.Kruse, and A.D.McGuire, "Detection of the Free Neutrino: A Confirmation," *Science* **124** (1956) .

[5] G.Danby, J. Gaillard, K.Goulianos, L.M.Lederman, N.Mistry, and M.Schwartz, "Observation of High-Energy Neutrino Reactions and the Existence of Two Kinds of Neutrinos," *Phys. Rev. Lett.* **9** no. 1, (1962) .

[6] **DONuT** Collaboration, "Observation of Tau Neutrino Interactions," *Phys. Lett.* **B504** no. 3, (2001) 218–224.

[7] "Precision electroweak measurements on the Z resonance," *Phys. Rept.* **427** (2006) 257–454.

[8] M.Goldhaber, L.Grodzins, and A.W.Sunyar, "Helicity of Neutrinos," *Phys. Rev.* **109** no. 3, (1958) 1015–1017.

[9] K. Zuber, *Neutrino Physics*. CRC Press, 2012.

[10] **Super-Kamiokande** Collaboration, "Evidence for an oscillatory signature in atmospheric neutrino oscillation," *Phys. Rev. Lett.* **93** (2004) .

[11] **K2K** Collaboration, "Evidence for muon neutrino oscillation in an accelerator-based experiment," *Phy. Rev. Lett.* **94** (2005) .

[12] **MINOS** Collaboration, "Measurement of Neutrino Oscillations with the MINOS Detector in the NuMi Beam," *Phy. Rev. Lett.* **101** (2008) .

[13] R. Davis, D. S. Harmer, and K. C. Hoffman, "Search for Neutrinos from the Sun," *Phys. Rev. Lett.* **20** (1968) 1205–1209.

[14] **Kamiokande** Collaboration, "Observation of ^{8}B Solar Neutrinos in the Kamiokande-II Detector," *Phys. Rev. Lett.* **81** (1998) .

[15] **SAGE** Collaboration, "Results from SAGE," *Phys. Lett. B* **328** no. 1-2, (1994) 234–248.

[16] **SNO** Collaboration, "Measurement of Charged Current Interactions Produced by ^{8}B Solar Neutrinos at the Sudbury Neutrino Observatory," *Phys. Rev. Lett.* **87** (2001) .

[17] **SNO** Collaboration, "Direct Evidence for Neutrino Flavor Transformation from Neutral-Current Interactions in the Sudbury Neutrino Observatory," *Phys. Rev. Lett.* **89** (2002) .

[18] **KamLAND** Collaboration, "Measurement of Neutrino Oscillation with KamLAND: Evidence of Spectral Distortion," *Phys. Rev. Lett.* **94** (2005) .

[19] **Daya Bay** Collaboration, "Observation of electron-antineutrino disappearance at Daya Bay," *Phys. Rev. Lett.* **108** (2012) .

[20] **RENO** Collaboration, "Observation of Reactor Electron Anti-neutrinos Disappearance in the RENO Experiment," *Phys. Rev. Lett.* **108** (2012) .

[21] **T2K** Collaboration, "Indication of Electron Neutrino Appearance from an Accelerator-produced Off-axis Muon Neutrino Beam," *Phys. Rev. Lett.* **107** (2011) .

[22] **Double-Chooz** Collaboration, "Indication for the disappearance of reactor electron antineutrinos in the Double Chooz experiment," *Phys. Rev. Lett.* **108** (2012) .

[23] **Particle Data Group** Collaboration, J. et al., *Neutrino Mass, Mixing and Oscillations*, vol. 86. 2012.

[24] J.J.Gomez-Cadenas, J.Martin-Albo, M.Mezzetto, F.Monrabal, and M.Sorel, "The search for neutrinoless double beta decay," *Riv. Nuovo Cim.* **35** (2011) .

[25] S.M.Bilenky and C.Giunti, "Neutrinoless double-beta decay. A brief review," *Mod. Phys. Lett.* **A27** (2012) .

[26] **Mainz** Collaboration, "Final Results from phase II of the Mainz Neutrino Mass Search in Tritium Beta Decay," *Eur. Phys. C* **40** no. 4, (2004) .

[27] **Troitsk** Collaboration, "An upper limit on electron antineutrino mass from Troitsk experiment," *Phys. Rev. D* **84** (2011) .

[28] **KATRIN** Collaboration, "The KATRIN Neutrino Mass Experiment," *Nucl. Instrum. Meth.* **A623** (2010) .

[29] K.Assamagan, Ch.Bronnimann, M.Daum, H.Forrer, R.Frosch, P.Gheno, R.Horisberger, M.Janousch, P.R.Kettle, Th.Spirig, and C.Wigger, "Upper limit of the muon-neutrino mass and charged-pion mass from momentum analysis of a surface muon beam," *Phys. Rev. D* **53** (1996) .

[30] **ALEPH** Collaboration, "An upper limit on the tau neutrino mass from three and five prong tau decays," *Eur. Phys. J. C* **2** (1998) .

[31] **Planck** Collaboration, "Planck 2013 results. XVI. Cosmological parameters," *Astronomy & Astrophysics* (2013) .

[32] E. Majorana, "Theory of the Symmetry of Electrons and Positrons," *Nuovo Cim.* **14** (1937) .

[33] M.Goeppert-Mayer, "Double beta-disintegration," *Phys. Rev.* **48** (1935) .

[34] W.H.Furry, "On transition probabilities in double beta-disintegration," *Phys. Rev.* **56** (1939) .

[35] C.Vilela, "Development of the tracking detector for SuperNEMO and analysis of double-beta decay in 48Ca using NEMO3 data," *IOP Talk* (2013) .

[36] H.V.Klapdor-Kleingrothaus and I.V.Krivosheina, "The evidence for the observation of 0ν beta beta decay: The identification of 0ν beta beta events from the full spectra," *Mod. Phys. Lett.* **A21** (2006) .

[37] **GERDA** Collaboration, "Status of the GERDA experiment," *J. Conf. Series* **120** (2008) .

[38] **NEMO** Collaboration, "Limits of different Majoran decay modes of ^{100}Mo and ^{82}Se for neutrinoless double beta decays in the NEMO-3 experiment," *Nucl. Phys.* **A765** (2006) .

[39] **SuperNEMO** Collaboration, "SuperNEMO project," *J. Phys. Conf. Ser.* **120** (2008) .

[40] **CUORICINO** Collaboration, "^{130}Te Neutrinoless Double-Beta Decay with CUORICINO," *Astropart. Phys* **34** (2011) .

[41] **CUORE** Collaboration, "Sensitivity and Discovery Potential of CUORE to Neutrinoless Double-Beta Decay," *arXiv:1109.0494* (2911) .

[42] **KamLAND-Zen** Collaboration, "Limit on neutrinoless double beta decay of ^{136}Xe from the First Phase of KamLAND-Zen and comparison with the positive claim in ^{76}Ge," *Phys. Rev. Lett.* **110** no. 6, (2013) .

[43] **EXO** Collaboration, "Search for Neutrinoless Double-Beta Decay in ^{136}Xe with EXO-200," *Phys. Rev. Lett.* **109** no. 3, (2012) .

[44] A. Mastbaum, "130Te $0\nu\beta\beta$ Energy Spectrum Plot." SNO+-doc-1975-v1, July, 2013.

[45] A. Mastbaum. Private communication, 2013.

[46] **IMB** Collaboration, "Search for proton decay into e^+ and π^0 in the IMB-3 detector," *Phys. Rev. D* **42** (1990) .

[47] **Super-Kamiokande** Collaboration, "Search for Nucleon Decay into Charged Anti-lepton plus Meson in Super-Kamiokande I and II," *Phys. Rev. D* **85** (2012) .

[48] **Super-Kamiokande** Collaboration, "Search for Proton Decay through $p \to \overline{\nu} k^+$ in a large water Cherenkov detector," *Phys. Rev. Lett.* **83** (1999) .

[49] **Super-Kamiokande** Collaboration, "Search for Proton Decay into Muon plus Neutral Kaon in Super-Kamiokande I, II, and III," *Phys. Rev. D* **86** (2012) .

[50] R.N.Mohapatra and A.Perez-Lorenzana, "Neutrino mass, proton decay and dark matter in TeV scale universal extra dimension models," *Phys. Rev. D* **67** (2003) .

[51] **SNO** Collaboration, "Constraints on Nucleon Decay via Invisible Modes from the Sudbury Neutrino Observatory," *Phys. Rev. Lett.* **92** (2004) .

[52] **KamLAND** Collaboration, "Search for the Invisible Decay of Neutrons with KamLAND," *Phys. Rev. Lett* **96** (2006) .

[53] **SNO** Collaboration, "The Sudbury Neutrino Observatory," *Nucl. Instrum. Meth.* **A449** (2000) 172–207.

[54] K. Singh, M. Hedayatipoor, and A. Hallin, "The Expected Performance and Motion of the Upward and Downward Ropes in the SNO+ Rope Net." SNO+-doc-1872-v1, April, 2013.

[55] N.Fatemi-Ghomi, "LAB covergas system." SNO+-doc-1803-v2, March, 2013.

[56] A. Mastbaum and R. Bonventre, "Electronics Overview." SNO+-doc-1316-v1, February, 2012.

[57] S. Peeters, "Calibration Overview." SNO+-doc-1614-v1, August, 2012.

[58] K. Singh, P. Gorel, C. Krauss, and Z. Petriw, "Camera System for SNO+." SNO+-doc-1680-v3, March, 2013.

[59] J. Maneira, "ELLIE: Details." SNO+-doc-514-v2, June, 2010.

[60] A. Reichold, K. Clark, I. Coulter, and K. Majumdar, "SMELLIE Status." SNO+-doc-1623-v1, August, 2012.

[61] J. Maneira, "New model for light production and propagation in RAT." SNO+-doc-583-v2, July, 2010.

[62] J.B.Birks, *The theory and practice of scintillation counting.* Pergamon Press, 1967.

[63] D. H. Perkins, *Introduction to High Energy Physics (2nd Edition).* Addison-Wesley Publishing, 1982.

[64] S. Asahi, "Scattering measurement at Queen's." SNO+-doc-802-v1, February, 2011.

[65] S. Grullon, "Liquid scintillator light yield measurements." SNO+-doc-1488-v4, August, 2012.

[66] H. C. Tseung and N. Tolich, "Ellipsometric measurements of the refractive indices of linear alkylbenzene and EJ-301 scintillators from 210 to 1000 nm." SNO+-doc-963-v1, May, 2011.

[67] H. C. Tseung, "Birks' constant and alpha quenching factors from bucket." SNO+-doc-905-v1, March, 2011.

[68] H. M. O'Keeffe, E. O'Sullivan, and M. C. Chen, "Scintillation decay time and pulse shape discrimination in oxygenated and deoxygenated solutions of linear alkylbenzene for the SNO+ experiment," *Nucl. Instrum. Meth.* **A640** (2011) 119–122.

[69] A. Wright, "LAB Optics Report." SNO-doc-219-v1, October, 2008.

[70] **Borexino** Collaboration, "Ultra-low background measurements in a large volume underground detector," *Astropart. Phys.* **8** (1998) 141–157.

[71] **Geant4** Collaboration, *Geant4 User's Guide for Application Developers.* 2012.

[72] M. Chen. Private communication, 2013.

[73] A. Wright, "Scintillator Development for SNO+." SNO-doc-319-v1, July, 2009.

[74] S. Brice, *Monte Carlo and Analysis Techniques for the Sudbury Neutrino Observatory.* PhD thesis, University of Oxford, 1996.

[75] P. G. Jones, *Background Rejection for the Neutrinoless Double Beta Decay Experiment SNO+.* PhD thesis, University of Oxford, 2012.

[76] P. G. Jones, "Fitter Structure." SNO-doc-911-v4, March, 2012.

[77] K. Clark. Private communication, 2011.

[78] S. Morgan, "Characterisation and analysis of total internal reflection and refraction effects at sno+," Master's thesis, University of Oxford, 2010.

[79] K. Majumdar, "A Geometry-base NearAV Method." SNO+-doc-1710-v2, March, 2013.

[80] W. H. Press, *Numerical Recipes in C++: the art of scientific computing.* Cambridge University Press, 2002.

[81] S. Grullon, S. Asahi, and J. Maneira, "External Background Simulation Studies for Te." SNO+-doc-1720-v6, April, 2013.

[82] M. Boulay, *Direct Evidence for Weak Flavour Mixing with the Sudbury Neutrino Observatory.* PhD thesis, Queen's University, 2001.

[83] G. D. Orebi Gann, *An Improved Measurement of the ^8B Solar Neutrino Spectrum at the Sudbury Neutrino Observatory.* PhD thesis, University of Oxford, 2008.

[84] P. G. Jones, "Short Note on the ET1D and GV1D PDFs." SNO+-doc-1507-v1, July, 2012.

[85] P. Wittich, *First Measurement Of The Flux Of Solar Neutrinos From The Sun At The Sudbury Neutrino Observatory.* PhD thesis, University of Pennsylvania, 2000.

[86] H.Ejiri, "Nuclear deexcitations of nucleon holes associated with nucleon decays in nuclei," *Phys. Rev. C* **48** no. 3, (1993) .

[87] H. M. O'Keefe, *Low energy background in the NCD Phase of the Sudbury Neutrino Observatory.* PhD thesis, University of Oxford, 2008.

[88] E. O'Sullivan. Private communication, 2013.

[89] S. Grullon. Private communication, 2013.

[90] G. D. Orebi Gann. Private communication, 2013.

[91] O.Helene *Nucl. Inst. and Meth.* **212** (1983) .

[92] A. Mastbaum, "130Te 2vbb Spectrum." SNO+-doc-1934-v1, June, 2013.

[93] A. Mastbaum, "130Te 0vbb Energy Spectrum Plot," June, 2013.

[94] J.N.Bahcall, A.M.Serenelli, and S.Basu, "New Solar Opacities, Abundances, Helioseismology, and Neutrino Fluxes," *ApJ* **621** (2005) .

[95] W.T.Winter and S.J.Freedman, "The ^{8}B neutrino spectrum," *Phys. Rev. C* **73** (2006) .

[96] J.N.Bahcall, M.Kamionkowski, and A.Sirlin, "Solar neutrinos: Radiative corrections in neutrino-electron scattering experiments," *Phys. Rev. D* **51** (1995) .

[97] S. Andringa, "Anti-neutrino analysis." SNO+-doc-1377-v1, March, 2012.

[98] P.Vogel and J.F.Beacom, "The angular distribution of the reaction $\overline{\nu}_e + p \to e^+ + n$," *Phys. Rev. D* **60** (1999) .

[99] S. Andringa, "Study of Reactor Anti-Neutrino Oscillations in SNO+." SNO+-doc-397-v1, December, 2009.